



THE HONG KONG  
POLYTECHNIC UNIVERSITY

香港理工大學

Pao Yue-kong Library

包玉剛圖書館

---

## Copyright Undertaking

This thesis is protected by copyright, with all rights reserved.

**By reading and using the thesis, the reader understands and agrees to the following terms:**

1. The reader will abide by the rules and legal ordinances governing copyright regarding the use of the thesis.
2. The reader will use the thesis for the purpose of research or private study only and not for distribution or further reproduction or any other purpose.
3. The reader agrees to indemnify and hold the University harmless from and against any loss, damage, cost, liability or expenses arising from copyright infringement or unauthorized usage.

If you have reasons to believe that any materials in this thesis are deemed not suitable to be distributed in this form, or a copyright owner having difficulty with the material being included in our database, please contact [lbsys@polyu.edu.hk](mailto:lbsys@polyu.edu.hk) providing details. The Library will look into your claim and consider taking remedial action upon receipt of the written requests.

The Hong Kong Polytechnic University

Department of Electronic and Information  
Engineering

Development of Gallium Nitride-Based  
Ultraviolet Detectors

Lui Hsian Fei Hardy

A thesis submitted in partial fulfillment of the requirements  
for the degree of Doctor of Philosophy

September 2007

## CERTIFICATE OF ORIGINALITY

I hereby declare that this thesis is my own work and that, to the best of my knowledge and belief, it reproduces no material previously published or written, nor material that has been accepted for the award of any other degree or diploma, except where due acknowledgement has been made in the text.

---

Lui Hsian Fei Hardy

## **Abstract**

Visible-blind ultraviolet (UV) photodetectors have found many important applications nowadays, such as the ultra-high density storage optical reading head and the measurement of UV radiation (UV index) from the solar UV spectrum on the earth's surface. Gallium Nitride (GaN), having band-gap energy of 3.4 eV which corresponds to a band-edge wavelength of 364 nm, is a material of choice for the development of short wavelength optoelectronic devices. Strong atomic bonding, high chemical stability and high saturation velocity as well as a strong breakdown field are important properties that make it a superior candidate over silicon for optoelectronic applications.

The role of the double buffer layer in a GaN film and its effects on the device's radiation hardness has been being addressed in the first part of this study. Two types of GaN Schottky barrier photodetectors were fabricated for the radiation hardness studies. Type I devices were fabricated on MBE-grown GaN films using a double-buffer-layer structure, whereas the type II control devices were fabricated on conventional buffer-layer structures only. The radiation hardness of the devices was studied by the accelerated optical stressing experiment. The results show that the two types of devices

exhibited high-quality and comparable Schottky characteristics prior to the application of stress, in terms of their current-voltage ( $I$ - $V$ ) characteristics, capacitance-voltage ( $C$ - $V$ ) properties, low-frequency noise and responsivities. However, the device properties were found to behave quite differently upon the application of high-power UV radiation stress. All type II devices under stress exhibited catastrophic breakdown at some point during the optical-stress process and none of type I devices under test demonstrated any substantial breakdown for the entire stressing period of up to 90 hours. The increase of reverse current, decrease of capacitance and reduced UV-to-visible response ratios suggest that either significant generation of traps or the activation of metastable states within the bandgap occur, enable electrons occupying these states to be excited by sub-bandgap photons. The results from low-frequency noise measurement provided further evidence of the trap origin of the degradation phenomena. The experimental results clearly indicate that the use of the double buffer layer results in improved crystallinity and is responsible for the substantial improvements in the radiation hardness of the type I devices.

The second part of this study was the fabrication and characterization of indium-tin-oxide (ITO)/GaN Schottky photodetectors. The optimal growth conditions for the ITO was systematically studied. The  $I$ - $V$  characteristics show that the reverse leakage currents of the devices are strongly dependent on the deposition conditions of the ITO. The experimental results also indicate that interfacial traps play an important role on the optoelectronic properties of the device. Due to the fact that the ITO is deposited in an oxidizing ambient, high surface states density would exist at the ITO/GaN interface

leading to a degradation in the device performance. A unique device structure was investigated in which a thin Ni layer was deposited between the ITO and GaN film for the passivation of the GaN surface. The optoelectronic properties of this novel device are found to be substantially improved.

## **Acknowledgements**

I am grateful to the Department of Electronic and Information Engineering of The Hong Kong Polytechnic University for inviting me into their Ph.D. program and provide the studentship for the study.

I would like to thank my adviser Professor Charles Surya for accepting me into his research group. Thank you for your stimulating discussions and general guidance in achieving this work. It has been an invaluable experience for me to work in the Thin Film Optoelectronics Research Group.

I would also like to thank the members of the Thin Film Optoelectronics Research Group Dr. W. K. Fong, Mr. B. H. Leung, Mr. P. K. Lai, Mr. K. H. Leung, Mr. M. Y. Tung, Mr. C. W. Lip and Miss S. W. Ng for their helpful discussions, encouragement and friendship. My special thanks go to Professor C. F. Zhu from the China University of Science and Technology for sharing his insights and expertise in device characterization. Additionally, I wish to thank Dr. W. K. Fong for his guidance in MBE operation and the supply of GaN epiwafers for this study. I am also very grateful to Mr. B. H. Leung for sharing his knowledge and assistance in the field of fabrication.

I wish to acknowledge Dr. A. B. Djurišić and the members of the Optoelectronics and Nanomaterials Group of The University of Hong Kong, for their help and contributions to the preparation of ITO films used in this study. Thanks also to Mr. C. H. Cheung for his assistance in the operation of the deposition equipment.

Finally, I wish to thank my parents for their patience and endless support throughout my life. Although they may not even understand what I did in graduate school, their love was always a source of motivation for me.

# Table of Contents

Abstract .....	i
Acknowledgements .....	iv
Table of Contents .....	vi
List of Figures .....	x
List of Tables .....	xvi
List of Symbols and Constants.....	xvii
<b>1 Introduction .....</b>	<b>1</b>
1.1 GaN Semiconductors .....	1
1.2 Visible-blind GaN-based UV Detector.....	2
1.3 Organization of the Thesis .....	6
<b>2 Reviews of GaN Materials .....</b>	<b>7</b>
2.1 Introduction to III-nitride Materials.....	7
2.1.1 Properties of III-nitrides .....	7
2.1.2 Crystal Structure of III-nitrides .....	9
2.1.3 Polarization Effects .....	12
2.1.4 Substrates of III-nitride Growth .....	12
2.2 Epitaxial Growth of GaN .....	15
2.2.1 MOCVD Growth of III-nitrides .....	15
2.2.2 MBE Growth of III-nitrides .....	18
2.3 Application of Buffer Layers for Improved GaN Film Quality.....	21

<b>3</b>	<b>Schottky Contact UV Photodiodes: Operation Principles and Fabrication Processes.....</b>	<b>26</b>
3.1	Introduction.....	26
3.2	Theory of Rectifying Metal Semiconductor Contacts .....	27
3.2.1	Current Transport Mechanisms in the Schottky Diode .....	32
	<i>Thermionic Emission</i> .....	32
	<i>Quantum Mechanical Tunneling</i> .....	33
	<i>Leakage Current</i> .....	34
3.3	Principles of Optical Detection.....	35
3.4	Advantages of Wide Bandgap Schottky UV Photodiodes.....	37
3.5	Fabrication and Processes of Ni/n-GaN UV Photodiodes .....	42
3.5.1	GaN Film Epitaxy .....	44
	<i>Molecular Beam Epitaxy Growth of GaN films for Schottky Contact Photodiodes</i> .....	44
	<i>Growth of High Quality GaN Films Utilizing a Double Buffer Layer Structure</i> .....	46
3.5.2	Electron-Beam Deposition .....	51
	<i>Electron-Beam Evaporation</i> .....	51
	<i>Sample Preparation Prior to Deposition</i> .....	54
3.5.3	Patterning - Photolithography .....	54
3.5.4	The Device Fabrication Processing Steps .....	55
<b>4</b>	<b>Measurement and Analysis Techniques .....</b>	<b>60</b>
4.1	Current-Voltage Measurements .....	60
4.1.1	Experimental Setup .....	61
4.1.2	Barrier Height.....	64
4.1.3	Ideality Factor.....	65
4.1.4	Series Resistance .....	66
4.2	Capacitance-Voltage Measurements.....	66
4.2.1	Experimental Setup .....	69

4.2.2	Free Electron Concentration.....	72
4.2.3	Barrier Height .....	73
4.3	Low-frequency Noise Measurements .....	74
4.3.1	Noise Theory .....	74
	<i>G-R Noise Trapping Kinetics</i> .....	75
	<i>1/f Noise Theories</i> .....	78
	<i>Hooge's Model</i> .....	79
	<i>Quantum 1/f Noise Model</i> .....	80
	<i>1/f Noise Arising from the Superposition of Lorentzians</i> .....	81
	<i>The McWhorter Model</i> .....	82
	<i>Thermal Activation Model</i> .....	83
4.3.2	Experimental Setup .....	85
4.4	Spectral Response Measurement .....	87
4.4.1	Responsivity .....	87
4.4.2	Experimental Setup .....	89
<b>5</b>	<b>Experimental Results and Discussion.....</b>	<b>92</b>
5.1	Experiment I: Optical Stressing of Ni/n-GaN UV Photodiodes.....	92
5.1.1	Accelerated Optical Stressing .....	93
5.1.2	Experimental Results on <i>I-V</i> Measurements .....	96
5.1.3	Experimental Results on <i>C-V</i> Measurements.....	105
5.1.4	Experimental Results on Spectral Response Measurements.....	108
5.1.5	Experimental Results on Low-frequency Noise Measurements .....	114
5.1.6	Discussion .....	118
5.2	Experiment II: Development of ITO/n-GaN UV Photodiodes.....	124
5.2.1	Indium Tin Oxide (ITO).....	124
	<i>Properties of ITO</i> .....	126
	<i>ITO Deposition Techniques</i> .....	127
	<i>Transmittance Measurement</i> .....	129
5.2.2	ITO Deposition and Fabrication of the ITO/n-GaN UV Photodiodes .	131

5.2.3 Experimental Results and Discussion .....	137
<b>6 Conclusions and Suggestions for Future Work .....</b>	<b>152</b>
<b>Appendix: Ni/GaN UV Detector Fabrication Processes .....</b>	<b>157</b>
Simplified Block Diagram of the Process Flow .....	157
Schematic of the Fabrication at Select Points in the Process Flow.....	158
<b>References .....</b>	<b>162</b>

## List of Figures

2.1	Schematic diagram of wurzite crystal structure. The unit cell is shaded.....	11
2.2	Schematic diagram of zincblende crystal structure .....	11
2.3	Atomic arrangement and stacking order of the c-plane sapphire .....	14
2.4	Schematic diagram of an MOCVD system .....	16
2.5	Schematic diagram of an MBE system.....	19
2.6	Evolution of GaN film growth.....	23
2.7	Microstructure of GaN grown on sapphire. (a) side view showing tilt for individual grains in the [0001] direction; (b) Plan view showing twist in the $[11\bar{2}0]$ direction. ....	24
3.1	Schematic energy band structure of an unbiased metal/n-type semiconductor Schottky contact .....	28
3.2	The energy band diagram and photocurrent generation mechanisms of a Schottky junction under zero bias .....	36

3.3	Dispersion curve diagrams ( $E$ versus $k$ ) for both direct bandgap (left) and indirect bandgap (right) materials. Visualizations of the generation and recombination of electron and hole in both type of semiconductors are shown with the photon and phonon transitions processes .....	39
3.4	Device cross sectional view of the Ni/n-GaN Schottky photodiode .....	43
3.5	Ga beam equivalent pressure measured at different cell temperatures.....	45
3.6	The room temperature PL spectra of samples grown with various ITBL thicknesses .....	49
3.7	(a) The FWHM and the relative intensity of the bandedge emission of GaN films plotted against the thickness of ITBL; (b) Hall mobility and PL peak position at different ITBL thicknesses.....	50
3.8	Schematic diagram of an e-beam deposition system.....	51
3.9	The structure of two types of GaN epitaxial layers used for Ni/GaN UV photodiodes fabrication: (a) n-GaN epi-layer with ITBL for the fabrication of type I devices; and (b) n-GaN epi-layer without ITBL for the fabrication of type II devices.....	56
3.10	AFM results showing the thickness of the deposited Ni layer .....	58
4.1	Schematic of the $I$ - $V$ measurement setup .....	62
4.2	Experimental $I$ - $V$ result of a typical Ni/n-GaN Schottky photodiode.....	63

4.3	Typical $I$ - $V$ characteristic of a GaN Schottky photodiode plotted in a semi-logarithm of $I / (1 - e^{-qV/k_B T})$ against the applied voltage $V$ . Dashed lines shows the linear fitted result for parameter extraction .....	63
4.4	Schematic of a reverse biased Schottky barrier superimposed with an ac voltage and the associated charge distribution in energy band diagram .....	67
4.5	Schematic of the $C$ - $V$ measurement setup .....	69
4.6	Typical $C$ - $V$ data measured from Ni/n-GaN Schottky photodiode.....	71
4.7	Experimental result of $C^{-2}$ plotted against applied voltage $V$ .....	72
4.8	Schematic of a Lorentzian form power spectrum with a corner frequency $f_c$ ..	78
4.9	Superposition of five Lorentzian form power spectra (a), (b), (c), (d) and (e), with distributed corner frequency. The corresponding summation spectrum is shown as dash line .....	81
4.10	Schematic of the low-frequency noise measurement setup.....	86
4.11	Schematic of the spectral response measurement setup.....	91
5.1	Schematic of the accelerated optical stressing experiment.....	95
5.2	Typical $I$ - $V$ characteristic measured from type I and type II.....	97
5.3	Typical semi-logarithmic plot of $I / (1 - e^{-qV/k_B T})$ against $V$ measured from (a) type I and (b) type II devices .....	98

5.4	Experimental semi-logarithmic $I$ - $V$ characteristics measured at different $t_S$ for (a) type I and (b) type II devices.....	103
5.5	Reverse leakage current at -0.2 V as a function of $t_S$ for type I (solid symbols) and type II (open symbols) devices. (a) Linear plot; (b) Semi-logarithmic plot. ....	104
5.6	$C^{-2}$ versus $V$ characteristics for a typical (a) type I and (b) type II devices before optical stress .....	106
5.7	Experimental $C$ - $V$ characteristics measured at different $t_S$ for (a) type I and (b) type II devices.....	107
5.8	Typical spectrally resolved current responsivities for type I (solid line) and type II (dashed line) devices before optical stress. Dashed line shows the theoretical calculated responsivity of 30% quantum efficiency for eye guidance.....	109
5.9	Experimental spectral responsivities for (a) type I and (b) type II device both before optical stress, after 90 hours and 27 hours of optical stress respectively.....	110
5.10	Responsivity at 350 nm as a function of stress time for both type I and type II photodiodes.....	112
5.11	Responsivity at 400nm as a function of stress time for both type I and type II photodiodes.....	112
5.12	Rejection ratio of stressed devices as a function of stress time.....	113

5.13	Experimental $S_V(f)$ for typical type I and type II devices before optical stress .	116
5.14	Experimental values of $F_n$ plotted as a function of $t_S$ for type I and type II devices .....	116
5.15	Schematic diagram of the carrier tunneling process through localized states in a Schottky barrier contact .....	119
5.16	Schematic diagram of photo-electrons excitation process by defect state within the bandgap.....	120
5.17	The FWHM and the relative intensity of the bandedge emission of GaN films plotted against the thickness of ITBL.....	123
5.18	Hall mobility and PL peak position at different ITBL thicknesses .....	123
5.19	Schematic of the transmittance measurement setup .....	130
5.20	Device cross sectional view of the ITO/n-GaN Schottky photodiode.....	132
5.21	Oxygen partial pressure against flow rate of the e-beam system .....	134
5.22	Measured ITO etching depth as a function of the etching time.....	136
5.23	Typical transmittance spectrum of 80 nm ITO and 15 nm Ni e-beam evaporated on quartz substrates .....	140
5.24	Spectral current responsivity curves for devices fabricated at different ITO deposition conditions. Dashed line shows the theoretical calculated responsivity of 30% quantum efficiency for eye guidance .....	141
5.25	Typical $I$ - $V$ characteristic of the ITO/n-GaN Schottky photodiode device .....	143

5.26	Typical $C^{-2}$ - $V$ characteristic of the ITO/n-GaN Schottky photodiode device...	143
5.27	ITO/n-GaN Schottky photodiode reverse bias current at -1 V as a function of the substrate temperature .....	144
5.28	ITO/n-GaN Schottky photodiode reverse bias current at -1 V as a function of the oxygen flow .....	144
5.29	Transmission spectrum of 3 nm Ni on quartz substrate .....	145
5.30	Device cross sectional view of the ITO/Ni/n-GaN Schottky photodiode .....	146
5.31	Measured $I$ - $V$ characteristic for ITO/n-GaN, ITO/Ni/n-GaN and Ni/n-GaN Schottky photodiodes .....	148
5.32	Rejection ratio of fabricated ITO/n-GaN, ITO/Ni/n-GaN and Ni/n-GaN Schottky photodiodes .....	148
5.33	Normalized current noise spectrum $S_I(f)/I^2$ for ITO/n-GaN, Ni/n-GaN and ITO/Ni/n-GaN Schottky photodiodes.....	151

## List of Tables

2.1	General properties of AlN, GaN and InN.....	8
3.1	List of materials used in the fabrication of UV detectors and their corresponding deposition parameters .....	53
5.1	Time to failure for the optically stressed devices .....	101
5.2	Summary of the ITO layer growth conditions, ITO/n-GaN photodiodes responsivities and rejection ratios.....	138

## List of Symbols and Constants

Symbol	Name	Unit/Value
$A$	Area	$\text{m}^2$
$A^{**}$	Modified Richardson constant	$\text{A cm}^{-2} \text{K}^{-2}$
$a_{\text{sapphire}}$	Lattice constant $a$ of Sapphire	$\text{\AA}$
$a_{\text{wGaN}}$	Lattice constant $a$ of wurzitic GaN	$\text{\AA}$
$C$	Capacitance	farad
$C_t$	Proportionality constant	
$c$	Speed of light	$2.997925 \times 10^8 \text{ m/s}$
$c_n$	Electron capture coefficient	$\text{cm}^3 \text{s}^{-1}$
$c_{\text{sapphire}}$	Lattice constant $c$ of Sapphire	$\text{\AA}$
$c_{\text{wGaN}}$	Lattice constant $c$ of wurzitic GaN	$\text{\AA}$
$D_s$	Density of surface states	$\text{eV}^{-1} \text{m}^{-3}$
$E$	Energy	J
$E_o$	Tunneling constant	eV
$E_{oo}$	Tunneling parameter	eV
$E_c$	Conduction band energy	J
$E_f$	Fermi level energy	J
$E_g$	Band gap energy	J
$E_p$	Lorentzian peak energy	J
$E_v$	Valence band energy	J
$E_\tau$	Thermal activation energy of carriers	J
eV	Electron volt	$1.602177 \times 10^{-19} \text{ J}$
$f$	Frequency	Hz
$f_T$	Trap filling probability	

$f_c$	Lorentzian form corner frequency	Hz
$g$	Trap degeneracy factor	
$h$	Planck constant	$6.626076 \times 10^{-34}$ J-s
$h\nu$	Photon energy	J
$I$	DC current	A
$I_{photo}$	Photocurrent	A
$I_r$	Reverse current	A
$I_s$	Reverse saturation current	A
$I_m$	Tunneling current	A
$\Delta I_o$	Fluctuation current	A
$k_B$	Boltzmann constant	$8.617385 \times 10^{-5}$ eV/ K $1.380658 \times 10^{-23}$ J / K
$L_o$	Lorentzian prefactor	
$m_o$	Electron rest mass	$9.11 \times 10^{-31}$ kg
$m_e^*$	Effective mass of electron	kg
$N_C$	Effective density of states	$\text{cm}^{-3}$
$N$	Carrier concentration	$\text{cm}^{-3}$
$N_A$	Ionised acceptor concentration	$\text{cm}^{-3}$
$N_D$	Ionised donor concentration	$\text{cm}^{-3}$
$N_T$	Trap density	$\text{cm}^{-3}$
$N_{TR}$	Normalized trap density	$\text{cm}^{-3}$
$N_{TT}$	Density of traps	$\text{cm}^{-3} \text{ eV}^{-1}$
$n$	Ideality factor	
$n_o$	Electron carrier concentration at equilibrium	$\text{cm}^{-3}$
$n_{T_o}$	Filled traps density at equilibrium	$\text{cm}^{-3}$
$OT$	Optical transmission power	J/s
$P_o$	Optical power	J/s
$p$	Hole carrier concentration	$\text{cm}^{-3}$
$P_\lambda$	Illumination power at specific wavelength	J
$q$	Charge of electron	$-1.602177 \times 10^{-19}$ coul
$R_{ac}$	AC resistance	$\Omega$
$\mathfrak{R}$	Responsivity	A / W, V / W
$R_{leakage}$	Leakage resistance	$\Omega$
$R_s$	Series resistance	$\Omega$

$\Delta R$	Fluctuation resistance	$\Omega$
$r_e$	Rate of electron collection	$s^{-1}$
$r_p$	Rate of photon arrival	$s^{-1}$
$S_V$	Voltage noise power spectral density	$V^2 / \text{Hz}$
$S_I$	Current noise power spectral density	$A^2 / \text{Hz}$
$T$	Temperature	K
$t_S$	Stress time	hour
$V$	Voltage	V
$V_{bi}$	Built-in potential	V
$V_{dc}$	DC voltage	V
$v_{ac}$	AC voltage	V
$x_{dep}$	Depletion width	m
$\text{\AA}$	Angstrom	$10^{-10}$ m
$\alpha_H$	Hooge parameter	
$\gamma$	Slope of linear line	
$\delta$	Oxide layer thickness	m
$\epsilon_0$	Permittivity of free space	$8.854188 \times 10^{-14}$ farad/cm
$\epsilon_i$	Permittivity	farad/cm
$\epsilon_s$	Permittivity of the semiconductor	farad/cm
$\eta$	Quantum efficiency	
$\lambda_c$	Cutoff wavelength	m
$\nu$	Electro-magnetic radiation frequency	Hz
$\rho_c$	Specific contact resistivity	$\Omega \text{ cm}^2$
$\tau_T$	Fluctuation time constant	s
$\tau_{TT}$	Tunneling time constant	s
$\tau_{Th}$	Thermal activation time constant	s
$\tau_o$	Trap time constant	s
$\phi_b$	Schottky barrier height energy	J
$\phi_m$	Work function of the metal	J
$\phi_s$	Work function of the semiconductor	J
$\phi_o$	Neutral level of localized surface states	J
$\chi_s$	Electron affinity of the semiconductor	J
$\Omega$	Active device volumn	$\text{m}^3$
$\omega$	Radian frequency	Hz

# **Chapter 1**

## **Introduction**

### **1.1 GaN Semiconductors**

Gallium Nitride (GaN) is a member of the III-nitride semiconductor group and is a promising material for the development of short wavelength optical and electronic applications. This is due to several important properties of GaN, such as its large and direct energy bandgap, good thermal and chemical stability, and physical hardness. Significant research effort has been put into the development of high quality GaN thin films as well as practical optoelectronic and electronic devices. Some successful applications worthy of note include short wavelength light emitters for full color displays, laser diodes for printing and high density information storage, high brightness light emitters operating in the blue to ultraviolet regions for solid state lighting as well as the visible-blind ultraviolet (UV) photodiodes for the measurement of the UV index from sun light [1-7]. With its high breakdown field and large electron saturation

velocity, GaN-based materials are also attractive for high power and high frequency microwave device applications [8-11]. Such high temperature and high power transistors are needed for automobile engines, future advanced power distribution systems in electric vehicles, avionics and base stations of communication systems.

With the demonstrated advantages of optical fiber telecommunication systems over conventional copper-wire based systems, converting an electrical signal to an optical signal and vice versa are now of utmost importance. GaN and the related III-nitride compound semiconductor are particularly suitable for applications in optoelectronic devices. This is because the bandgaps of III-nitride alloys vary from 0.7 eV for InN to 6.2eV for AlN. Using well established bandgap engineering techniques with the help of modern sophisticated film growth processes, such as metalorganic chemical vapor deposition (MOCVD) and molecular beam epitaxy (MBE), the bandgaps of the films can be engineered to cover continuously a spectral region from deep UV to infrared [12-14]. Hence, GaN and its alloys are uniquely suited for the development of optoelectronic devices and particularly in the UV to blue-green range.

## **1.2 Visible-blind GaN-based UV Detector**

Visible-blind UV detectors play important roles in a variety of military and civil applications including: flame/engine monitoring, chemical/biological agent sensing, and space-to-space communications [15-18]. A low-noise and high-efficiency photo-receiver would be important for use in these applications.

Several types of device structures have been proposed for the GaN-based photodetector, such as the p-n junction diode, p-i-n diode, metal-semiconductor-metal (MSM) photo diode, and semi-transparent metal-semiconductor Schottky barrier photodiode [9, 17, 19-21]. Among these structures, Schottky photodiodes are particularly attractive because of their potential for high speed operation and ease of fabrication [21-24]. The use of a Schottky barrier diode is ideal for high speed applications due to the inherent absence of slow components associated with minority carrier effects. In contrast, the p-n junction type diode, both the majority carriers and the minority carriers establish the conduction current in the forward-bias state and a reverse recovery time is required when the diode switched over due to the large amount of minority carriers stored in the opposite material, and it takes time to return to the majority-carrier state in a reverse-bias situation. An inherent disadvantage for the Schottky type photodiode, however, is the high series resistance and low optical coupling efficiencies associated with the thin semi-transparent metal layer. Also, to date, sapphire is the most commonly used substrate for the growth of GaN thin films. This is because of its relative low price and stability at high temperatures. However, due to the large differences in the lattice constants and the coefficients of thermal expansion between sapphire and GaN, it is observed that GaN films deposited directly on sapphire substrates typically exhibit a high density of crystalline defects, such as threading dislocations [12, 25]. It has been shown that such material defects lead to significant degradations in the characteristics of the resulted devices [26-29].

The study and development of GaN-based visible-blind UV Schottky photodiodes is the subject of this thesis. The development of high quality GaN films deposited on sapphire substrates is the prerequisite for the fabrication of efficient UV detectors. It has been demonstrated that the incorporation of an intermediate-temperature buffer layer (ITBL) on the MBE-grown GaN can lead to significant improvements in the optoelectronic and electronic properties of the films [30-32]. However, the effects of the ITBL in the operations of the photodiode have not yet been fully investigated. In the first part of this study, the effects of ITBL films on the performance and the reliability of the devices are systematically investigated. A comparative study between two types of GaN-based photodiodes is conducted. Type I devices are fabricated on GaN layers grown using a novel double buffer layer structure, consisting of a conventional AlN buffer layer and an ITBL. Whereas type II devices are fabricated on GaN layers grown using a single conventional AlN buffer layer only. The devices are then optically stressed by exposure to high intensity UV radiation to investigate the radiation hardness of the devices. The optical and electronic properties such as current-voltage ( $I$ - $V$ ) characteristics, capacitance-voltage ( $C$ - $V$ ) properties, low-frequency noise and the responsivities of the devices are systematically characterized to monitor the change in the devices as well as the materials properties as a function of the stress time.

Based on the results obtained in the first part of the study, the work proceeded to further improve the performance of the detector. An inherent disadvantage of the conventional semi-transparent metal-semiconductor Schottky barrier photodiode is that the thin metal layer is optically highly absorptive and reflective. The performance of the

resulting devices is therefore limited by the high series resistance and low optical coupling efficiencies. Furthermore, the high interfacial state density at the metal/GaN interface often leads to the lowering of the UV-to-visible rejection ratio. To address these problems, the use of indium tin oxide (ITO) was explored for high performance GaN based Schottky photodiodes. The unique feature of this device is that the ITO is highly transparent and conductive, which could substantially improve the properties of the devices. Detailed electrical and optical behaviors of the devices are characterized. The growth conditions of ITO are crucial to the performance of the resulting photodetectors. The deposition parameters for the ITO were optimized by systemically varying the substrate temperature and the oxygen flow. The experimental results show that the reverse leakage currents of the devices are strongly dependent on the deposition conditions of the ITO. They also indicate that, as in the case of Ni/GaN Schottky photodiodes, interfacial traps also play an important role on the optoelectronic properties of the devices. A novel process has been developed in which a thin Ni layer was deposited between the ITO and the GaN to passivate the ITO/GaN interface, with significant improvements in the reverse leakage current, low-frequency excess noise as well as the UV-to-visible rejection ratio. The low-frequency noise properties of the devices clearly indicate the reduction of the interface states with the use of the thin passivation layer.

### **1.3 Organization of the Thesis**

The thesis is organized as follows: Chapter 2 presents the fundamentals of the GaN materials. This is followed, in Chapter 3, with the operating principle of Schottky contacts and the detailed description of the processing steps involved in the fabrication of the GaN based Schottky photodiodes. Chapter 4 then gives the details of the measurements and analytical techniques used in this study, as well as the corresponding experimental setup. Chapter 5 presents two experimental results and discussion, which includes, part I the experiments on the Ni/n-GaN UV photodiodes and part II the experiments on ITO/n-GaN UV photodiodes. In the first part of Chapter 5, experiment on the fabrication of the Ni/n-GaN UV photodiodes and the optical stressing studies of these devices are described. The experimental results on the optical stressing experiments are then presented and discussed at the end of the section. This is followed by experiment II, which presents the experimental results on the study of ITO/n-GaN Schottky photodiodes. The detailed ITO deposition parameter optimization, preliminary results and discussion are also included in this section. Finally, the conclusion of the studies and suggestions for further work are presented in Chapter 6.

# Chapter 2

## Reviews of GaN Materials

### 2.1 Introduction to III-nitride Materials

#### 2.1.1 Properties of III-nitrides

Studies of the different alloys of III-nitride semiconductors show that they are the materials of choice for the development of short wavelength optoelectronic devices. The main reason is that III-nitrides have several important properties [8, 15, 33, 34]:

- i) Wide and direct bandgaps that range from infrared (0.7 eV for InN) to deep UV (6.2 eV for AlN);
- ii) Strong atomic bonds leading to high radiation and hot-electron hardness;
- iii) High chemical stability enabling the device to function in harsh environments;
- iv) High saturation velocity of current carriers;

- v) High breakdown field; and
- vi) Strong piezoelectric field at the AlGaN/GaN interface giving rise to a two-dimensional electron gas (2DEG) even without any doping in the AlGaN layer.

These important properties have led to successful commercialization of GaN-based UV detectors, fabrication of high brightness LEDs, laser diodes (LDs) operating in the range from green to UV wavelengths and high electron mobility transistors (HEMTs) [1-7, 9-11]. These devices are essential for the development of future technologies for full color displays, general lighting and next generation of high density optical storage. Table 2.1 summarized the basic properties of AlN, GaN, and InN[35, 36].

	AlN	GaN	InN
Bandgap energy (eV, @ 300K)	6.2	3.4	0.7
Lattice constant (Å, @ 300K)	a = 3.112 c = 4.982	a = 3.189 c = 5.185	a = 3.548 c = 5.760
Coefficient of thermal expansion (K <sup>-1</sup> , @ 300K)	$\Delta a/a = 4.2 \times 10^{-6}$ $\Delta c/a = 5.3 \times 10^{-6}$	$\Delta a/a = 5.6 \times 10^{-6}$ $\Delta c/a = 3.2 \times 10^{-6}$	- -
Index of refraction (@ 3.38eV)	2.15	2.67	2.85 – 3.05

Table 2.1: General properties of AlN, GaN and InN.

### 2.1.2 Crystal Structure of III-nitrides

There are three common crystal structures among the group III-nitrides – the wurzite, zincblende, and rocksalt structures. At ambient conditions, wurzite is the most stable phase. A typical hexagonal crystal structure and the wurzite crystal structure is shown in Fig. 2.1.

The chemical bonds of III-nitrides are predominantly covalent. Each atom forms 4 tetrahedral bonds with its neighboring atoms. Due to the large differences in the electronegativity of the group III atoms and nitrogen atoms, there is a significant ionic contribution to the bond which determines the stability of the respective structure. The wurzite structure has a hexagonal unit cell with two lattice constants  $a$  and  $c$ . It is shown that the ratio between  $a$  and  $c$  is  $\frac{c}{a} = \sqrt{\frac{8}{3}} = 1.633$ . Figure 2.1 shows that the crystal structure consists of two interpenetrating hexagonal close-packed (hcp) sublattices, each with one type of atom, offset along the  $c$  axis by  $5/8$  of the cell height ( $5c/8$ ). In this structure every atom of one kind is surrounded by four atoms of the other kind arranged at the edges of a tetrahedron.

The zincblende structure has a cubic unit cell, containing four group-III atoms and four nitrogen atoms. The position of the atoms within the unit cell is identical to the diamond crystal structure, which consists of two interpenetrating face-centered cubic sublattices, offset by  $1/4$  of the distance along a body diagonal. Each atom in the structure may be viewed as being positioned at the center of a tetrahedron with the four nearest

neighbours at the four corners of the tetrahedron. Figure 2.2 shows a schematic diagram of zincblende crystal structure.

The wurzite and zincblende structures are similar. In both cases, each group-III atom is bonded with four nitrogen atoms, while each nitrogen atom is bonded to 4 group-III atoms. The main difference between these two types of crystal structures lies in the stacking sequence of the diatomic planes. For wurzite crystal structures the stacking sequence of the (0001) plane is ABABAB in the  $\langle 0001 \rangle$  direction. For the zincblende crystal structure, the stacking sequence is ABCABC in the  $\langle 111 \rangle$  direction.

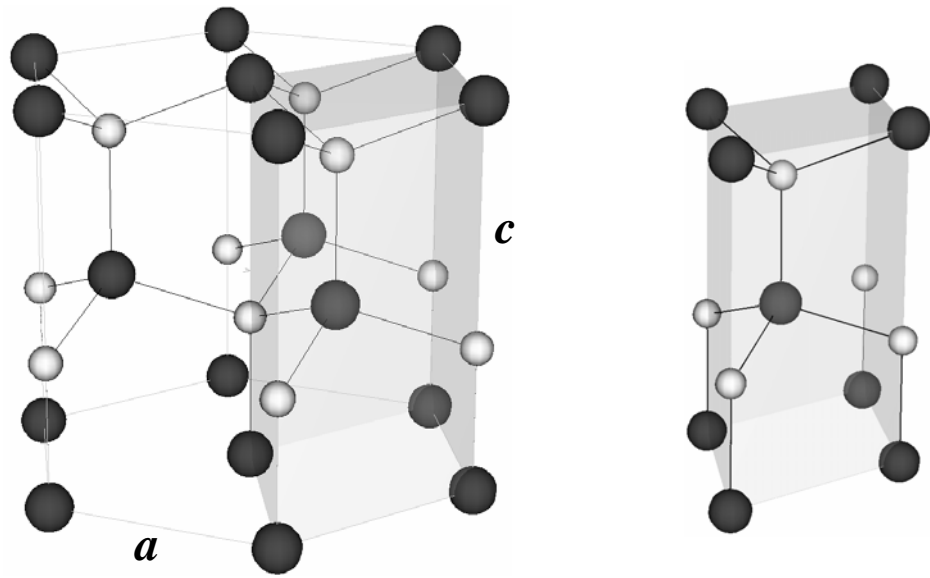


Figure 2.1: Schematic diagram of wurzite crystal structure. The unit cell is shaded.

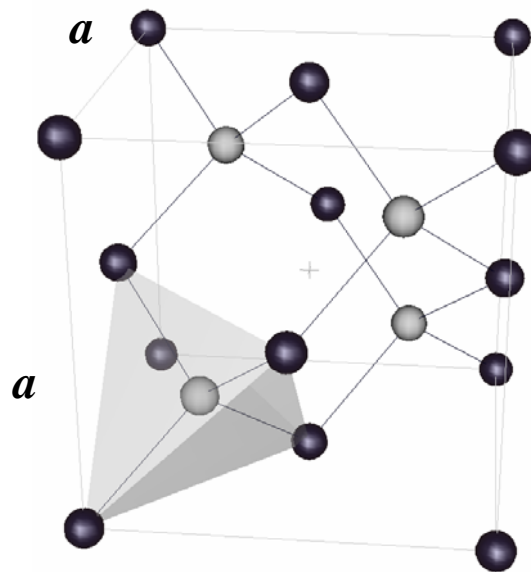


Figure 2.2: Schematic diagram of zincblende crystal structure.

### 2.1.3 Polarization Effects

The wurzitic crystal structure, shown in Fig. 2.1, indicates that there is no center of inversion. Hence, an atom position on a closed-packed plane with coordinates  $(x,y,z)$  is not invariant to the position  $(-x,-y,-z)$  since inversion results in the replacement of a group III atom by a nitrogen atom and vice versa. As a result of the lack of inversion symmetry, the crystal exhibits highly pronounced polarization effects. This gives rise to strong piezoelectric properties for the III-nitrides when strained along  $\langle 0001 \rangle$  direction. In addition, wurzite GaN has a unique axis which allows spontaneous polarization even in the absence of strain. This leads to the existence of a polarization charge at the hetero-interfaces. The piezoelectric effect has two components. One arises from lattice mismatch strain and the other from the thermal expansion coefficient difference between the substrate and the epitaxial layers. A substantial piezoelectric field is typically observed in GaN films grown on sapphire substrates due to the large lattice and thermal expansion coefficient mismatches between the two materials [37, 38].

### 2.1.4 Substrates for III-nitride Growth

Obtaining a suitable substrate for the growth of III-nitride epitaxial layers is one of the major issues encountered in the development of nitride-based devices. To date, sapphire is the most commonly used substrate for epitaxial growth of nitride materials. The quality of the GaN layers grown on sapphire are typically found to be of adequate

quality and considering sapphire is comparatively inexpensive as compared to other choices such as SiC, it is little wonder that sapphire is the substrate of choice for nitride growth. The surfaces of sapphire substrates that have been utilized for nitride growth are the c, a and r planes. The atomic arrangements for c planes are shown in Fig. 2.3.

The stacking configuration perpendicular to the c plane is also displayed in the figure. The calculated lattice mismatch between GaN and sapphire is about 30%. However due to the 30° misorientation of the Al atoms, the real mismatch is given by [39-40]

$$\frac{\sqrt{3}a_{wGaN} - a_{sapphire}}{a_{sapphire}} = 0.16 \quad (2.1)$$

where  $a_{wGaN}$  is the lattice constant  $a$  of wurzitic form GaN and  $a_{sapphire}$  is the lattice constant  $a$  of sapphire.

GaN films had also been grown on other facets, such as the r face ( $1\bar{1}02$ ), which has a much better match in the lattice constant. For instance, the lattice mismatch between the  $\langle\bar{1}101\rangle$  direction sapphire and  $\langle 0001\rangle$  direction of GaN parallel to the sapphire  $\langle\bar{1}101\rangle$  is equal to

$$\frac{3c_{wGaN} - \sqrt{3a_{sapphire}^2 + c_{sapphire}^2}}{\sqrt{3a_{sapphire}^2 + 3c_{sapphire}^2}} = 0.01 \quad (2.2)$$

where  $c_{wGaN}$  is the lattice constant  $c$  of wurzitic form GaN,  $a_{sapphire}$  and  $c_{sapphire}$  are the lattice constants  $a$  and  $c$  of sapphire.

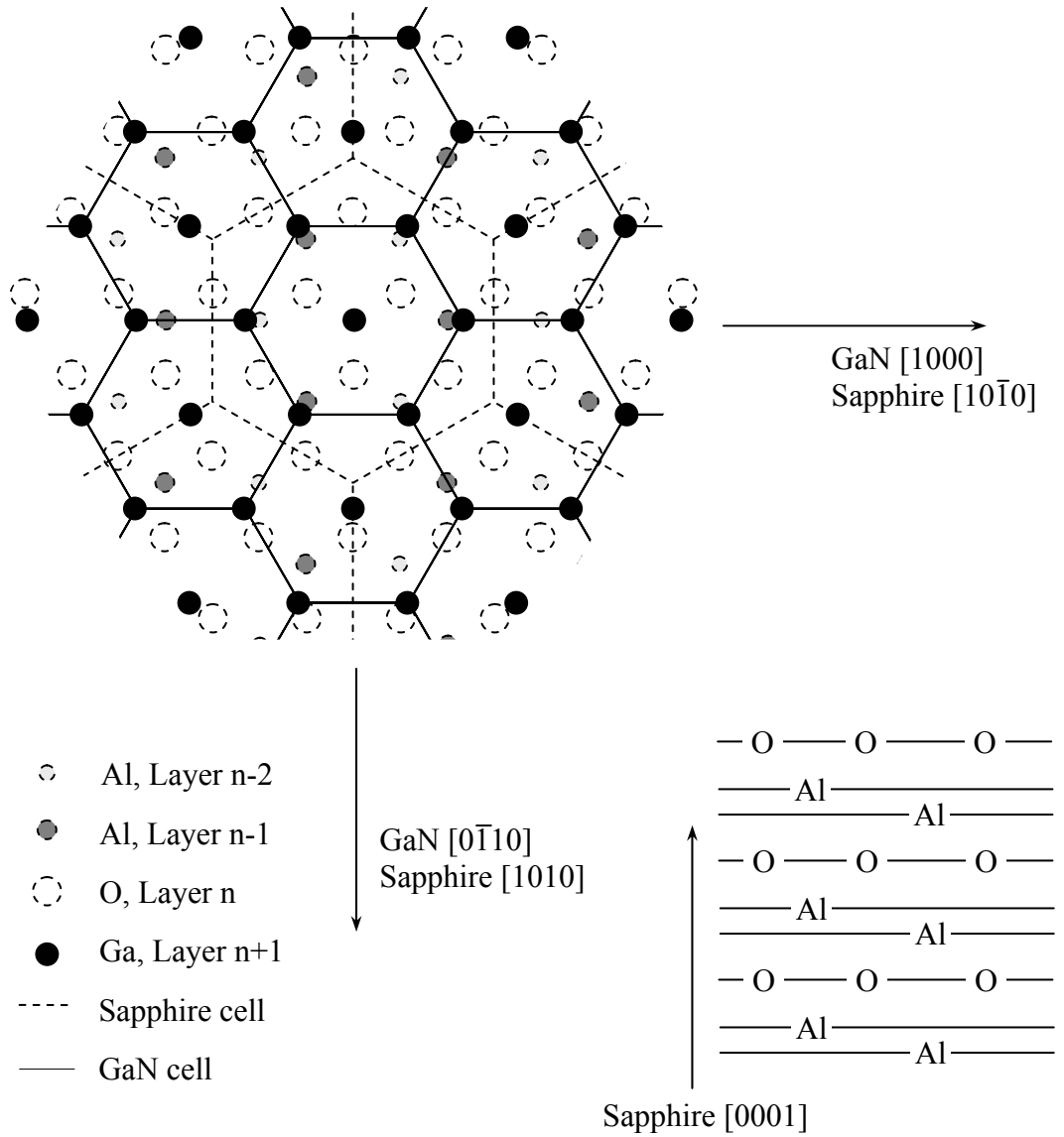


Figure 2.3: Atomic arrangement and stacking order of the c-plane sapphire.

## 2.2 Epitaxial Growth of GaN

There are three main techniques for the growth of GaN films: i) metalorganic chemical vapour deposition (MOCVD); ii) molecular beam epitaxy (MBE); and iii) hydride vapour phase epitaxy (HVPE). Process iii is typically employed for the growth of very thick GaN layers, of the order of 100  $\mu\text{m}$ , with a fast growth rate of about 50 – 60  $\mu\text{m}/\text{h}$ . For the growth of optoelectronic and electronic devices such as LEDs and high electron mobility transistors (HEMTs), accurate control of the film thickness is crucial and hence either MOCVD or MBE are typically chosen over the HVPE process.

### 2.2.1 MOCVD Growth of III-nitrides

The MOCVD technique was developed in the late sixties by Manasevit, who applied the technique to the growth of GaN on sapphire substrates. The MOCVD technique uses TriMethylGallium (TMG), TriMethylAluminum (TMA), TriMethylIndium (TMI) and  $\text{NH}_3$  as reactant sources for the growth of III-nitride films. Since the metalorganics are kept in liquid form, hydrogen carrier gas is used to transport the metalorganics to the substrate located inside the reactor which is typically kept at around 1000°C. The reactant gas, diluted with  $\text{H}_2$ , is introduced to the surface of a rotating substrate through a quartz nozzle. Separate inlets are used for different reactants to minimize the pre-deposition reaction of the gases. Rotation of the substrate is designed to improve the

uniformity of the film. A schematic diagram of an MOCVD system is shown in Fig. 2.4 below.

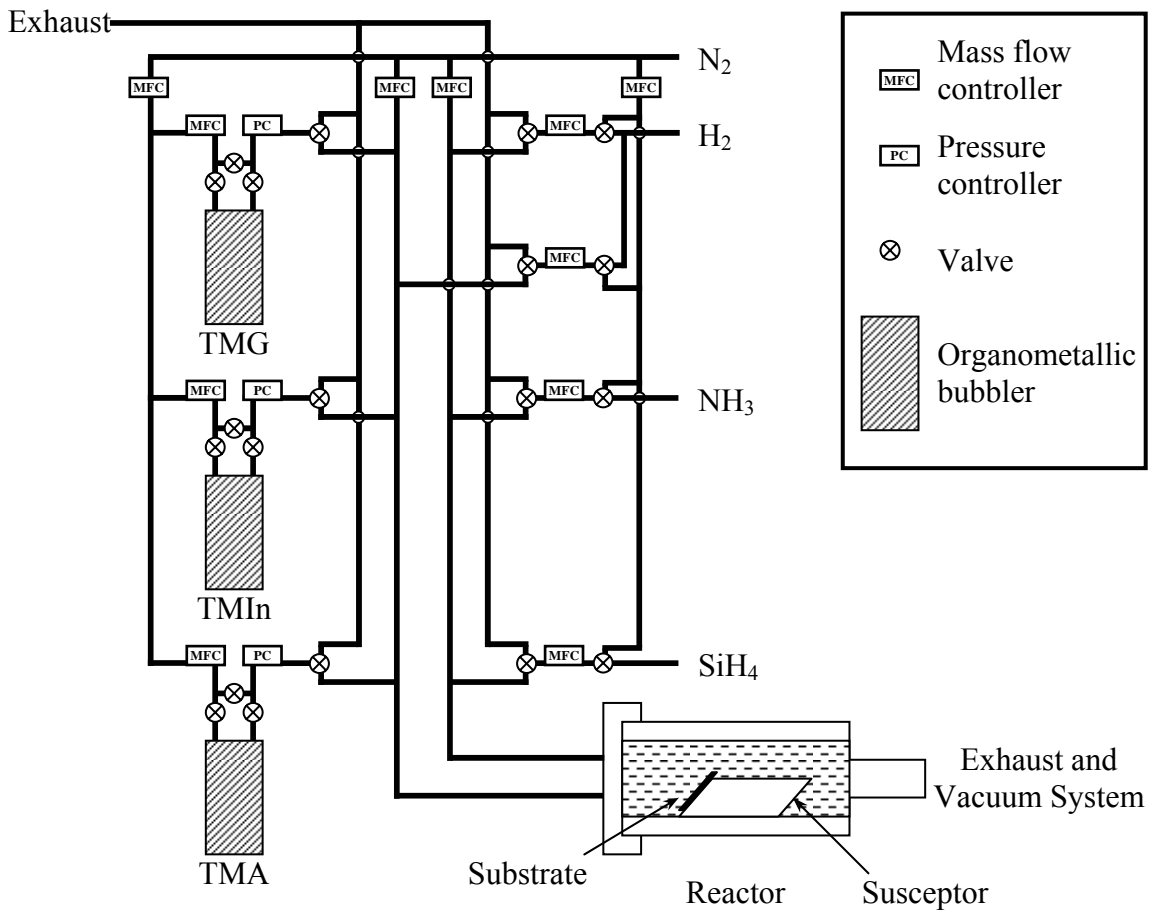


Figure 2.4: Schematic diagram of an MOCVD system.

One major problem encountered in the growth of III-nitrides is the lack of a substrate material with a lattice constant close to GaN. As mentioned in the previous section, c-plane sapphire ( $\text{Al}_2\text{O}_3$ ) is the most commonly used substrate for the growth of GaN films, which has a lattice mismatch to GaN as large as 16%. This results in three-dimensional growth of GaN material leading to high concentrations of defects and background carrier concentrations of the order of magnitude  $10^{18}$ - $10^{20}$   $\text{cm}^{-3}$ . Also, deep-level related yellow luminescence (YL) hinders the achievement of device-quality GaN films, especially in the field of optoelectronic devices. Although the physical origin of YL is still not clear, it is generally accepted that gallium vacancy is the defect responsible for YL [39-42]. In order to improve the GaN film quality, a thin buffer layer is typically grown prior to the deposition of the epitaxial layer. Typically a GaN or AlN layer grown with a thickness of around 20 nm is used as the buffer layer. The purpose of the buffer layer is to provide a surface with the nucleation sites for the reactant species to form bonds and accommodate the lattice mismatch between the GaN and the substrate. The development of such a nucleation layer marked a significant milestone in the development of GaN materials and devices. GaN films grown utilizing this technique are found to exhibit much lower defect densities resulting in a substantially reduced background electron concentration in the undoped GaN films [43, 44]. By optimizing the buffer layer growth conditions, GaN epitaxial films can be improved with background carrier concentrations down to the order of  $10^{16}$   $\text{cm}^{-3}$ . It is also important to note that substantial improvement in the film crystallinity is observed with the use of such a nucleation layer for MBE-grown materials as well.

### 2.2.2 MBE Growth of III-nitrides

The MBE process is a state-of-the-art ultrahigh vacuum (UHV) thin film deposition technique. Such UHV conditions enable the growth of semiconductor epitaxial layers with high purity. In addition, due to the ultra-high vacuum environment for its growth process, a number of in-situ monitoring techniques have been developed for effective control of the growth parameters. This greatly facilitates the understanding of the growth mechanism and optimization of the growth parameters. As a result, the MBE process has been employed for the growth of highly sophisticated devices such as surface emitting cavity lasers and modulation doped field effect transistors [6, 7, 9, 45-47]. A schematic diagram of a typical MBE system is shown in Fig. 2.5.

Elements are contained in pyrolytic boron nitride (PBN) crucibles which are heated by tantalum (Ta) heating coils inside the Knudsen cells. The temperatures of the individual Knudsen Cells are measured using K type thermocouples which are used as input parameters for controlling the output power delivered by the Eurotherm programmable power supplies to the Ta heaters. The vapour pressure of the individual element is a strong function of the cell temperature. Hence, close monitoring of the cell temperature enables one to achieve detailed control of the growth rates of the films. The growth time of each element is accurately controlled by individual shutters placed at the opening of the PBN crucible.

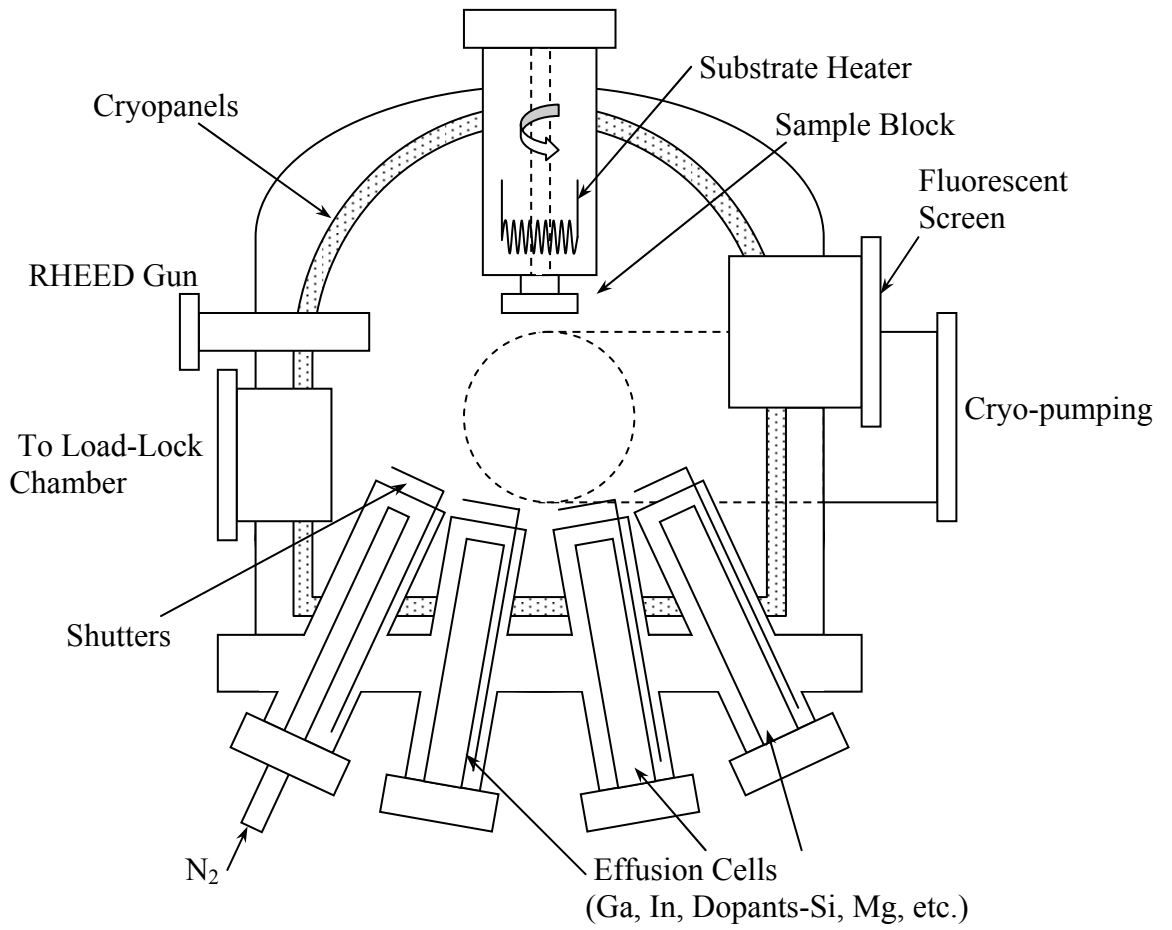


Figure 2.5: Schematic diagram of an MBE system.

Since MBE is a UHV process, in-situ surface characterization techniques such as the reflection high-energy electron diffraction (RHEED) and the gas analysis process such as the quadrupole mass spectrometry can be incorporated into the growth chamber. These in-situ analyses methods are important in the characterization and optimization of the growth process. The MBE process is usually performed in relatively low temperatures of around 650°C–800°C. To facilitate efficient growth of GaN, the nitrogen species has to be activated. This is because molecular nitrogen is inert, due to the strong N-N bond, and does not chemisorb on the GaN surface below 950°C. Common techniques for the activation of the nitrogen species are accomplished by radio frequency (RF) or electron cyclotron resonance microwave (ECR) plasma sources. Alternatively NH<sub>3</sub> can be used as the nitrogen source, as in the case of the ammonia-MBE system. Solid sources of Ga, In, Al, Mg and Si are typically used for the growth of the III-nitride alloys. Particularly, Mg and Si are used for p- and n-doping respectively.

In the case of MOCVD-growth of III-nitrides, a thin buffer layer is typically deposited prior to the growth of the epitaxial layer in the MBE nitrides growth process. Other techniques have also been used for MBE growth to improve the quality of the resulting GaN films. These include migration enhanced epitaxy (MEE), AlN-GaN superlattice intermediate layers, and the use of surfactants during growth [48-50].

The MBE process is widely used for academic research purposes and commercial device production. This matured technology has been transferred to production-scale manufacturing of optoelectronic and electronic devices. In fact, the first blue-violet InGaN laser diodes were realized on bulk GaN substrates grown by the plasma-assisted

MBE system, which is the key element of the blue-ray DVD high density storage. High electron mobility transistors (HEMTs) for use in satellite broadcasting systems are also produced by MBE technology [6, 7, 33, 47]. All these examples indicate that MBE plays a vital role in thin film growth technology.

### **2.3 Application of Buffer Layers for Improved GaN Film Quality**

Until the development of buffer layers, the quality of GaN films grown directly on sapphire was very poor. The film surface was found to be very rough with high rms roughness and the formation of hillocks was exhibited. Also, significant yellow emission was observed in the luminescence spectra. With the application of a AlN or GaN buffer layer, prior to the growth of the epitaxial layer, the quality of the GaN layer was found to improve substantially [43, 44]. Although this technique was originally developed for MOCVD growth of GaN films, its implementation, in a modified version, in the MBE-growth process proved highly beneficial.

The purpose of the buffer layer is to optimize the transition between the sapphire substrate and the GaN active layers. The buffer layer provides a higher nucleation site density and allows the top GaN layer to deviate somewhat from the surface arrangement of the underlying sapphire substrate. This allows the nitride layer to assume its own structure. The strain is accommodated by twisting, tilting and prismatic growth with the objective of reducing the interface defect density as much as possible. The application of buffer layers in MBE growth has also resulted in the improvement of the quality of

the GaN epitaxial layers. However, it is found that the strain between the buffer and the underlying substrate is relatively strong for MBE growth, which partly accounts for the less drastic improvements in MBE-grown GaN films.

The initial stage of film growth is crucial in determining the resulting quality of the top epitaxial layer. There are three cases of epitaxy: i) two-dimensional (2D) layer-by-layer; ii) three-dimensional (3D) island mode, and the mixed (M) mode in which the 2D growth is followed by island formation. The 2D growth mode gives smooth surface morphology while the other two result in surfaces with high roughness. The growth mode is determined by various parameters such as the interfacial energy of the solid and vapor phases and the interfacial energy of the vapor phase and the substrate, rate of impingement of species and surface migration of reactants etc.

The evolution of the film is illustrated in Fig. 2.6. The thin buffer layer is first deposited on the substrate and this layer is amorphous at the deposition temperature. However, as the temperature is ramped towards the growth temperature of the epitaxial layer, it is crystallized and exhibits a columnar structure. The initial GaN layer deposited on top of the buffer layer is found to possess crystalline structures resembling that of the buffer layer. Each GaN column originates from a GaN nucleus formed on top of an buffer layer's column. The columns have disordered orientations and as the base of each column increases in area, the number of columns at the growth surface also decreases accordingly.

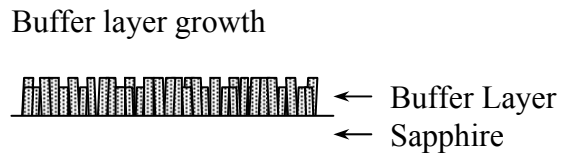
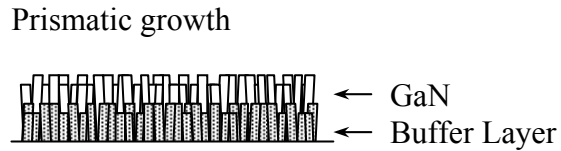
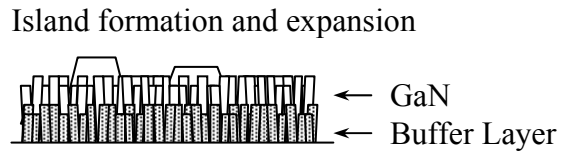
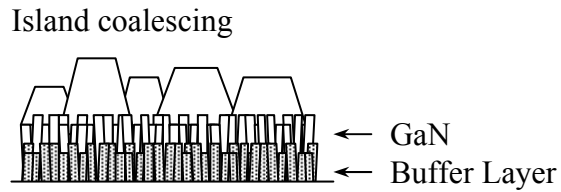
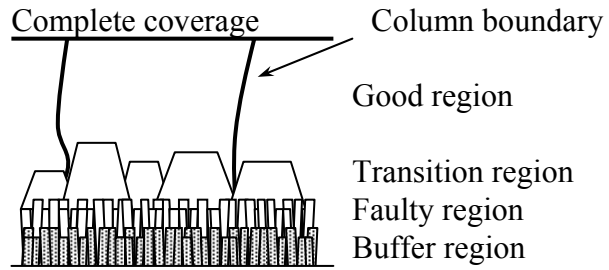


Figure 2.6: Evolution of GaN film growth.

The prismatic growth leads to alignment along the c-axis in general but with some misorientation for each column. As the thickness increases, the relative “twist” and “tilt” between columns appear to decrease giving rise to a more orderly structure as growth proceeds. Figure 2.7 illustrates the microstructure of GaN grown on sapphire. As the growth proceeds, the islands coalesce to form larger grains. Finally, as the crystallographic directions of the islands are within a few degrees of each other, a smooth GaN layer with reduced number of defects may be formed.

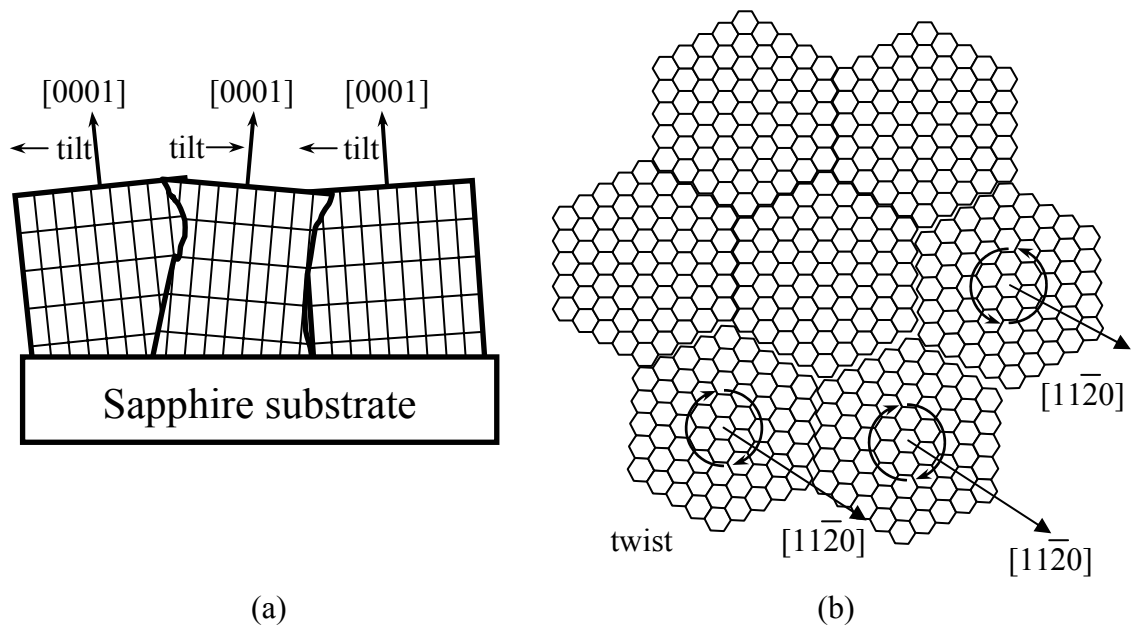


Figure 2.7: Microstructure of GaN grown on sapphire. (a) side view showing tilt for individual grains in the  $[0001]$  direction; (b) Plan view showing twist in the  $[11\bar{2}0]$  direction.

In 2000, Fong *et al.* [30, 51] first reported the use of a new buffer layer system for the MBE growth of GaN in which an intermediated-temperature buffer layer (ITBL) is used in addition to the conventional buffer layer. This technique yielded high quality GaN epitaxial layers. It was found that the ITBL serves to relax the residual strain due to the large lattice and thermal mismatches between the GaN and sapphire substrates and hence substantially improves the quality of the GaN. Detailed experimental results on the reliability study of photodiodes fabricated on GaN with ITBL structure is given in Chapter 5.

## **Chapter 3**

# **Schottky Contact UV Photodiodes: Operation Principles and Fabrication Processes**

### **3.1 Introduction**

Short wavelength ultraviolet (UV) photodetection is important for many applications. For instance, ultra high density storage, such as second generation DVD storage, requires fast and low-noise detection mechanisms. For such applications, a high-speed photodetector with high sensitivity, low capacitance, and low noise at the operating wavelength is required. To meet these requirements, various types of photodetectors have been proposed. Among these, the Schottky photodiodes are particularly attractive because of their high speed operation and ease of fabrication. This is because the photo-generated carriers are efficiently collected within the depletion region at the metal/semiconductor junction and the operation is not affected by minority carrier diffusion [22-24]. Also, both high-quality Schottky and ohmic contacts to GaN can be achieved using the standard e-beam evaporation technique [21, 52-56]. These make

Schottky photodiodes particularly attractive among the various types of proposed photodetector structures.

### **3.2 Theory of Rectifying Metal Semiconductor Contacts**

Knowledge of metal/semiconductor contacts can be traced back to 1874 in the early work of F. Braun, who discovered the asymmetric nature of electrical conduction between metal contacts and semiconductors [57]. Although the rectification mechanism was not well understood at that time, detectors such as metal point contacts on metallic sulphides were used extensively in early experiments on radio. The following presents the fundamentals of the Schottky contacts.

In 1938 Schottky and Mott [58, 59] independently suggested a model for the rectification mechanism. They pointed out that the observed direction of rectification could be explained by supposing that electrons passed over a potential barrier through the normal process of drift and diffusion. The basic theory of rectifying metal semiconductor contacts is now presented, and follows reference [60] to a great extent and relies to some extent on reference [61]. A more comprehensive description is provided in theoretical work by E. H. Rhoderick and R. H. Williams [60]. Figure 3.1 shows a schematic diagram of the energy band structure of an unbiased metal/n-type semiconductor Schottky contact.

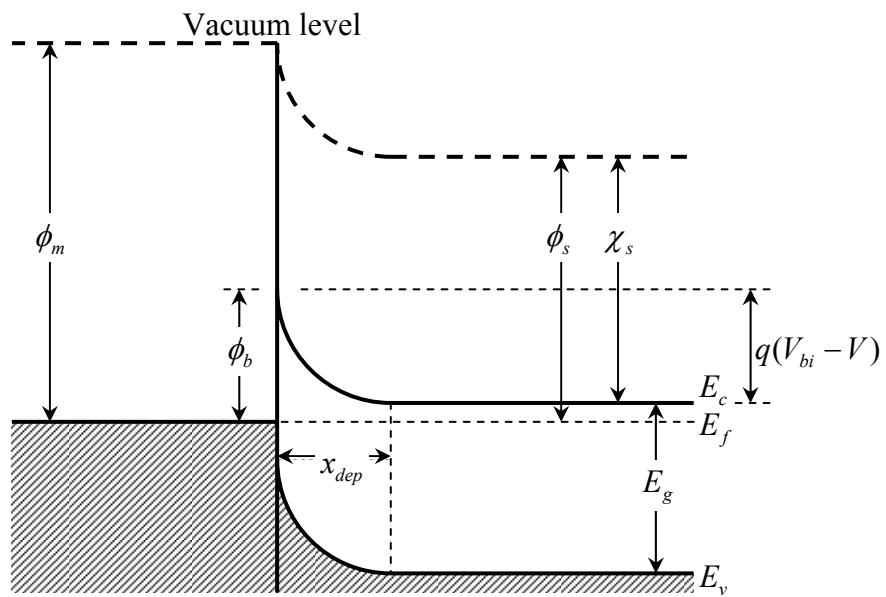


Figure 3.1: Schematic energy band structure of an unbiased metal/n-type semiconductor Schottky contact.

According to the Schottky-Mott theory, the barrier height at zero bias,  $\phi_b$ , referenced to the Fermi level, is

$$\phi_b = \phi_m - \chi_s \quad (3.1)$$

where  $\phi_m$  is the work function of the metal,  $\chi_s$  is the electron affinity of the semiconductor, which is expressed as

$$\chi_s = \phi_s - (E_c - E_f) \quad (3.2)$$

in which  $\phi_s$  is the work function of the semiconductor,  $E_c$  is the conduction band edge and  $E_f$  is the Fermi level. While  $\phi_b$  is the barrier encountered by electrons in the metal, the built-in energy  $qV_{bi}$  where  $q$  is the charge of electron, is the potential barrier encountered by electrons in the semiconductor and is given by:

$$\begin{aligned} qV_{bi} &= \phi_m - \phi_s \\ &= \phi_b - (E_c - E_f) \end{aligned} \quad (3.3)$$

This model describes a rather simple situation as it assumes ideal conditions whereby dipole surface contributions and the electron affinity are thought to be unchanged when metal comes into contact with the semiconductor. It further assumes that there are no chemical reactions or physical strains created when they are brought into contact. In practice, however, surface dipole layers do exist on the semiconductor's surface. This is because the atoms at the surface of semiconductors have neighbours on one side only

and hence an unpaired electron in a localized orbital, directed away from the surface occurs. Such an orbital is often called a dangling bond, and this causes a distortion of the electron clouds of the surface atoms, such that the centers of the positive and negative charges do not coincide.

Also, it was found that the barrier height,  $\phi_b$ , often does not depend on  $\phi_m$  in some cases, which contradicts Eq. 3.1. Such a weak dependence of  $\phi_b$  on  $\phi_m$  was explained by the existence of localized surface states. The surface states are continuously distributed in energy within the forbidden gap and are characterized by a level,  $\phi_o$ , such that if the surface states are occupied up to  $\phi_o$  and empty above  $\phi_o$ , the surface is electrically neutral. If the level  $\phi_o$  happens to be above the Fermi level,  $E_f$ , the surface states contain a net positive charge and the amount of band bending will be decreased. The reduction in  $\phi_b$  has the effect of pushing  $\phi_o$  towards  $E_f$ , i.e. it tends to reduce the positive charge in the surface states. On the other hand, if  $\phi_o$  happens to be below  $E_f$ , the band bending will be increased and hence  $\phi_o$  will be pulled up towards  $E_f$ . This acts as a negative-feedback loop and ultimately stabilizes when  $\phi_o \approx E_f$ . In this case, the barrier height will be given by  $\phi_b \approx E_g - \phi_o$ , where  $E_g$  is the bandgap of the semiconductor, and is called the Bardeen limit. The barrier height is said to be ‘pinned’ by the high density of surface states.

In practice, a thin oxide layer often exists between the metal and the semiconductor, so the charge in the surface states together with its image charge on the surface of the

metal, will form a dipole layer. As a result, this dipole layer will alter the potential difference between the semiconductor and the metal. Thus, the modification to the Schottky-Mott theory is shown as follows:

$$\phi_b = \gamma(\phi_m - \chi_s) + (1 - \gamma)(E_g - \phi_o) \quad (3.4)$$

where  $\phi_o$  is the position of neutral level referenced to the top of the valence band, and  $\gamma$  is the slope of the linear relationship between Schottky barrier height and metal work function given by:

$$\gamma = \frac{\varepsilon_i}{\varepsilon_i + q\delta D_s}, \quad (3.5)$$

in which  $\varepsilon_i$  is the permittivity of the oxide layer,  $\delta$  is the thickness of the oxide layer, and  $D_s$  is the density of surface states. If surface states are absent, i.e.  $D_s = 0$  and  $\gamma = 1$ , Eq. 3.4 becomes identical to the original Schottky-Mott model as indicated in Eq. 3.1. If the density of surfaces states is very high,  $\gamma$  becomes small and  $\phi_o$  approaches the Bardeen limit. This is because a very small deviation of the Fermi level from the neutral level can produce a large dipole moment, which stabilizes the barrier height by a negative feedback effect.

### 3.2.1 Current Transport Mechanisms in the Schottky Diode

#### *Thermionic Emission*

The current transport through the device by emission over the barrier is basically a two step process: first the electrons must move through the depletion region, which is governed by the usual drift and diffusion processes; secondly they will pass over the barrier into the metal and this is controlled by the density of available states in the metal. The current-voltage characteristics given by the thermionic emission theory is expressed as:

$$I = AA^{**}T^2 \exp\left(-\frac{\phi_b}{k_B T}\right) \exp\left(\frac{qV}{nk_B T}\right) \left[1 - \exp\left(-\frac{qV}{k_B T}\right)\right] \quad (3.6)$$

which reduces to the following expression when the applied voltage  $V$  greater than  $3k_B T$ :

$$I = AA^{**}T^2 \exp\left(-\frac{\phi_b}{k_B T}\right) \exp\left(\frac{qV}{nk_B T}\right) \quad (3.7)$$

where  $A$  is the cross-sectional area of the metal-semiconductor interface,  $A^{**}$  is the Richardson constant for metal-semiconductor interface,  $T$  is the absolute temperature in Kelvin,  $k_B$  is the Boltzmann constant, and  $n$  is the ideality factor.

The current transport described by Eq. 3.7 is commonly referred to as the “thermionic emission” current. The ideality factor in the equation gives a measure of the quality of the junction, which is highly process dependent. In practice, the presence of

non-ideal effects or mechanisms other than thermionic emission will lead to an increase in the ideality factor above one, such as, image force lowering, generation-recombination in the depletion region and tunneling via interfacial states etc. [62-64].

### *Quantum Mechanical Tunneling*

For a heavily doped semiconductor at a low temperature, the current arising from the quantum mechanical tunneling of carriers through the barrier becomes the dominant transport process. The tunneling current  $I_{tn}$  can be expressed by:

$$I_{tn} = I_{ms} \left[ \exp\left(\frac{qV}{E_o}\right) - 1 \right] \quad (3.8)$$

where  $I_{ms}$  is the tunneling saturation current, and  $E_o$  is the tunneling constant. The tunneling saturation current can be expressed as a function of temperature, barrier height and semiconductor parameters. Padovani and Stratton [65] further derived the  $E_o$  as:

$$E_o = E_{oo} \coth\left(\frac{E_{oo}}{k_B T}\right) \quad (3.9)$$

where,  $E_{oo}$  is the tunneling parameter related to the material properties of the semiconductor and is expressed as:

$$E_{oo} = \frac{qh}{4\pi} \sqrt{\frac{N_D}{m_e^* \epsilon_s}} \quad (3.10)$$

in which  $h$  is Planck's constant,  $N_D$  is the n-type impurity doping concentration with the assumption that all the donors are ionized,  $m_e^*$  is the effective mass of an electron and  $\epsilon_s$  is the permittivity of the semiconductor.

### *Leakage Current*

Another small but finite current, parallel to the carrier transport mechanism mentioned above, is the leakage current. This is usually found in practical devices. It is caused by surface leakage and can be significantly reduced by optimizing the design and fabrication conditions. An example of the creation of such leakage path is the plasma dry etching processes used in devices fabrication. Such processes create a damaged layer on the etched sidewall due to the energetic particles involved in the etching processes. The major effect of such damaged layer is the creation of alternative conduction path in addition to the device active region and leading to the increase of leakage current. In practice, this component is modeled by a large by-pass resistor,  $R_{leakage}$ , connected in parallel to the metal-semiconductor junction. The leakage current can be expressed as:

$$I_{leakage} = \frac{V}{R_{leakage}} \quad (3.11)$$

### 3.3 Principles of Optical Detection

There are two main mechanisms of photo detection using the semiconductor photodiode devices. Electron excitation from the valence band to the conduction band is referred to as intrinsic absorption, while in extrinsic detectors, excitation involving impurity centers within the band gap of the material and is known as extrinsic absorption. Due to intrinsic absorption's greater efficiency and faster response time, it is the one on which interest is generally centered [66].

Figure 3.2 shows the energy band diagram of a metal/semiconductor junction under photon illumination. When incident radiation with energy larger than the bandgap irradiates the semiconductor material, electrons will be excited to the conduction band from the valence band. The absorption layer, which is situated directly underneath the metal contact, is usually lightly doped to maximize the depletion width, and thereby enhancing the quantum efficiency of the devices. Furthermore, the semi-transparent metallic layer that makes up the Schottky contact is kept as thin as possible to minimize the number of photons absorbed in it. The electron-hole pairs are then swiftly separated by the built-in field within the depletion region giving rise to a photocurrent.

The speed of response of such a device depends on the transit time of the photo-generated carriers across the depletion region, the junction capacitance and parasitic circuit elements. For high-speed operation, the Schottky barrier photodiode requires a narrow depletion region for a small transit time, however on the other hand a wide

depletion region and a small area will give a low junction capacitance. Therefore, the geometry and dimensions of a photodiode, as well as the dopant concentration of the epilayer, have significant roles in determining the diode's speed and sensitivity [67-69]. Hence, the device structure has to be carefully optimized to meet the specific requirements for high-speed application.

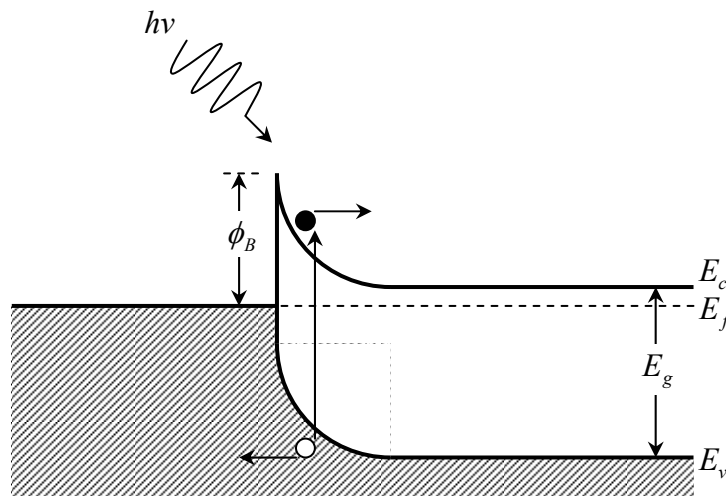


Figure 3.2: The energy band diagram and photocurrent generation mechanisms of a Schottky junction under zero bias.

### 3.4 Advantages of Wide Bandgap Schottky UV Photodiodes

GaN is an attractive candidate for the development of short wavelength optoelectronic devices. One of the major advantages of GaN over the Si and GaAs counterparts is its wide and direct bandgap [17, 33, 34]. Si and GaAs have narrow bandgaps (1.12 eV and 1.43 eV respectively) and therefore a filter is required to stop low energy photons, the visible and infrared part of the spectrum, so as to operate in the UV regions only. In contrast, the bandgap of GaN (3.4 eV) and its related alloys have much larger bandgaps. Hence, detectors fabricated with the GaN material can operate without additional filtering, which is an obvious advantage over Si and GaAs, for which filtering can be bulky and expensive.

GaN is also a direct bandgap material as opposed to Si which has an indirect bandgap. Figure 3.3 shows the dispersion curve diagram for both direct bandgap and indirect bandgap materials. The electrons (and holes) are treated as waves with wavelength  $\lambda = 2\pi k$ , and the band diagram gives the energy ( $E$ ) of the electrons (and holes) as a function of the wavevector  $k$  (or momentum). For indirect bandgap semiconductors, electron transition between the top of the valence band and the bottom of the conduction band requires not only a change in the electron energy but also in the electron momentum. Thus the absorption process will require not only a photon but also the participation of a phonon. For photon energies well above the bandgap, this can be accomplished relatively efficiently by the excitation of an electron directly to a higher

energy level in the conduction band, and then relaxing back to the bottom of the band and the difference in the energy is released as heat. But for light energies closer to the bandgap, a phonon is required for momentum transfer to accomplish the non-vertical excitation process, resulting in lower efficiency. The total effect is a substantially reduced spectral response compared to a direct bandgap semiconductor. For a direct bandgap semiconductor, the quantum efficiency is much higher and response peaks at the bandgap energy and drops off sharply for sub-bandgap illumination.

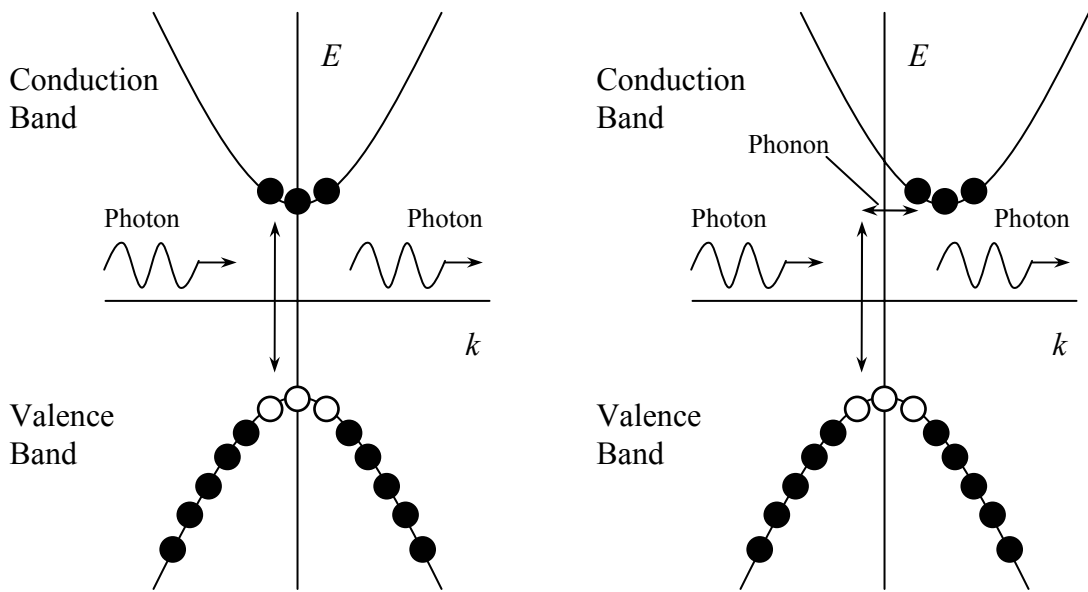


Figure 3.3: Dispersion curve diagrams ( $E$  versus  $k$ ) for both direct bandgap (left) and indirect bandgap (right) materials. Visualizations of the generation and recombination of electron and hole in both types of semiconductors are shown with the photon and phonon transitions processes.

Schottky diode structures also provide several advantages over other types of detector structures such as p-n and p-i-n diodes. Growth of a p<sup>+</sup> GaN layer and formation of p<sup>+</sup> ohmic contacts with low contact resistance are two challenging issues for GaN based p-n and p-i-n type photodiodes, while Schottky photodiodes do not suffer from these problems [24, 70-73]. Both high quality Schottky and n-type ohmic contacts can be achieved by well established processes [21, 53, 54, 56, 64, 74]. Also, fabrication of coplanar p-n or p-i-n diodes requires mesa etching. The etching of III-nitride material is generally done by a dry etching method such as reactive ion etching (RIE) or inductively coupled plasma (ICP) etching. However, dry etching usually comes with some unwanted side effects on the etched samples. The most undesirable of these is that the etching surface and the sidewall are usually damaged by energetic particles created during the etching process. A higher concentration of defects or trap density is introduced on the damaged surface, which increases the noise and provides a leakage path, thereby substantially increasing the leakage current [75, 76]. In addition, impurity contamination can be serious as the internal surfaces of the etching systems are subject to ion bombardment and can be sputtered. These sputtered materials may deposit on the sample surfaces and be incorporated in the device being etched [77].

The fabrication processes of the Schottky photodetector is relatively less complicated. The major processes involved in Schottky diodes fabrication are the metallization and photolithography for device patterning. These processes are well established and controllable to produce high quality Schottky diodes [52, 53].

In terms of device operation, Schottky diodes are particularly attractive for high speed operation. Since there is an inherent absence of slow components associated with minority carrier diffusion, the photo-carriers are generated and efficiently collected within the depleted active layer of the Schottky diode. Schottky diode devices operating at frequencies of GHz have been demonstrated in the literature [22, 23].

Thus, combining the advantage of a direct widegap material and the Schottky photodiode structure, GaN Schottky contact UV photodiodes should be capable of operating at high frequencies, short wavelengths and be suitable for extreme environment, such as in space applications.

### **3.5 Fabrication and Processes of Ni/n-GaN UV Photodiodes**

In this section, all the major steps involved in the fabrication of the Ni/n-GaN UV detectors will be described. The Schottky contact photodiode structure is used to fabricate the detectors. The cross sectional schematic diagram of the Ni/n-GaN Schottky barrier photodiode is shown in Fig. 3.4.

As evidenced from the structure, the device consists of a Schottky contact and an ohmic contact fabricated on top of an n-GaN epi-layer. Hence, the growth of a high-quality GaN layer is crucial to the development of a high quality GaN-based UV detector. This is the main challenge in the fabrication of GaN-based detectors [26-29, 78]. In the following sections, the processes involved in the fabrication of the GaN-based UV detector will be examined. This includes the MBE growth of GaN epitaxial layer which was deposited on top of a novel double buffer layer structure; the electron-beam deposition and photolithography technique. The complete fabrication steps of the Ni/n-GaN Schottky barrier UV detector is also presented at the end of this section.

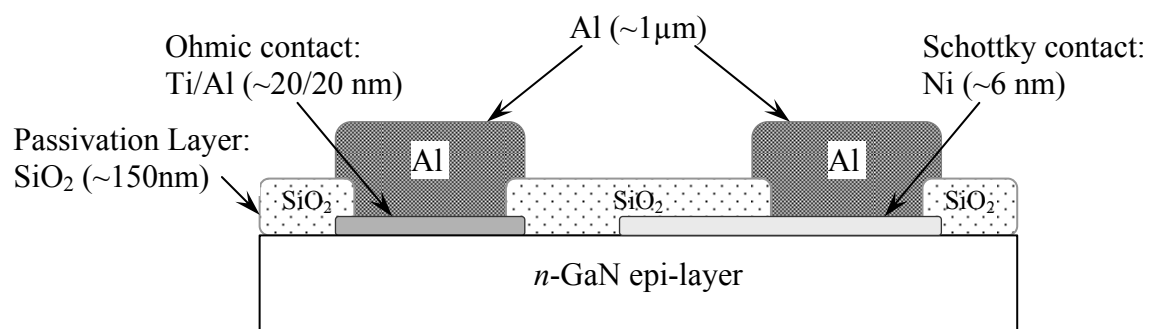


Figure 3.4: Device cross sectional view of the Ni/n-GaN Schottky photodiode.

### 3.5.1 GaN Film Epitaxy

#### *Molecular Beam Epitaxy Growth of GaN films for Schottky Contact Photodiodes*

In this study, UV detectors were fabricated on GaN films grown by an SVT model 35N radio frequency plasma assisted molecular beam epitaxy (RF-PAMBE) system. One of the key advantages of MBE growth is the ability of in-situ monitoring of the growth process with the use of a reflection high-energy electron diffraction (RHEED) system. Hence the growth can be controlled at the monolayer (ML) scale by monitoring the growth surface conditions and optimization of the growth parameters. This makes MBE a superior technique for growing superlattices and multiple quantum well structures [6, 7, 46, 47].

The MBE system used for the growth of GaN materials in this study consists of a load-lock chamber and a main growth chamber, and the two chambers are isolated from each other by a UHV gate valve. The load-lock chamber is pumped with a Balzers TMU065 turbo molecular pump while the main growth chamber is pumped with a Varian Turbo-V 550 turbo pump and a CTI CryoTorr 8 cryo-pump. The system is kept at a base pressure of  $\sim 5 \times 10^{-10}$  Torr.

High purity elemental Al, Ga, In, and the Mg source are supplied by separate Veeco SUMO cells and Si is evaporated by a conventional Knudson effusion source. The cell temperatures are controlled by Eurotherm 818 temperature controllers which can minimize the fluctuation down to  $\pm 0.1^\circ\text{C}$  with carefully tuned PID (proportional, integral and differential) parameters. A nude ionization gauge controlled by a

Grandville-Phillips 350 ionization gauge controller is used to measure the molecular fluxes arriving at the substrate. The flux monitor can be extended to the growth position to measure the beam equivalent pressure (BEP) from different cells. A plot of the BEP of the Ga cell is given in Fig. 3.5.

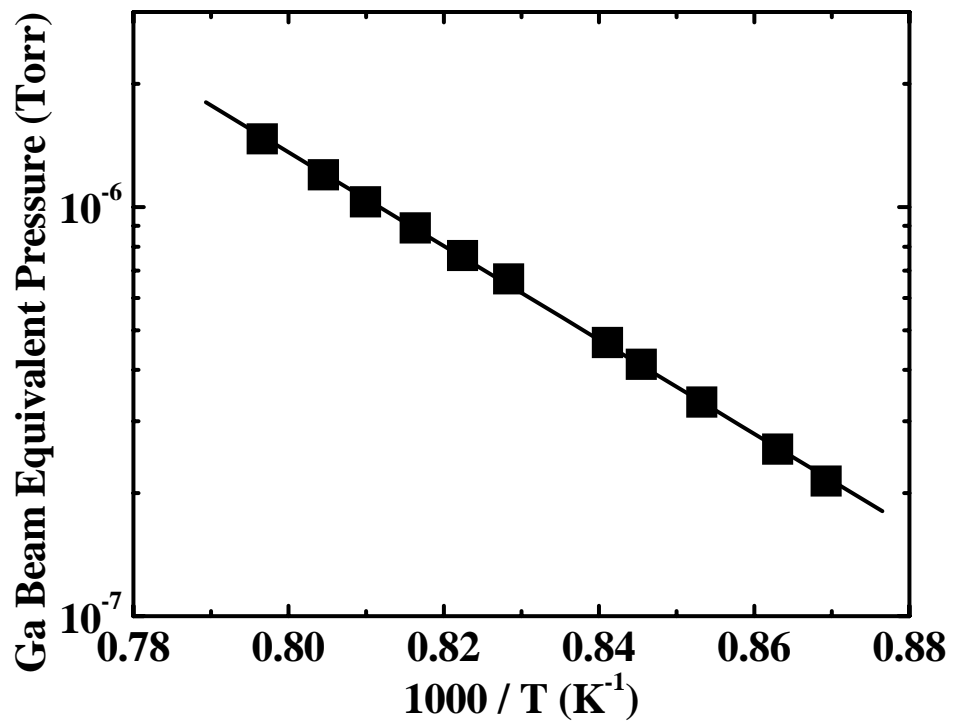


Figure 3.5: Ga beam equivalent pressure measured at different cell temperatures.

The data clearly indicate strong dependence of Ga BEP on the cell temperature. This enables a fine control of the growth rate of the GaN films. High purity nitrogen gas is passed to a Veeco Uni-bulb rf-plasma nitrogen source to supply nitrogen atoms. A 13.56MHz rf power, generated by Advanced Energy RFX-600, is used to create the nitrogen plasma within the range of 250 - 400 W for the activation of the nitrogen species. The nitrogen flow rate is accurately controlled using a MKS 1179A mass flow controller (MFC). The reflected power is minimized by a manual tuning unit to less than 1% of the input power.

The sapphire substrate is mounted on a Veeco molybdenum (Mo) uniblock using custom-made spring plates and then loaded into the load lock chamber. The loading procedure will proceed when the load-lock pressure is below  $\sim 5 \times 10^{-7}$  torr. The substrate holder is transferred to the main growth chamber using a magnetically coupled transfer rod. The molybdenum block is mounted on the manipulator right under the substrate heater which is rotatable and designed to hold substrates up to 3" in diameter. The sample is usually rotated during deposition to ensure the uniformity of the film thickness.

#### *Growth of High Quality GaN Films Utilizing a Double Buffer Layer Structure*

As mentioned in the previous section, due to the large lattice mismatch between the GaN and the Sapphire substrate, high quality epitaxial films cannot be obtained if GaN films are grown directly on the sapphire substrate. In order to accommodate the lattice

mismatch, a conventional GaN or AlN buffer layer is normally utilized. It has been shown that the quality of the films grown utilizing this technique were significantly improved. To further improve the film quality, in this study, GaN epitaxial layers were prepared by a novel technique in which an intermediate-temperature buffer layer was grown prior to the epitaxial layer in addition to the conventional HTBL. The detailed characterizations of the effects of ITBL have been investigated experimentally by Fong *et al.* [30-32, 51, 79-81]. As shown in Fig. 3.6, the photoluminescence (PL) measurement results demonstrate a strong bandedge emission. Furthermore, no detectable yellow band emissions were observed on the sample grown with an ITBL.

The full width at half maximum (FWHM) of the PL spectrum as well as the electron mobilities and PL peak positions for different ITBL thicknesses are shown in Fig. 3.7. As shown in the figure, the GaN film with the highest mobility was obtained with an ITBL thickness of 800 nm. The data show that there is a systematic shift in the PL peak position in addition to the change in the PL intensity. The systematic shift of the peak position of the PL can be explained by the relaxation of the residual tensile strain in the epi-layers. It is suggested that, under typical growth conditions with the use of the conventional buffer layer, the film is under tensile stress due to the mismatch of the lattice constant and coefficient of thermal expansion between sapphire and GaN. However, with the use of the double buffer layer structure, this tensile stress is relaxed at the growth condition. It has been shown that the increase in the compressive stress during growth promoted the 2-D mobility of the adsorbed atoms on GaN surface. This results in the improved crystallinity of the GaN films [51, 82-85]. For the ITBL

thickness beyond 800 nm a rebound in the peak position of the PL is observed, which is indicative of the increase in the residual strain.

These results clearly show that ITBL plays an important role in improving GaN films. In the following chapters, details of the systematic investigation of the properties of Schottky contact UV photodiodes fabricated on GaN epitaxial layers grown utilizing the double buffer layer structure, as discussed above are given.

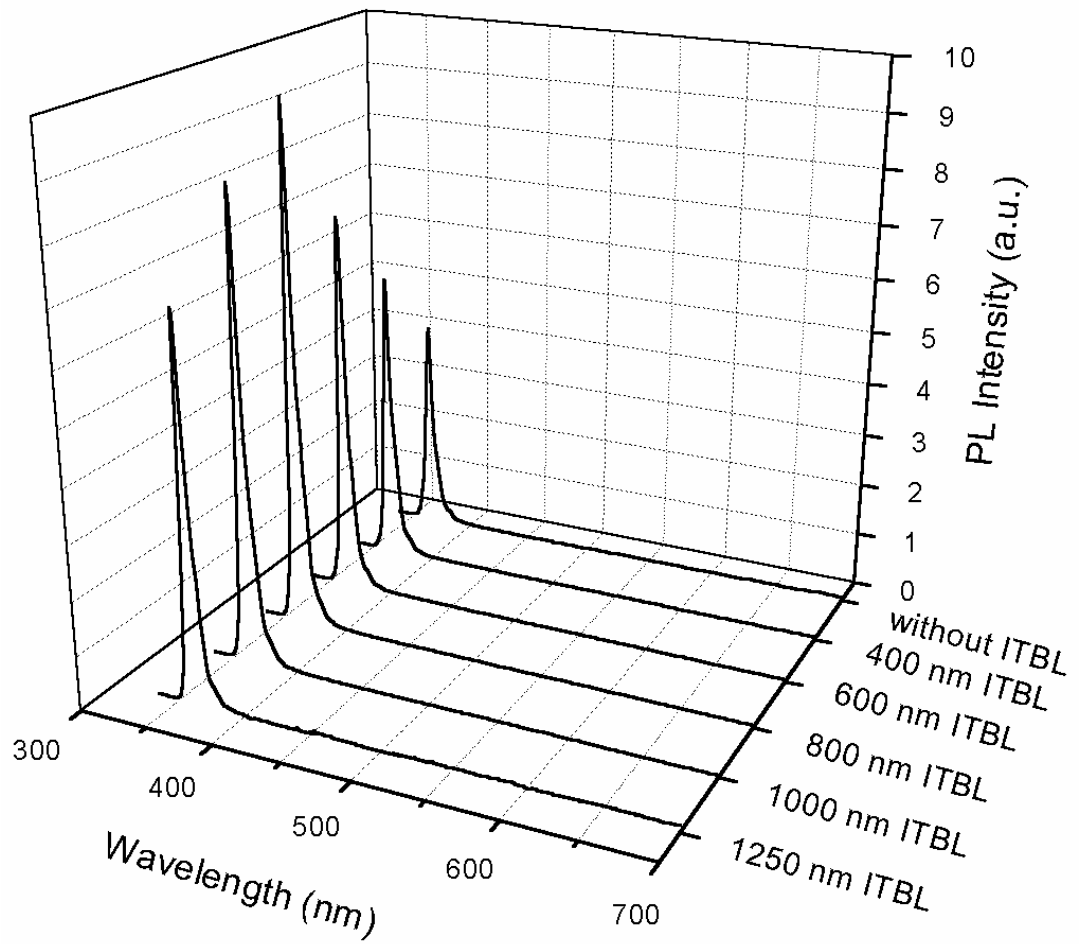
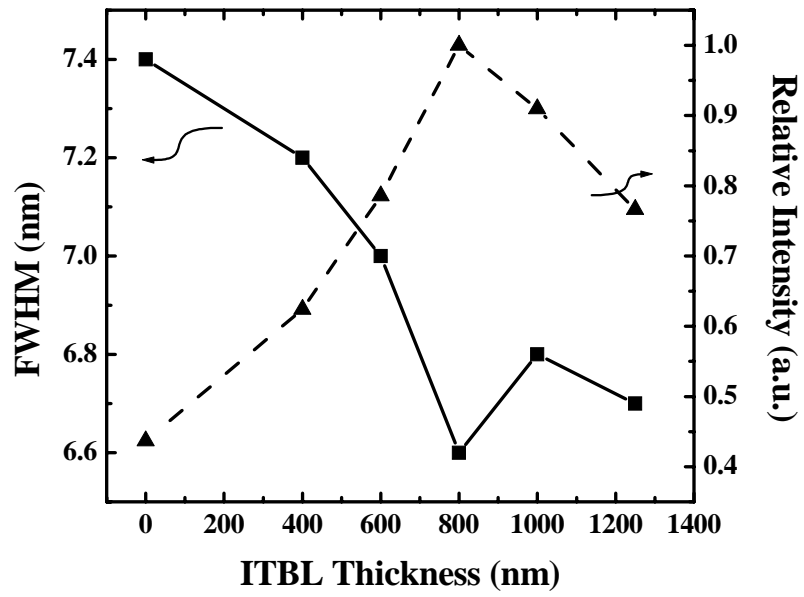
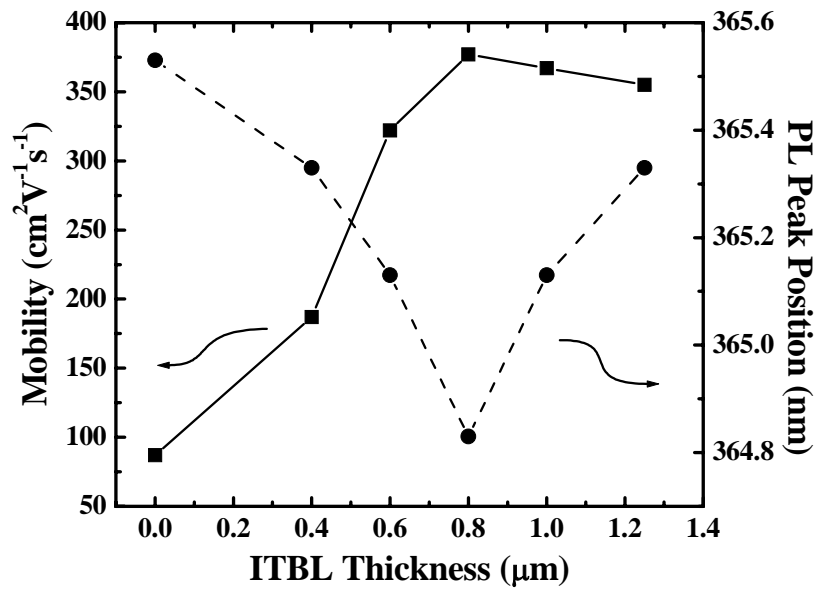


Figure 3.6: The room temperature PL spectra of samples grown with various ITBL thicknesses [79].



(a)



(b)

Figure 3.7: (a) The FWHM and the relative intensity of the bandedge emission of GaN films plotted against the thickness of ITBL; (b) Hall mobility and PL peak position at different ITBL thicknesses [79].

### 3.5.2 Electron-Beam Deposition

#### *Electron-Beam Evaporation*

Evaporation of elemental metal is a crucial process for the formation of Schottky and ohmic contacts of the devices, as well as the bonding pads. All metallization processes and passivation layers in this study were obtained by electron-beam (e-beam) evaporation, which is a fairly straightforward process. Figure 3.8 shows the schematic diagram of an e-beam thin film coating system.

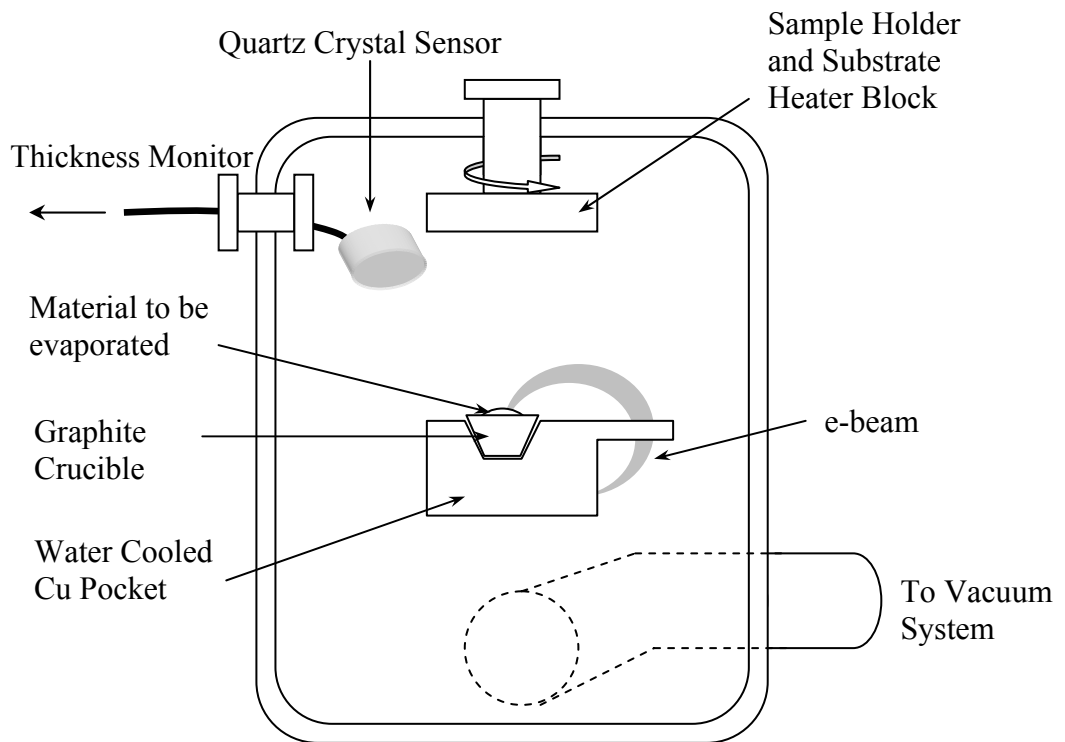


Figure 3.8: Schematic diagram of an e-beam deposition system.

An Edwards 306 automatic electron-beam evaporator was used in this study for the deposition of all the metals and silicon dioxide passivation layers. The deposition chamber was pumped by a Seiko SP301C turbomolecular pump backed by an Edwards mechanical pump. The chamber pressure was monitored by a Pirani gauge at low-vacuum and a Penning gauge for the high-vacuum environment. To obtain high uniformity in the film thickness, substrate rotation was used. The thickness of the film was monitored by a quartz crystal sensor head mounted inside the chamber which was linked to a thickness monitor to give the deposition rate and total thickness.

The process of e-beam evaporation is described as follows. First, the source was placed in a graphite crucible and the base pressure was pump down to below  $4 \times 10^{-6}$  Torr prior to the evaporation. Then high purity material source is heated by a focused electron beam to a sufficiently high temperature for vaporization in a high vacuum. The evaporated atoms will then condense onto a cooler substrate to form a thin film layer.

The advantage of localized heating by an electron beam compared to conventional resistive thermal evaporation is that it can vaporize materials with a high melting point, such as tungsten (melting point 3660 K). However, the deposition rates are slow, of the order of angstroms per second. A fraction of the vapour is scattered as a result of collisions with the surrounding gas molecules inside the evaporation chamber. The mean free path (MFP) is the measure of the average distance traveled between collisions. At a pressure below  $10^{-4}$  Torr, the MFP is larger than the typical size of the deposition chamber. At high vacuum, the atoms do not experience collisions, and therefore they take a line-of-sight path from the source to the substrate. Therefore, a

good vacuum is necessary to ensure a straight line path from the source to the substrate for most of the evaporated species and thus to produce contamination free films.

Table 3.1 lists the materials used in this study, as well as the typical minimum e-beam emission current required to evaporate each of these materials and their corresponding parameters used in the deposition process.

Material	Minimum e-beam Current (mA) (@ 5 kV)	Evaporation Rate ( $\text{\AA} / \text{s}$ )	Working Pressure (Torr)
Ti	95	$\sim 1$	$\sim 3 \times 10^{-6}$
Al	85	$\sim 20$	$\sim 5 \times 10^{-6}$
Ni	100	$\sim 0.5$	$\sim 1 \times 10^{-5}$
SiO <sub>2</sub>	20	$\sim 5$	$\sim 5 \times 10^{-5}$

Table 3.1: List of materials used in the fabrication of UV detectors and their corresponding deposition parameters.

### *Sample Preparation Prior to Deposition*

Since the semiconductor device fabrication process is highly sensitive to contaminants and the surface conditions of the wafer, a standard cleaning procedure was performed on the samples prior to metal deposition and passivation. The samples were first cleaned by acetone followed by 2-propanol in an ultrasonic bath for 5 minutes each. The samples were then rinsed in deionized water and blown dry with filtered nitrogen gas. All the cleaning processes were performed inside a class-1000 clean room. A clean sample surface not only reduces contamination but also promotes stronger metal and photoresist adhesion to the epilayer. After the cleaning process the samples were ready for subsequent fabrication process.

### 3.5.3 Patterning - Photolithography

A standard photolithography technique is used to define the exact dimensions of devices. First a thin layer of AZ3100 positive photoresist, which is a light-sensitive organic polymer, were spun coated on the sample surface for defining the pattern. The thickness of the resist layer is critical and is usually controlled by the spinning speed and duration. The photoresist-coated sample is then soft baked in a conventional oven at 110°C for 1 minute. The resulting photoresist thickness at 4000 rpm for 30 seconds was around 1.4 µm as measured by the step profilometer. A Karl Suss MA6 mask aligner system was then used to expose the pattern. Ultra-violet light produced by a mercury lamp was

shone onto the photoresist layer for 300 seconds through a dark field mask containing the pattern to be transferred. For a positive photoresist, the chemical bonds exposed to UV light are weakened and are subsequently removed using AZ300 photoresist developer solution. After pattern development and rinsing in deionized water, hard baking was performed at 110 °C for 30 minutes for drying and hardening of the photoresist. The patterned photoresist can now serve as a protective layer in the lift-off process or for the wet etching process to stop most of the chemical etchants.

#### 3.5.4 The Device Fabrication Processing Steps

The active region of a GaN-based UV detector consists of a semi-transparent Schottky junction formed by the deposition of a thin Ni layer on top of a slightly n-doped GaN thin film. The n-GaN layers were grown using an rf-plasma assisted MBE system on c-plane sapphire substrates, as described in Section 3.5.1.

Two types of GaN visible blind Schottky contact photodiodes were investigated in this work. Type I devices were fabricated on n-doped GaN epitaxial layers grown with the use of a novel double buffer layer structure that consists of a conventional AlN high temperature buffer layer and a GaN intermediate-temperature buffer layer. In this study of GaN-based UV detectors, an ITBL thickness of 800 nm was chosen for the fabrication of type I devices. This is shown to be the optimal thickness for the ITBL, as discussed above. Type II devices were fabricated on the GaN epi-layer grown using the conventional single AlN buffer layer. This will serve as a control to elucidate the effects

of the double buffer layer structure on the reliability of the devices. Figure 3.9 shows the structure of the films used for the fabrication of the devices.

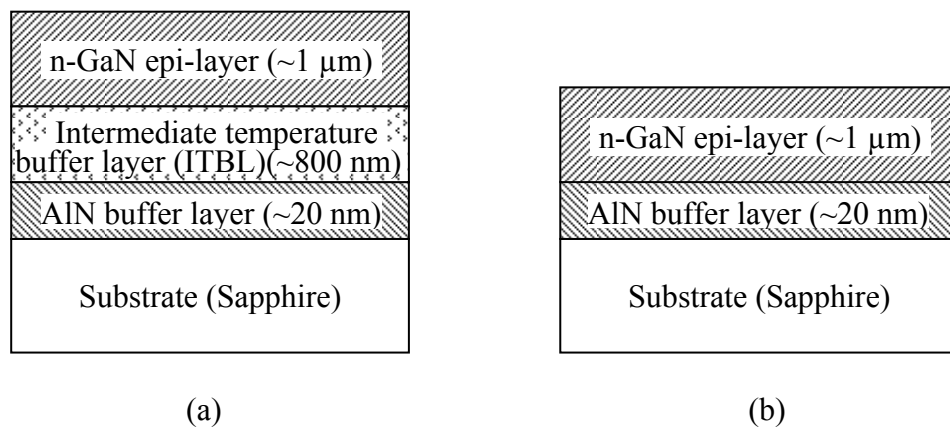


Figure 3.9: The structure of two types of GaN epitaxial layers used for Ni/GaN UV photodiodes fabrication: (a) n-GaN epi-layer with ITBL for the fabrication of type I devices; and (b) n-GaN epi-layer without ITBL for the fabrication of type II devices.

Figure 3.4 illustrates the schematic cross sectional view of a Ni/n-GaN Schottky photodiode. The device consists of a Ti/Al (20 nm/20 nm) ohmic contact, and a semitransparent Ni layer to form the Schottky contact active region to the GaN. First, the ohmic contact is deposited on the GaN epitaxial layer by electron-beam evaporation. The dimensions of the ohmic contact are  $100\ \mu\text{m} \times 100\ \mu\text{m}$  and are defined using standard photolithography process and lift-off techniques, as described in Section 3.5.3. After the deposition of Ti/Al bilayer, the samples were thoroughly cleaned in an ultrasonic bath with acetone, followed by 2-propanol and deionized (DI) water rinses respectively. The sample was then blown dry using filtered nitrogen gas. Rapid thermal annealing (RTA) was subsequently performed at  $800^\circ\text{C}$  for 60 seconds in a nitrogen ambient. A specific contact resistivity,  $\rho_c$ , of approximately  $10^{-4}\ \Omega\text{cm}^2$ , is achieved using this technique.

Following the formation of the ohmic contact, the Schottky contact was fabricated by e-beam evaporation of a thin semi-transparent Ni layer using a 5N Ni pellet source. The active areas were first defined by the standard photolithographic technique followed by the lift-off process. The typical thickness of the semi-transparent Ni layer is 6 nm. A thickness monitor with a crystal oscillator is used for real time monitoring of the thickness of the deposited film. The exact thickness of the Ni layer was calibrated by AFM as shown in Fig. 3.10.

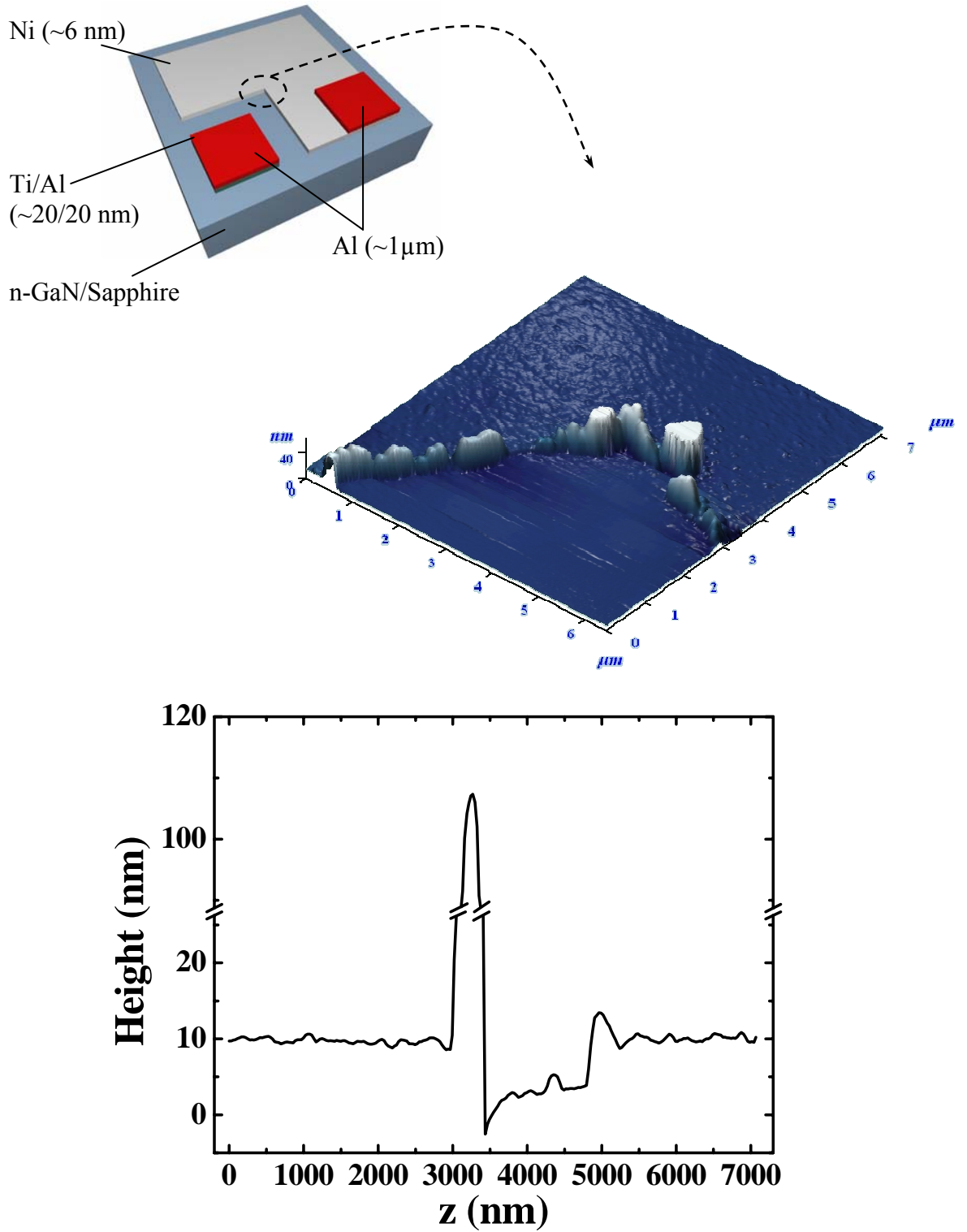


Figure 3.10: AFM results showing the thickness of the deposited Ni layer.

The AFM images were taken by a SOLVER P47H atomic force microscope from NT-MDT Co. The microscope was operated with a Si cantilever probe which has a radius of curvature less than 10nm. A semi-contact mode, with the probe resonating at about 250kHz, was used for the surface topography measurement. As shown in Fig. 3.10, the control sample with Ni deposited on a Si wafer was used to determine the Ni layer thickness. A silicon wafer was used because of its atomically smooth surface and which allowed determination of the thin Ni layer down to a few nanometers. The material on the Ni layer was found to be the photoresist residue after the lift-off process. The measurement results showed that the Ni layer was smooth and thin, and the thickness of this sample was determined to be about 6 nm.

Subsequent to the fabrication of the Schottky contact, a 150 nm thick SiO<sub>2</sub> was deposited on the sample by e-beam evaporation which served as the passivation layer. Two windows were opened by the lift-off process for the metallization of the bonding pads, which consisted of 1 μm thick of Al deposited by e-beam evaporation. The schematic of complete processing steps for the photodiode are illustrated in Appendix.

Once the fabrication process was completed, the devices were scribed, packaged and wire bonded onto a 24-pin DIL ceramic IC header for characterization and optical stressing processes.

## Chapter 4

### Measurement and Analysis Techniques

#### 4.1 Current-Voltage Measurements

Current-voltage ( $I$ - $V$ ) measurement is one of the techniques widely used for device characteristics analysis and parameter extraction, due to the simple experimental set-up and its effectiveness in extracting the device parameters.

Several diode parameters can be extracted from the  $I$ - $V$  measurement results, such as the Schottky barrier height ( $\phi_b$ ), ideality factor ( $n$ ) and reverse saturation current ( $I_s$ ). In practice, most of these parameters are extracted by plotting the  $I$ - $V$  characteristics in a semi-logarithmic plot.

#### 4.1.1 Experimental Setup

The schematic of the  $I$ - $V$  characterization setup is shown in Fig. 4.1. Devices packaged on 24 pin DIL headers were connected to an HP4140B pA meter/DC voltage source via BNC cables. The measurements were taken at room temperature and in a dark environment by placing the device inside a shielded box to eliminate the influence of optical generated carriers on the results. The HP4140B was connected to an IBM compatible personal computer (PC) by an IEEE GPIB interface for automatic control and data transfer. The unit was able to measure the current from as low as  $1 \times 10^{-12}$  A to  $1.999 \times 10^{-2}$  A with  $\pm 1$  count error and provided a stable voltage source output in 10 mV steps. This meant that the HB4140B was capable of making accurate  $I$ - $V$  measurements and measuring small leakage currents. The measurement process was made fully automatic through the use of a Labview program on the PC in which the start, stop, step voltages, ramp rate and delay time between each measurement step could be set via the graphical user interface, depending on the characteristics of the device. The measurements were automatically taken by first outputting the start constant voltage and measuring the series current passing through the device. This was then repeated by increasing the constant voltage source with the step specified and looping until reaching the stop voltage. The measured results are then stored in a computer as an ASCII text file for later analysis. An experimental  $I$ - $V$  result is shown in Figs. 4.2 and 4.3.

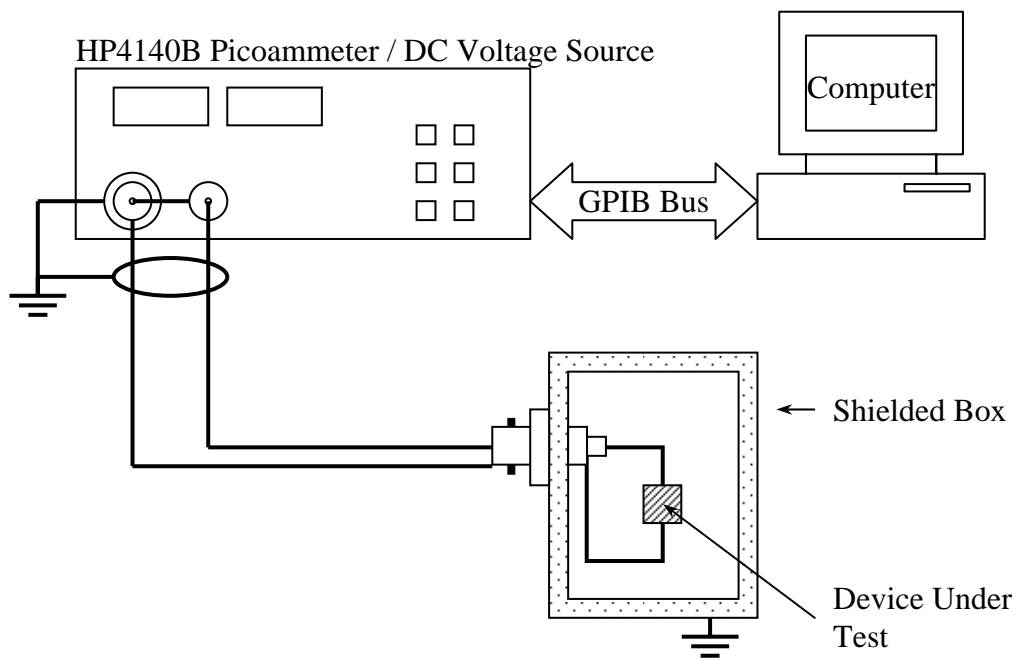


Figure 4.1: Schematic of the  $I$ - $V$  measurement setup.

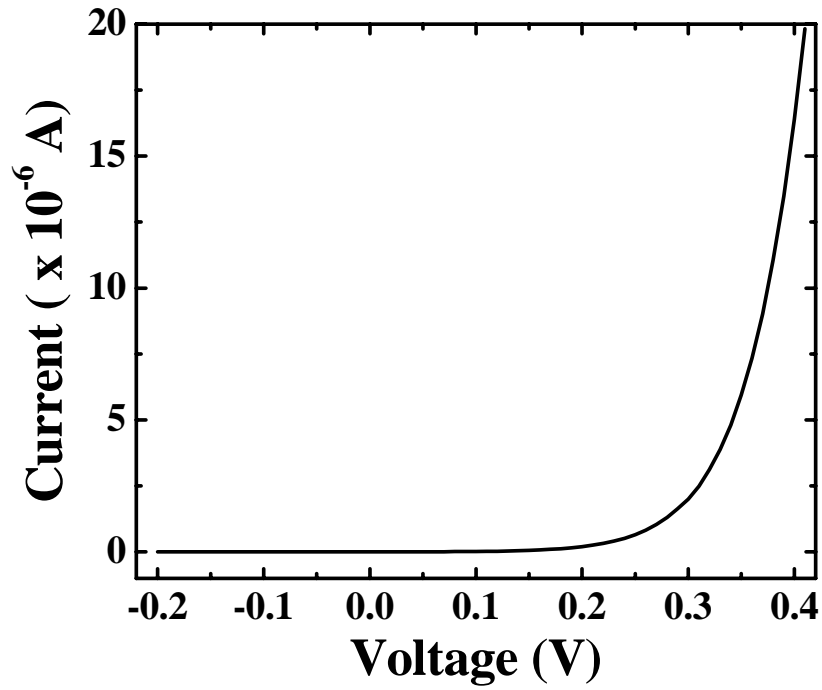


Figure 4.2: Experimental  $I$ - $V$  result of a typical Ni/n-GaN Schottky photodiode.

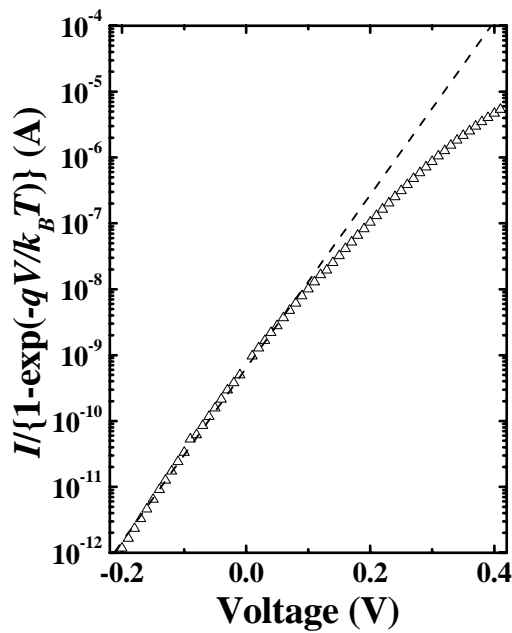


Figure 4.3: Typical  $I$ - $V$  characteristic of a GaN Schottky photodiode plotted in a semi-logarithm of  $I / (1 - e^{-qV/k_B T})$  against the applied voltage  $V$ . Dashed lines shows the linear fitted result for parameter extraction.

As shown in Fig. 4.3, the semi-logarithm of  $I / (1 - e^{-qV/k_B T})$  is plotted against  $V$ . This plot is used because the more exact form describing the  $I$ - $V$  relationship predicted by the thermionic-emission theory should incorporate the term  $(1 - e^{-qV/k_B T})$ , as described in Eq. 3.6, and is reproduced here:

$$I = AA^{**} T^2 \exp\left(-\frac{\phi_b}{k_B T}\right) \exp\left(\frac{qV}{nk_B T}\right) \left[1 - \exp\left(-\frac{qV}{k_B T}\right)\right] \quad (4.1)$$

Although the reduced form of Eq. 4.1, Eq. 3.7, is more often quoted in the literature, the difference is negligible for the a bias voltage  $V$  larger than  $3k_B T/q$ . The correct form of Eq. 4.1 has the advantage that both the ideality factor and barrier height can be found experimentally by plotting  $I / (1 - e^{-qV/k_B T})$  against  $V$ , not only for  $V$  larger than  $3k_B T/q$ , but for the region where  $V$  is smaller than  $3k_B T/q$  and for reverse bias as well [86]. The graph is linear over the whole range from -0.2V to +0.2V which shows that Eq. 4.1 accurately represents the measured data. The deviation from linearity above +0.2V is mainly due to series resistance.

#### 4.1.2 Barrier Height

The Schottky barrier height is defined as the potential barrier to thermionic emission that exists between an intimate metal and semiconductor contact at zero bias. It is assumed that the current transport is dominated by thermionic emission. The barrier

height  $\phi_b$  is extracted by fitting a straight line in Fig. 4.3. The saturation current  $I_s$  is obtained by setting the bias voltage to zero in Eq. 4.1 and hence:

$$I_s = AA^{**}T^2 \exp\left(-\frac{\phi_b}{k_B T}\right) \quad (4.2)$$

Experimentally  $I_s$  can be obtained from y-axis intercept of the fitted line of the  $\ln\{I/(1 - e^{-qV/k_B T})\}$  plot at  $V = 0$ . Thus, the Schottky barrier height is given by:

$$\phi_b = k_B T \ln \frac{AA^{**}T^2}{I_s}. \quad (4.3)$$

The theoretical value for the effective Richardson constant of  $A^{**} = 26.4 \text{ cm}^{-2} \text{ K}^{-2}$  is used throughout this thesis [87-91].

### 4.1.3 Ideality Factor

The ideality factor,  $n$ , gives a measure of the quality of the junction. Using the linear fit in Fig. 4.3, which should be a straight line of slope  $\gamma$ , gives:

$$n = \frac{q}{k_B T} \cdot \frac{1}{\gamma} \quad (4.4)$$

For thermionic emission dominated ideal Schottky junction,  $n$  is close to unity. However, in practice, the ideality factors are always found to deviate from that value. Several different mechanisms may be responsible for the deviation of  $n$  from unity such

as the tunneling process, the presence of an interfacial layer and recombination in the depletion region [62-64].

#### 4.1.4 Series Resistance

A finite series resistance  $R_s$  usually exists in practical devices. This results in the lowering of the effective voltage drop across the barrier and in deviations in the extracted value of the Schottky barrier height. The series resistance is determined from the large forward bias region of the  $I$ - $V$  linear plot where at high current the voltage drop is assumed to be dominated entirely by  $R_s$ . The  $dV/dI$  against  $V$  plotted and  $R_s$  is extracted from the point where this curve reaches a minimum steady value. For the case of larger forward bias  $I$ - $V$  results involved in the analysis, the effect of the series resistance  $R_s$  should be included. To include the effect of the series resistance, the effective voltage across the junction is replaced by  $V - IR_s$ .

## 4.2 Capacitance-Voltage Measurements

The charge in the depletion region of a reverse biased Schottky diode, with a depletion width  $W$ , can be modulated by a small a.c. signal superimposed onto the d.c. biasing voltage. Figure 4.4 below illustrates that the rapid movement of the majority carriers in and out of the depletion region will result in a corresponding variation in the depletion width about its equilibrium value. This is physically analogous to a parallel plate capacitor with a separation of  $x_{dep}$  [92].

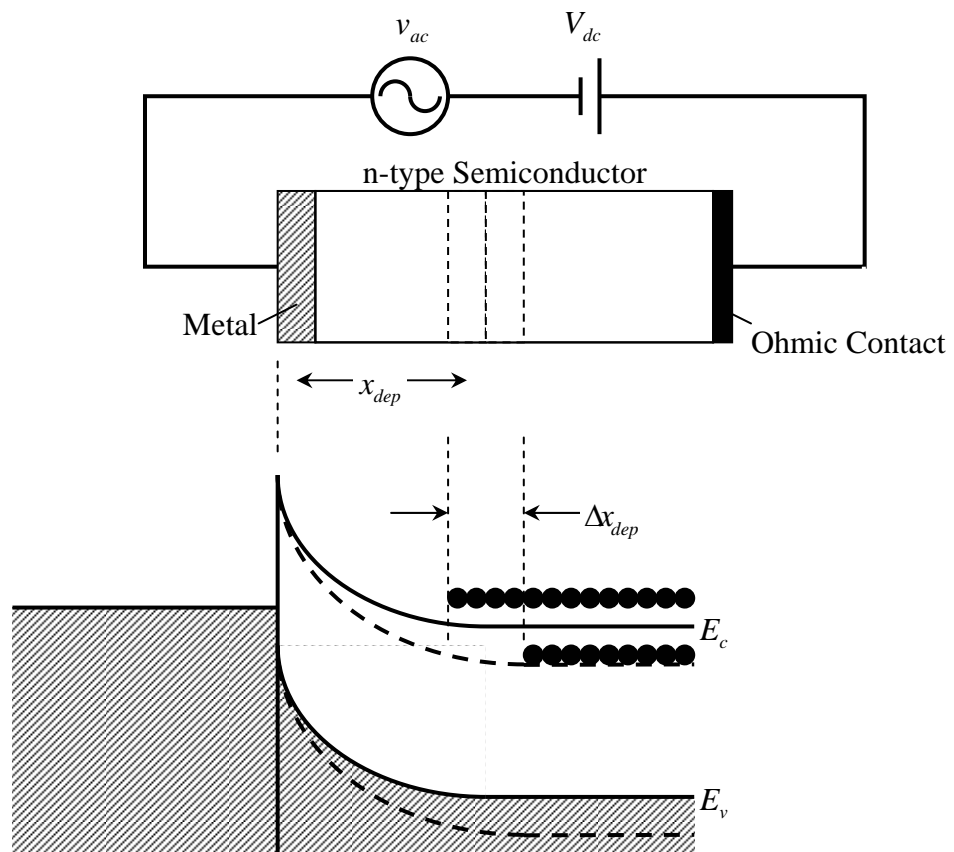


Figure 4.4: Schematic of a reverse biased Schottky barrier superimposed with an ac voltage and the associated charge distribution in energy band diagram.

Hence, the junction capacitance of the devices is given by:

$$C = \frac{\epsilon_s A}{x_{dep}} \quad (4.5)$$

where  $A$  is the diode area and  $\epsilon_s$  is the permittivity of the semiconductor. For a uniformly doped semiconductor, the depletion width is given by:

$$x_{dep} = \left[ \frac{2\epsilon_s}{qN_D} \left( V_{bi} - V - \frac{k_B T}{q} \right) \right]^{1/2} \quad (4.6)$$

where  $V_{bi}$  is the built-in voltage,  $\epsilon_s$  is the permittivity of the semiconductor, and  $N_D$  is the free electron concentration when all shallow donor levels are ionized. The junction capacitance is then given by

$$C = \frac{\epsilon_s A}{\left[ \frac{2\epsilon_s}{qN_D} \left( V_{bi} - V - \frac{k_B T}{q} \right) \right]^{1/2}} \quad (4.7)$$

From Eq. 4.7, one obtains

$$\frac{1}{C^2} = \frac{2}{qN_D \epsilon_s A^2} \left( V_{bi} - V - \frac{k_B T}{q} \right) \quad (4.8)$$

### 4.2.1 Experimental Setup

The experimental setup for the  $C$ - $V$  measurement consisted of a shielded box for housing the device under test, a Boonton 72BD digital capacitance meter and a Hewlett-Packard HP4140B pA meter/DC voltage source. A schematic of the  $C$ - $V$  measurement setup is shown in Fig. 4.5.

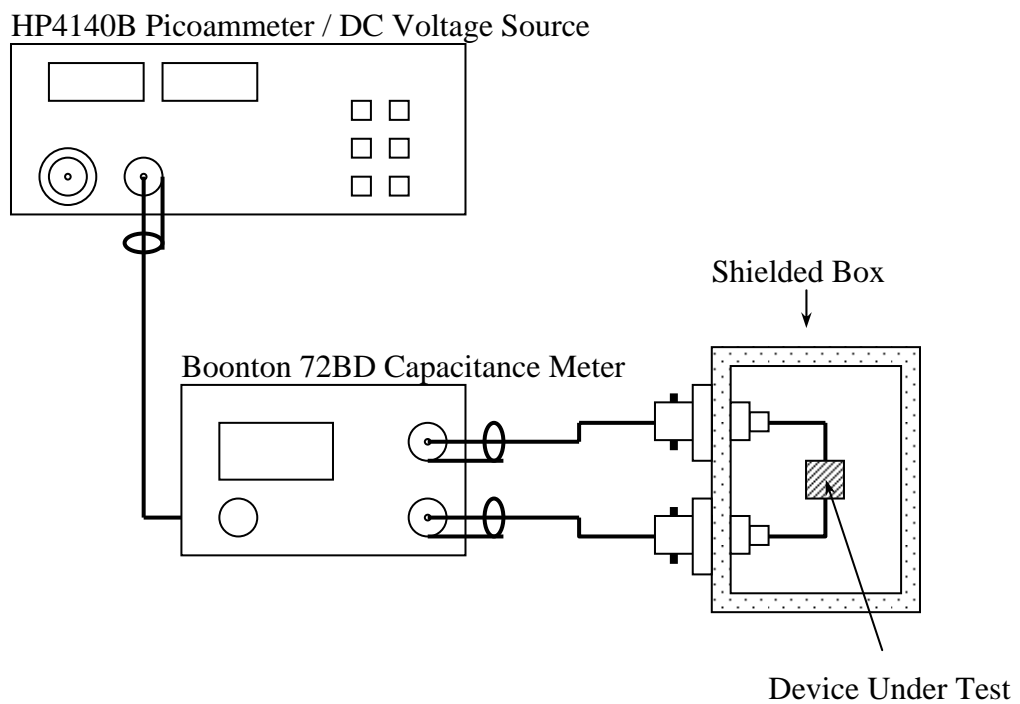


Figure 4.5: Schematic of the  $C$ - $V$  measurement setup.

The capacitance measurement using the Boonton 72BD capacitance meter was facilitated by applying an ac probing signal of magnitude 15 mV rms at a frequency of 1 MHz. The probing signal superimposed onto the DC bias voltage, which was supplied externally by the HP4140B constant voltage source. The minimum measurable capacitance of 72BD is  $1 \times 10^{-15}$  F. The device under test was placed inside the shielded box and connected to the capacitance meter via two coaxial cables. The coaxial cables were only ~6 inches in length to minimize the cable loading capacitance, which otherwise might have led to a deterioration in accuracy. Prior to the measurement, the stray capacitance contributed by the connecting cables and test fixtures were compensated by adjusting the zero control knob. The measurements were carried out at room temperature and in a dark environment to eliminate the influence of optically generated carriers in the device. The capacitances at different reverse biasing voltages were then measured and recorded for later analysis. Typical *C-V* data measured from a Ni/n-GaN Schottky contact photodiode are presented in Fig. 4.6.

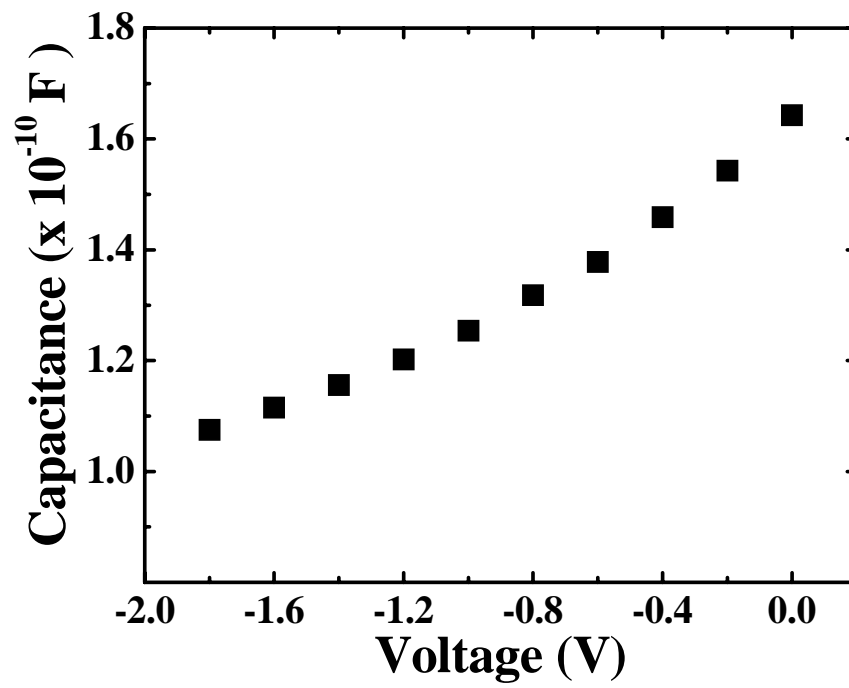


Figure 4.6: Typical *C-V* data measured from Ni/n-GaN Schottky photodiode.

#### 4.2.2 Free Electron Concentration

The ionized donor concentration,  $N_D$ , is obtained by fitting the  $C^{-2}$ - $V$  plot result with a linear function in the reverse biased region. Typical experimental data is shown in Fig.

4.7 and the slope  $\gamma$ , of this line is then shown to be  $\frac{2}{qN_D\epsilon_s}$ .

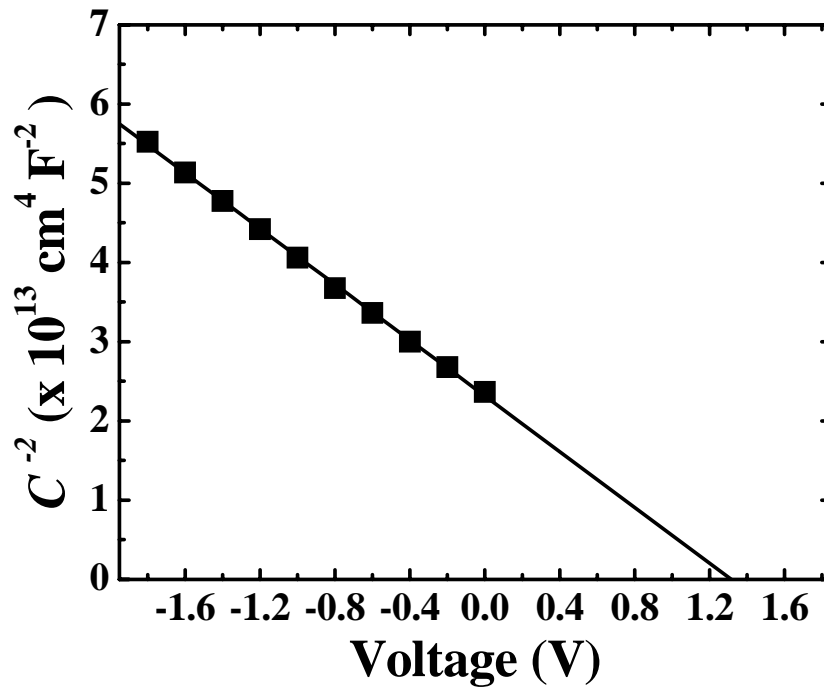


Figure 4.7: Experimental result of  $C^{-2}$  plotted against applied voltage  $V$ .

Thus, the ionized donor concentration is given by:

$$N_D = \frac{2}{q\epsilon_s A^2 \gamma} \quad (4.9)$$

### 4.2.3 Barrier Height

The built-in voltage is related to the Schottky barrier height by

$$V_{bi} = \frac{\phi_b}{q} - \frac{k_B T}{q} \ln\left(\frac{N_C}{N_D}\right).$$

Hence,

$$\phi_b = qV_{bi} + k_B T \ln\left(\frac{N_C}{N_D}\right), \quad (4.10)$$

where  $N_C$  is the effective density of states in the conduction band of the semiconductor.

The Schottky barrier height can then be evaluated as all the parameters are known in Eq. 4.10 except the built-in voltage  $V_{bi}$ . The built-in voltage is obtained from the extrapolated intercept of the fitted line in Fig. 4.7 with the  $V$ -axis, which gives the value of  $V_{bi} - k_B T/q$ .

### 4.3 Low-frequency Noise Measurements

Low-frequency noise measurement is an important figure of merit for semiconductor devices. It has also been shown that low-frequency noise can be used as an effective tool to probe and qualify junction behavior, as the low-frequency noise power spectral density is shown to be directly proportional to the trap density [93, 94]. One of the most important advantages of the use of noise measurements as a material and device characterization tool is that it is a nondestructive process compared to other characterization techniques such as TEM and SEM. In addition, noise generally exists in all electron devices and sophisticated sample preparation is not required, thus the characterization process can be conducted directly on the devices. This is particularly significant in the study of device degradation subjected to accelerated stressing.

#### 4.3.1 Noise Theory

Like any stochastic process, noise in semiconductors is characterized by its statistical function, which often reveals the underlying physics. Low-frequency noise in semiconductors can be categorized into four different types, namely, thermal noise, shot noise, generation-recombination (G-R) noise and  $1/f$  noise. In this research, the focus is on the study of low-frequency excess noise - G-R noise and  $1/f$  noise. Thermal noise and shot noise which dominate at high frequencies will not be discussed here.

### *G-R Noise Trapping Kinetics*

Generation-recombination (G-R) noise is caused by the random capture and emission of carriers (electrons or holes) by traps in semiconductors. The term traps in this thesis refers to those localized states located within bandgaps of semiconductors, capable of randomly capturing free carriers from the conduction and valence bands and subsequently releasing them, causing perturbation in both the carrier concentration and the current flow. Examples of traps are the shallow and deep levels of donors and acceptors, unintentional impurities in semiconductors, structural defects at crystal surfaces, threading dislocation, interfacial states in heterostructures etc.

As random processes, the traps are characterized by the capture probabilities or, equivalently, the average rates of trapping and de-trapping of carriers. Such probabilities can be described by the relaxation time constant,  $\tau_T$ , which is governed by the trap's parameters, such as their energy levels, capture cross sections and bearing signatures of the different trap species. Specifically, in n-type extrinsic semiconductors and for traps located in the upper half of the bandgap, the relaxation time of electron trapping is given by:

$$\tau_{T=} = \frac{1}{c_n [(N_T - n_{T0}) + n_o + n_s]} \quad (4.11)$$

where  $c_n$  is the electron capture coefficient,  $N_T$  is the trap density,  $n_{T_0}$  is the filled traps density at equilibrium,  $n_o$  is the electron concentration at equilibrium, and  $n_s$  is further defined as:

$$n_s = gn_o e^{\left(\frac{E_T - E_F}{k_B T}\right)}, \quad (4.12)$$

where  $g$  is the trap degeneracy factor and  $E_T$  is the trap energy level.

G-R noise, in general, is a multi-variable process, involving interaction of carriers among the conduction band, the valence band and various trap levels in materials. To simplify the calculation of the noise statistics, the multi-variable process is often approximated with one in which each trap level interacts independently with either the conduction or the valence band. Therefore, the fluctuation of carriers is described by separate independent trapping processes and the resulting noise spectrum is then the superposition of the noise spectra of the individual processes. The above approximation is valid when two of the following conditions are satisfied: the trap levels are at least a few  $k_B T$  away from the Fermi level and the density of each trap level is much smaller than that of the carrier concentration [95]. The noise power spectrum of G-R noise due to electron transitions between the conduction band and a single trap level is then given by [96-99]:

$$S_v(f) = S_o \frac{\tau_T}{1 + 4\pi^2 f^2 \tau_T^2} \quad (4.13)$$

where  $S_o = 4N_T\Omega(\Delta I_o)^2 R^2 f_T(1-f_T)$ ,  $\Omega$  is the active device volume,  $\Delta I_o$  is the current fluctuation due to the capture of a single carrier and  $R$  is the device resistance. At equilibrium, the probability function  $f_T$  is given by the Fermi-Dirac distribution function:

$$f_T = \frac{1}{1 + g \exp\left(\frac{E_T - E_F}{k_B T}\right)} \quad (4.14)$$

where  $E_T$  is the trap energy,  $E_F$  is Fermi level energy, and  $g$  is the trap degeneracy factor. Equation 4.13 has the form of a Lorentzian with a corner frequency  $f_c = 1/2\pi\tau_T$  and is schematically shown in Fig. 4.8. The spectral shape or the frequency dependence of  $S_V(f)$  is determined by the Lorentzian factor,  $\tau_T/(1+4\pi^2 f^2 \tau_T^2)$ , where the corner frequency divides the spectrum into two distinct regions: a plateau region for  $f < f_c$  and a roll off region for  $f > f_c$ . The roll off region of the spectrum is solely dependent upon the trapping kinetics while the low-frequency plateau region depends on, in addition to the trapping kinetics, the modulation mechanism whereby the filling and emptying of traps causes the device current to fluctuate.

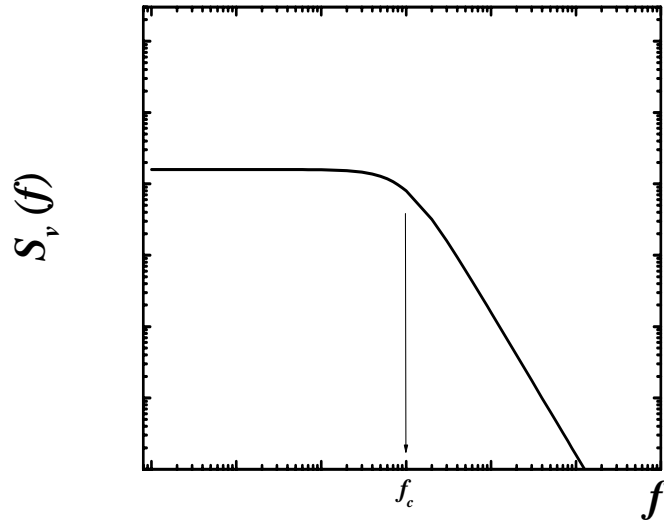


Figure 4.8: Schematic of a Lorentzian form power spectrum with a corner frequency  $f_c$ .

### *1/f Noise Theories*

Several models have been proposed to account for the origin of  $1/f$  noise in solid-state materials including the Hooge's empirical model, the quantum  $1/f$  noise model, McWorter's model, and the thermal activation model. The following sections give a brief summary of each.

### *Hooge's Model*

Based on the experimental studies of low-frequency noise in gold films and a number of semiconductor samples, Hooge *et al.* proposed a phenomenological formula for  $1/f$  noise [100, 101]:

$$\frac{S_V(f)}{V^2} = \frac{S_I(f)}{I^2} = \frac{\alpha_H}{Nf} \quad (4.15)$$

where  $N$  is the number of free carriers in a homogeneous sample,  $I$  is the dc current through the device and  $\alpha_H$ , is a dimensionless constant commonly known as the Hooge parameter, originally estimated to be  $2 \times 10^{-3}$ . As shown in Eq. 4.15, the dependence of  $S_V(f)$  and  $S_I(f)$  on  $N$  implies that the noise is caused by independent fluctuations associated with each free carrier, and thus gives a bulk effect. Despite the wide use of Hooge's equation and its limited success in explaining experimental data, critics of the model reject Hooge's formula and its interpretation on the following grounds:

- (i) while the Hooge equation is consistent with older noise data taken on a number of metals and semiconductors, samples with measured values of  $\alpha_H$  orders of magnitude different from  $2 \times 10^{-3}$  have also been reported in the literature, casting doubt on the possibility that a universal formula is applicable.

- (ii) studies on devices such as the MOSFET give extensive evidence for  $1/f$  noise originating from a surface effect as opposed to a bulk effect phenomenon.
- (iii) the spectral slope (in logarithmic scales) often is not exactly -1, as is required by Eq. 4.15, but ranges from -0.8 to -1.4. Furthermore, the value is found to vary with temperature and there is no explanation for this phenomenon based on Hooge's equation.

#### *Quantum 1/f Noise Model*

Another model attempt to give physical meaning to the Hooge equation is the formulation of the quantum  $1/f$  noise theories [102]. Handel proposed a quantum process, coherent state quantum  $1/f$  fluctuations, to obtain a close estimation of the Hooge parameter [103]. The calculated Hooge parameter based on the coherent state quantum  $1/f$  fluctuations mechanism is  $\alpha_H = 4.65 \times 10^{-3}$ , which is in good agreement with the high experimental range of  $\alpha_H$ . Like Hooge's model, Handel's theories are applicable only to cases where the noise exhibits a strictly  $1/f$  spectrum, i.e. with a slope of -1. However, there are large amount of data in the literature showing that the spectral slopes deviate from -1 and which is clearly indicate that in many samples the Hooge-type processes are not the dominant source of  $1/f$  noise [104-106]. In those cases, quantum  $1/f$  fluctuations may be present but are covered by noise of different origins.

### *1/f Noise Arising from the Superposition of Lorentzians*

As shown in Eq. 4.13, the power spectrum of a random process characterized by a single relaxation time is a Lorentzian,  $\tau_T / (1 + 4\pi^2 f^2 \tau_T^2)$ , which has a distinct corner frequency of  $f_c = 1/2\pi\tau_T$ . It is found that, the superposition of many Lorentzians with a distribution of  $\tau_T$  would result in a more gradual spectrum. Figure 4.9 shows the concept of the superposition of five Lorentzian form power spectra and the resulting  $1/f$  form spectrum.

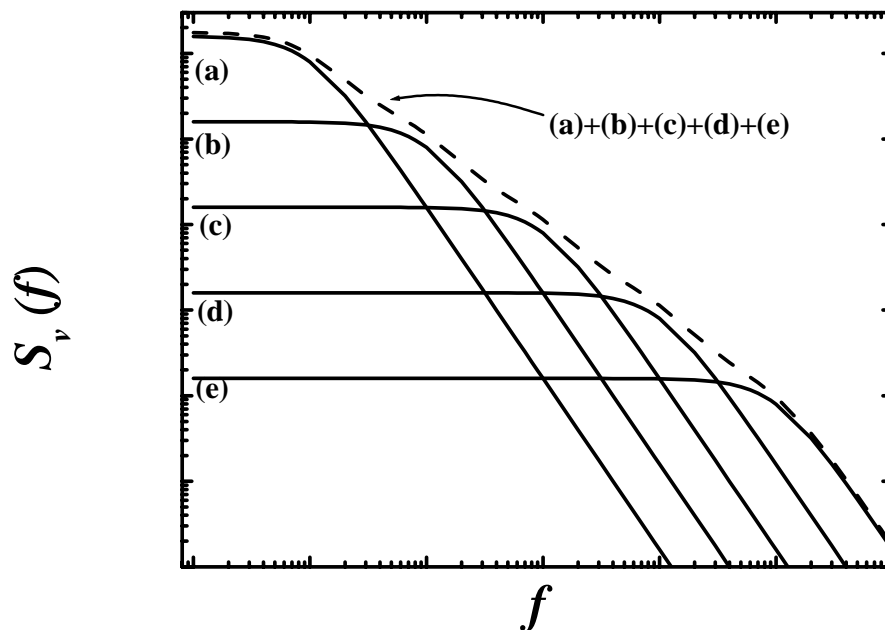


Figure 4.9: Superposition of five Lorentzian form power spectra (a), (b), (c), (d) and (e), with distributed corner frequency. The corresponding summation spectrum is shown as dash line.

Surdin [107] showed that if the relaxation time was thermally activated as given by:

$$\tau_T = \tau_o e^{E_\tau/k_B T} \quad (4.16)$$

where  $\tau_o$  is the inverse phonon frequency. Then a uniform distribution of  $E_\tau$ ,  $D(E_\tau) = D_o$ , would give an exact  $1/f$  spectrum within a lower and an upper frequency limit:

$$S_I(f) = \int dE_\tau D(E_\tau) \frac{L_o \tau_T(E_\tau)}{1 + 4\pi^2 f^2 \tau_T^2(E_\tau)}$$

$$\cong \frac{L_o D_o}{4f}, \text{ for } 1/2\pi\tau_2 \leq f \leq 1/2\pi\tau_1, \quad (4.17)$$

where  $L_o$  is the Lorentzian prefactor,  $\tau_1$  and  $\tau_2$  are the upper and the lower limits of  $\tau_T$  respectively. The idea of  $1/f$  noise arising from the superposition of Lorentzians forms the basis for McWhorter's model and the thermal activation model.

### *The McWhorter Model*

According to McWhorter [108],  $1/f$  noise in metal-oxide-semiconductor (MOS) systems originates from carrier trapping by localized states in the oxide giving rise to local fluctuations in the carrier number. The oxide traps are kinetically different from semiconductor bulk traps in that the oxide traps are spatially separated from the carriers. Thus, in this model, trapping and detrapping of carriers are assumed to take place via

tunneling. The power spectrum for fluctuations in the trap occupancy in an elemental volume  $\Delta x \Delta y \Delta z$  is [109]:

$$S_{\Delta N}(f) = 4N_{TT}(E, z)f_T(1-f_T)\Delta x \Delta y \Delta z \Delta E \frac{\tau_{TT}(E_\tau)}{1+4\pi^2 f^2 \tau_{TT}^2(E_\tau)} \quad (4.18)$$

where  $N_{TT}(E, z)$  is the density of traps, the Fermi factor  $f_T(1-f_T)$  in Eq. 4.18, as a function of the trap energy  $E_T$ , peaks sharply at  $E_T = E_F$  and  $\tau_{TT}$  is the tunneling time constant. Therefore, only traps with energies within a few  $k_B T$  from the Fermi level contribute to number fluctuations.

#### *Thermal Activation Model*

In the thermal activation model, the  $1/f$  noise is considered resulting from the superposition of Lorentzian spectra arising from thermally activated processes, where the required distribution of  $\tau_\tau$  resulted from a distribution of  $E_\tau$  [110-111]. Noting that a uniform distribution of  $D(E_\tau)$  was not necessary for  $1/f^\gamma$  noise. Dutta and Horn found that a smooth  $D(E_\tau)$  on the scale of  $k_B T$  would give rise to the spectral density varying as  $1/f^\gamma$ , where  $\gamma$  is close to unity [111].

Since both the spectral slope  $-\gamma$  and the noise magnitude depend on the distribution function,  $D(E_\tau)$ , a relationship can be derived connecting the two measurable quantities. For  $\tau_{Th} = \tau_o \exp(E_\tau/k_B T)$ , the Lorentzian factor  $\tau_{Th}/(1+4\pi^2 f^2 \tau_{Th}^2(E_\tau))$  as a function of  $E_\tau$  peaks sharply at

$$E_p = -k_B T \ln(2\pi f \tau_o) \quad (4.19)$$

It is noted that one can effectively probe traps with different activation energies by measuring the spectral density at different temperatures and frequencies. At a given temperature and frequency, and for a smoothly varying  $D(E_\tau)$  around  $E_p$ , Eq. 4.17 can be expressed as

$$\begin{aligned} S_I(f) &\approx L_o D(E_p) \int dE \frac{\tau_T(E_\tau)}{1 + 4\pi^2 f^2 \tau_T^2(E_\tau)}, \\ &= L_o D(E_p) \frac{k_B T}{4f} \end{aligned} \quad (4.20)$$

From Eq. 4.20, one can express the trap distribution in terms of  $S_I(f)$ :

$$D(E_p) = \frac{4f S_I(f)}{k_B T L_o} \quad (4.21)$$

Equation 4.20 shows that the shape of  $D(E)$  directly affects the magnitude and the spectral form of fluctuations. Varying both  $f$  and  $T$  while keeping  $E_p$  unchanged, Dutta *et al.* derived the temperature dependence of  $\gamma$  as:

$$\gamma \equiv -\frac{\partial \ln S_I}{\partial \ln f} = 1 - \frac{1}{\ln(2\pi f \tau_o)} \left( \frac{\partial \ln S_I}{\partial \ln T} - 1 \right) \quad (4.22)$$

### 4.3.2 Experimental Setup

The experimental setup for low-frequency noise measurement is shown in Fig. 4.10. First, the device under test (DUT) was placed inside a continuous flow cryostat, which was capable of being cooled down to 77K using liquid nitrogen as a cryogen. The temperature of the device was monitored and controlled by a Lakeshore 91C temperature controller, for which the silicon diode temperature sensors were current biased by a battery to eliminate the possible 50Hz ripples coupled from the line supply of the Lakeshore 91C temperature controller. An all-passive RLC filter was also used to filter the Lakeshore 91C current supply to the heater. Device biasing during the noise measurement was provided by the biasing circuit, composed of a battery supply, ten-turn potentiometer and series resistors. A high voltage battery (~100V) and a series resistor of value typically at least 30 times or more than the a.c. resistance of the device were used to achieve a near ideal current source biasing condition. The signal across the sample was then amplified by a battery powered PAR 113 low-noise preamplifier and fed to an HP3561A dynamic signal analyzer. In order to eliminate extraneous noise, the sample, the biasing circuit, and the amplifier were enclosed in a shielded room. The signal fed into the dynamic signal analyzer was sampled and a real-time fast Fourier transform (FFT) was performed to obtain the power spectral density of the voltage fluctuation. The spectra were averaged typically 1000 times for accuracy and stored temporarily in the analyzer non-volatile memory. A Labview program resident in an

IBM compatible personal computer (PC) was then used to acquire and store the measured data through the GPIB cable and IEEE interface to the PC for data analysis.

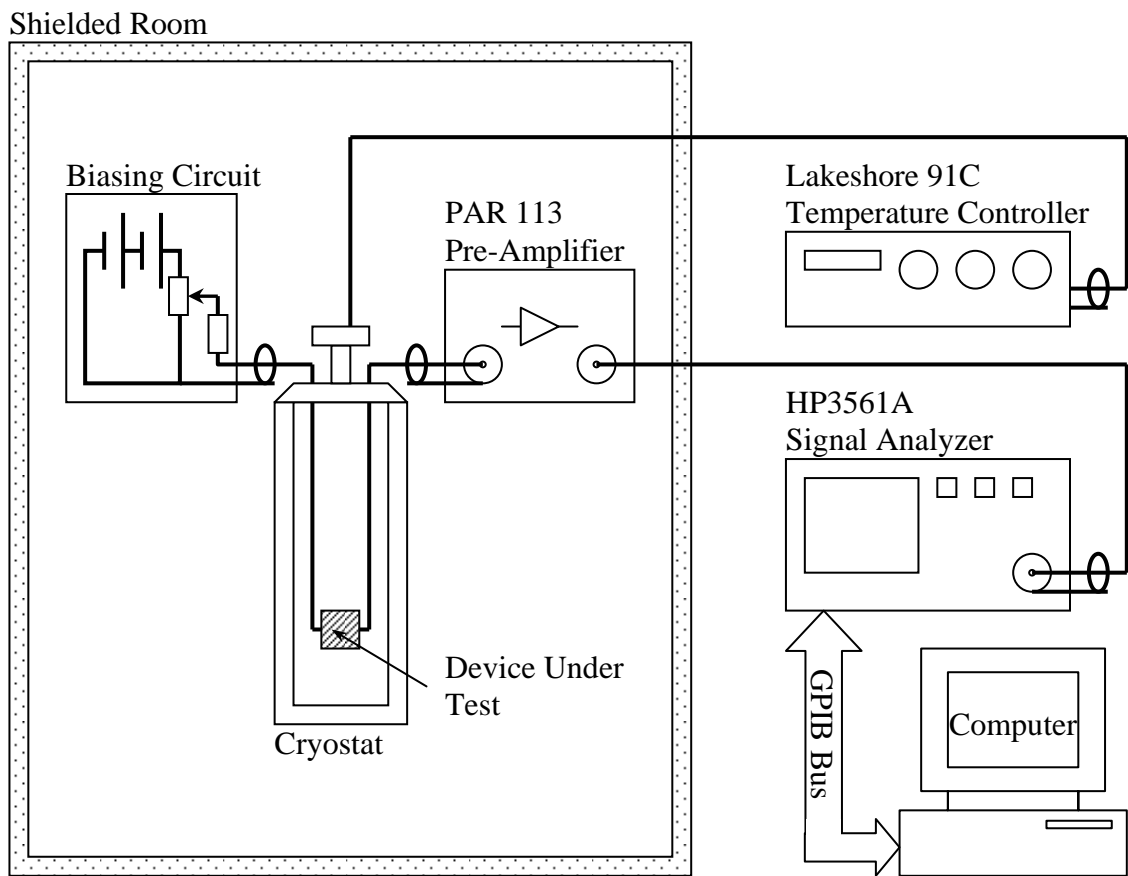


Figure 4.10: Schematic of the low-frequency noise measurement setup.

## 4.4 Spectral Response Measurement

### 4.4.1 Responsivity

There are a number of figures of merit used to indicate photodetector performance. The most fundamental among these is the responsivity,  $\mathfrak{R}$ , which is defined as the ratio of the detector output over the given input:

$$\mathfrak{R} = \frac{\text{signal output}}{\text{input optical power}}. \quad (4.23)$$

The signal output is measured either as a photo-generated voltage or current and the conventional units of responsivity are V/W or A/W. In this thesis, the current responsivity is used, so that:

$$\mathfrak{R}(\lambda) = \frac{I_{photo}}{P_{\lambda}}. \quad (4.24)$$

where  $I_{photo}$  is the photocurrent and  $P_{\lambda}$  is the illumination power at a wavelength  $\lambda$ .

Since only photons with energy larger than the bandgap  $E_G$  are absorbed, there is a cutoff wavelength,  $\lambda_c$ , below which the responsivity will increase by several orders of magnitude. Furthermore, the number of photons per watt decreases with decreasing wavelength, so that  $\mathfrak{R}(\lambda)$  also decreases with wavelength for the same quantum efficiency of the device over the measured spectral range.

The quantum efficiency,  $\eta$ , of an optoelectronic device is defined as a fraction of the electrons collected over the number of incident photons as shown in the equation below [112]:

$$\eta = \frac{r_e}{r_p} \times 100\% \quad (4.25)$$

where  $r_e$  is the rate of electron collection and  $r_p$  is the photon arrival rate. The photon energy is given by the product of its frequency,  $f$ , and the Planck's constant,  $h$ , thus the rate of photon arrival can be expressed as a function of the corresponding optical power:

$$r_p = \frac{P_\lambda}{hf} = \frac{P_\lambda \lambda}{hc} \quad (4.26)$$

where  $c$  is the speed of light. The rate of electron collection can be expressed as:

$$r_e = \frac{I_{photo}}{q} \quad (4.27)$$

With the aid of Eqs. 4.24 through 4.27, one can express the responsivity in terms of quantum efficiency:

$$\begin{aligned} \mathfrak{R}(\lambda) &= \frac{I_{photo}}{P_\lambda} \\ &= \frac{qr_e}{hfr_p} \end{aligned}$$

$$= \frac{q}{hf} \times \eta \text{ or } = \frac{q\lambda}{hc} \times \eta. \quad (4.28)$$

#### 4.4.2 Experimental Setup

The schematic diagram of the experimental set-up for the responsivity measurements is shown in Fig. 4.11. A 150W Xenon (Xe) lamp was used as the light source. The light from the Xe lamp was first passed through an Oriel 77250 monochromator to select a specific wavelength for measurement. A ruled grating with 1200 line/mm and blaze wavelength at 350 nm capable of selecting wavelength range between 200 – 1000 nm, was installed inside the monochromator. The slit size in front of the monochromator was selected to obtain a line resolution better than 1 nm. These monochromatic beams were then converged by a UV enhanced silica glass lens and directed to the device under test via a pinhole. Prior to the measurement, the spectral power ultimately passing through the lens and pinhole was measured by a Newport Model 840 handheld optical power meter with a calibrated Model 818 UV enhanced silicon detector. In order to measure a device's response, the devices were wire bonded on a dual in-line (DIL) 24-pin ceramic package. The DIL packaged devices were then inserted into a zero insertion force (ZIF) test header socket, which was mounted on a triple axis manipulator positioned on an optical bench. The micro-manipulator allowed precise optical alignment of the device under test. The photo-generated current from the device was then fed to a Keithley 617 electrometer which was capable of accurately measuring the current down to  $10^{-16}$  A. The spectral response was then measured over 250 nm to 500

nm and the corresponding photocurrents were recorded. Following Eq. 4.24, the spectral responsivities for the devices were obtained. The quantitative value of the responsivity at 325 nm was obtained using a He-Cd laser as the light source and the measured spectral response was then normalized to this value in order to eliminate the non-linearity effect from the Xe light source.

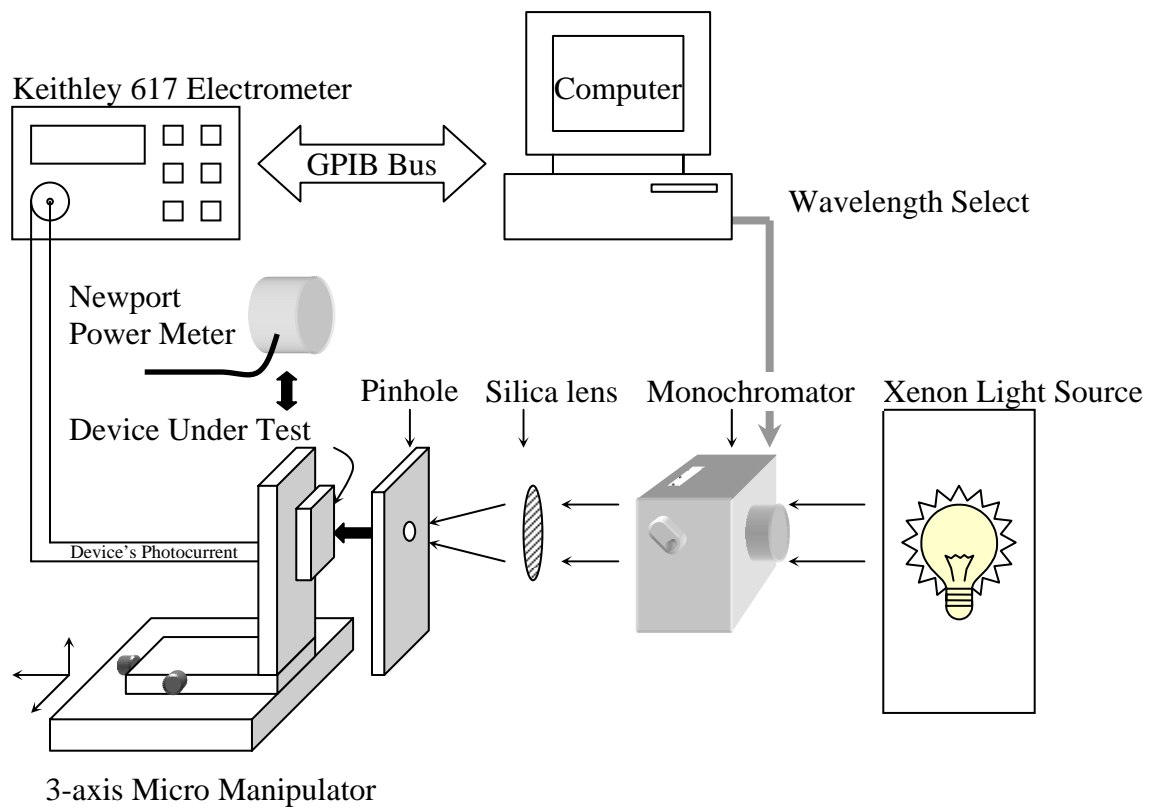


Figure 4.11: Schematic of the spectral response measurement setup.

## **Chapter 5**

### **Experimental Results and Discussion**

#### **5.1 Experiment I: Optical Stressing of Ni/n-GaN UV Photodiodes**

Two types of GaN visible blind Schottky diode photodetectors were investigated in this work. Type I devices were fabricated on n-doped GaN epitaxial layers grown with the use of a novel double buffer layer structure that consisted of a conventional AlN high temperature buffer layer and a GaN intermediate-temperature buffer layer (ITBL). Detailed studies on the optoelectronic properties of GaN epitaxial layers grown with the ITBL structure has been conducted systematically by Fong *et al.* [30-32, 51, 79-81]. It was shown that the electron mobility, PL intensity at 365 nm, and low-frequency noise properties were optimized at an ITBL thickness of 800 nm. In this study of GaN-based UV detectors, an ITBL thickness of 800 nm has been chosen for the fabrication of type I devices. Type II devices were fabricated on a GaN epi-layer grown with the use of a

single conventional AlN high temperature buffer layer. This will serve as a control to elucidate the effects of the double buffer layer structure on the reliability of the devices.

The active region of both types of detector consists of a semi-transparent Schottky junction formed by the deposition of a thin Ni layer on top of a lightly Si doped n-GaN epi-layer. The GaN epi-layers were grown using an rf-plasma assisted Molecular Beam Epitaxy (MBE) system on the c-plane sapphire substrates ( $\text{Al}_2\text{O}_3$ ) with the thickness of  $\sim 1 \mu\text{m}$ . Typical carrier concentration of around  $5 \times 10^{17} \text{ cm}^{-3}$  were obtained from Hall measurements. Detailed fabrication processes of the devices used in this study is given in Chapter 3, Section 3.5.4.

### 5.1.1 Accelerated Optical Stressing

During normal operation of the devices, the photodetectors are subject to exposure to high levels of UV radiation. It is therefore important to investigate the reliability of the devices when exposed to high intensity UV illumination. The reliability of the fabricated photodiodes was studied by accelerated optical stressing. The accelerated optical stressing setup is described as follow. A 300W Xenon lamp was used as the light source to generate high-power UV radiation. The light output was focused and the radiation intensity increased by a UV-enhanced fused silica lens with a 1-inch focal length. The intensity of the UV radiation irradiated onto the device was estimated to be around  $4 \text{ Wcm}^{-2}$ , measured by a calibrated UV sensor. This UV power density is about a thousand times that of the solar UV power under clear sky conditions, according to the

standard solar spectral irradiance specified by the International Commission on Illumination (CIE) [113].

In order to collect the highest light output, the wire-bonded devices inside the ceramic packages were inserted into a zero insertion force (ZIF) test header socket, which was mounted on a triple axis micro manipulator to align the devices under stress to the focused point of the system. During the optical stressing process, the devices were zero biased and the photo-current was monitored by a Keithley 617 electrometer.

The optoelectronic properties, including the current-voltage ( $I$ - $V$ ) characteristics, capacitance-voltage ( $C$ - $V$ ) properties, photo-responsivity and the low-frequency excess noise of the devices were investigated systematically as a function of the stress time,  $t_S$ . To avoid possible short-term transient irradiation effects, the samples were kept at room temperature, in the dark, for at least an hour after stressing and prior to performing any measurements. Figure 5.1 illustrates the setup for the accelerated optical stressing experiment.

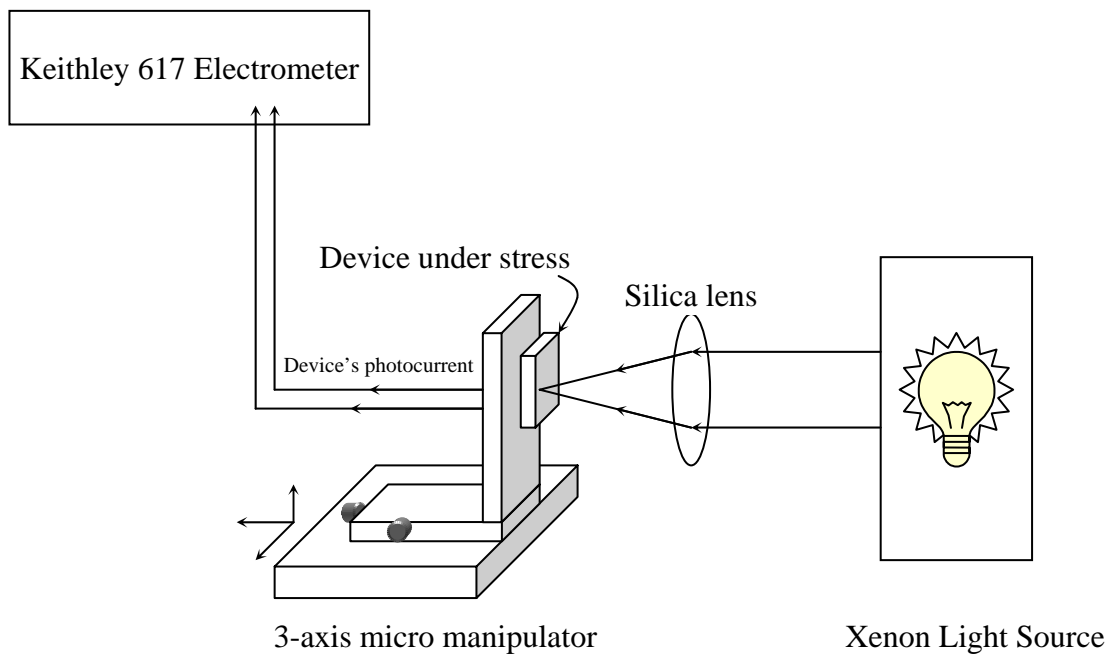


Figure 5.1: Schematic of the accelerated optical stressing experiment.

Electrical characterizations of the devices were carried out using  $I$ - $V$ ,  $C$ - $V$  and low-frequency noise measurements. These experiments were performed systematically as a function of the stress time. The experimental data shown that significant changes in the  $I$ - $V$ ,  $C$ - $V$  and low-frequency noise power spectral density,  $S_V(f)$ , of the devices could be seen as the stress time increases. In particular, catastrophic breakdown in the electronic properties among type II devices was observed, and is detailed in the sub-sections below. Optical characterization of the devices was carried out by measuring the spectral response of the devices as a function of  $t_S$ .

### 5.1.2 Experimental Results on $I$ - $V$ Measurements

Figure 5.2 shows typical examples of the  $I$ - $V$  characteristics of the wire bonded Ni/n-GaN Schottky photodiodes prior to optical stressing. Both types of devices demonstrated good rectifying Schottky  $I$ - $V$  characteristics with a room temperature reverse leakage current of  $\sim 6.8 \times 10^{-9}$  A and  $\sim 2.8 \times 10^{-9}$  A for type I and type II devices respectively at  $V = -0.2$  V. Typical experimental data on the  $I$ - $V$  characteristics of the devices in semi-logarithmic plot of  $I / (1 - e^{-qV/k_B T})$  against  $V$  are also shown in Fig. 5.3.

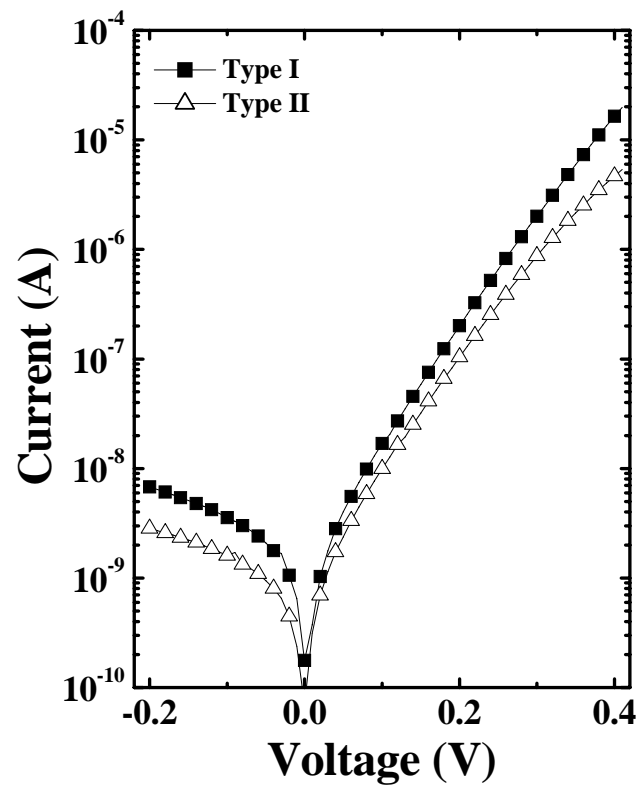
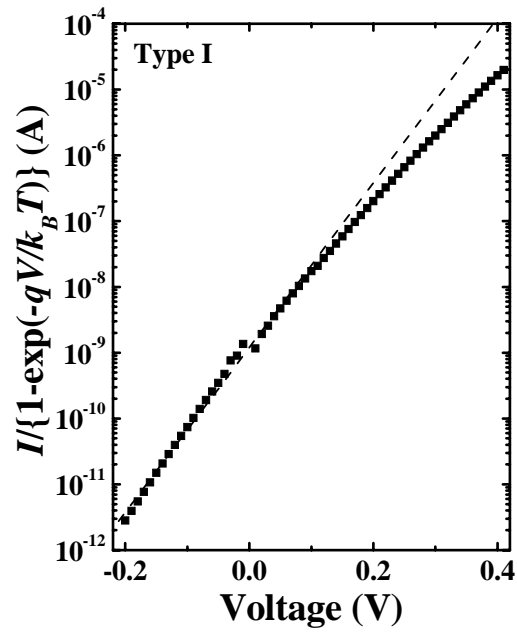
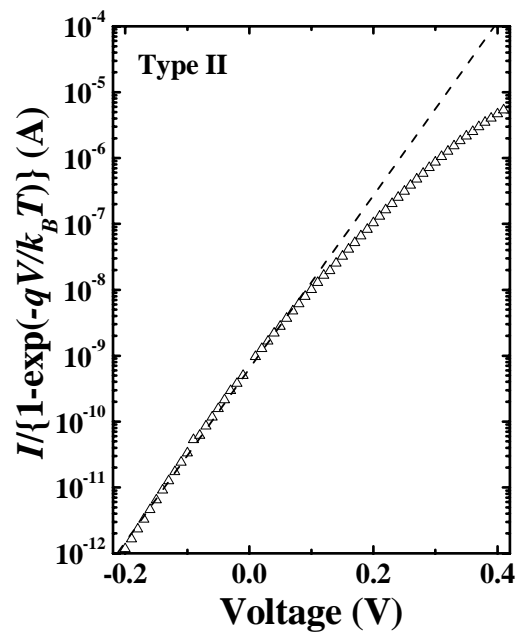


Figure 5.2: Typical  $I$ - $V$  characteristic measured from type I and type II.



(a)



(b)

Figure 5.3: Typical semi-logarithmic plot of  $I / (1 - e^{-qV/k_B T})$  against  $V$  measured from (a) type I and (b) type II devices.

Figures 5.2 and 5.3 show that both types of devices exhibit very similar room temperature  $I$ - $V$  characteristics, indicating similar quality for both types of devices prior to their exposure to high intensity UV radiation. Any observed differences between the devices can be easily accounted for by run-to-run fluctuations.

In order to extract the ideality factor and analyze current transport mechanisms of the devices, the  $I$ - $V$  measurement result is plotted in a semi-logarithm graph of  $I / (1 - e^{-qV/k_B T})$  against  $V$  and this is shown in Fig. 5.3. The reverse bias current exhibits a linear relationship with the biasing voltage. The deviation from linearity at high forward bias is due to the effect of series resistance. For the data shown in Fig. 5.3, the ideality factors,  $n$ , obtained from the slopes of the  $I$ - $V$  plots are found to be 1.35 and 1.29 for types I and II devices respectively. These values are larger than unity as expected by the thermionic emission theory, which indicates that electron transport is not dictated only by thermionic emission. In practice diodes will be less than ideal leading to large values of  $n$ . Possible physical mechanisms that may account for  $n$  larger than unity are the presence of an interfacial layer, the recombination in the depletion region and the trap-assisted tunneling, which will be further explored in the following section. Care must be taken, if one attempts to determine the barrier heights from the  $I$ - $V$  characteristics as it is reliable only if the current is mainly govern by the thermionic emission theory. Wide range of values had been reported for the barrier height of the Ni/n-GaN junctions based on  $I$ - $V$  analyses [28, 53, 114, 115]. The cause of this spread is not clear, however, it is likely due the difference in the fabrication processes, films grown by different techniques, surface terminations, and defect densities etc. There is generally less scatter

in the experimental barrier height obtained from the  $C-V$  data in the literature. The Schottky barrier heights of the photodiodes in this study is determined by the  $C-V$  measurement results as presented in the following section.

Although the pre-stressed  $I-V$  characteristics measurement results from both types of devices indicate similar electrical properties before optical stressing, they show a rather different picture when subjected to high intensity UV radiation. It is found that type II devices, which were fabricated without the ITBL structure, exhibit shorter lifetimes compared to the type I devices, as shown in Table 5.1. In this study, device failure is defined as the condition when the junctions were no longer rectifying and exhibiting nonlinear, symmetric current flow for both forward and reverse biases.

		<b>Time to failure (hours)</b>
<b>Type I devices</b>	Device 1	No observed failure (>90)
	Device 2	No observed failure (>90)
<b>Type II devices</b>	Device 1	45
	Device 2	27
	Device 3	57

Table 5.1: Time to failure for the optically stressed devices.

Experimental  $I$ - $V$  results from both type I and type II devices upon optical stressing are shown in Figs 5.4 and 5.5. Figure 5.4 shows the  $I$ - $V$  characteristic measured after various stress times for type I and II devices. Figure 5.5 present the reverse current,  $I_r$ , where  $V$  is set at  $-0.2\text{V}$ , against the stress time,  $t_S$ , for all devices being studied. The reverse bias of  $-0.2\text{V}$  is used as it won't alter the devices characteristic according to our experiences. From the figures it can be observed that both types of device indicate an increase in the reverse current as a function of  $t_S$ . For type I devices, the increase in  $I_r$  remains gradual up to  $t_S = 90$  hours. However, type II devices typically indicate similar gradual increase in  $I_r$  initially, but after a certain period of time catastrophic increases in  $I_r$  are observed. For the particular type II device shown in Fig. 5.4, such catastrophic failure took place at  $t_S = 45$  hours. It should be noted that different devices may fail at different values of  $t_S$ . The average lifetime for type II devices is found to be  $\sim 43$  hours with a large variation from device to device, while type I devices exhibit lifetimes longer than 90 hours.

As shown in Fig. 5.5, one observes drastic increases in the leakage current in type II devices immediately before the failure of the devices. This significant increase in the leakage current can be related to the increase in the defect states at the Schottky barrier due to the applied energetic UV radiation. It results in the increase in the trap-assisted tunneling current through the junctions. When the devices fail, it is observed that their junction properties becomes unstable and the reverse current becomes fluctuate at longer stressing times as shown in the results. The interfacial properties of these

samples were further analyzed by  $C$ - $V$  and low-frequency noise measurements in the following sections.

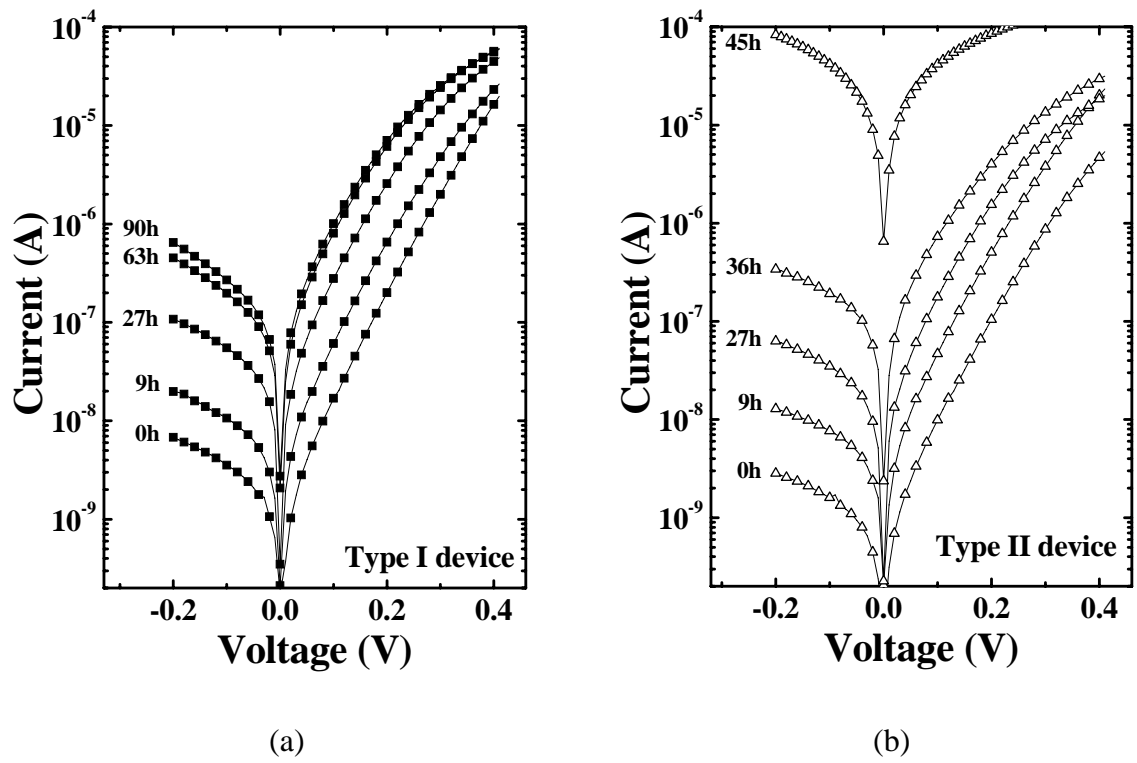
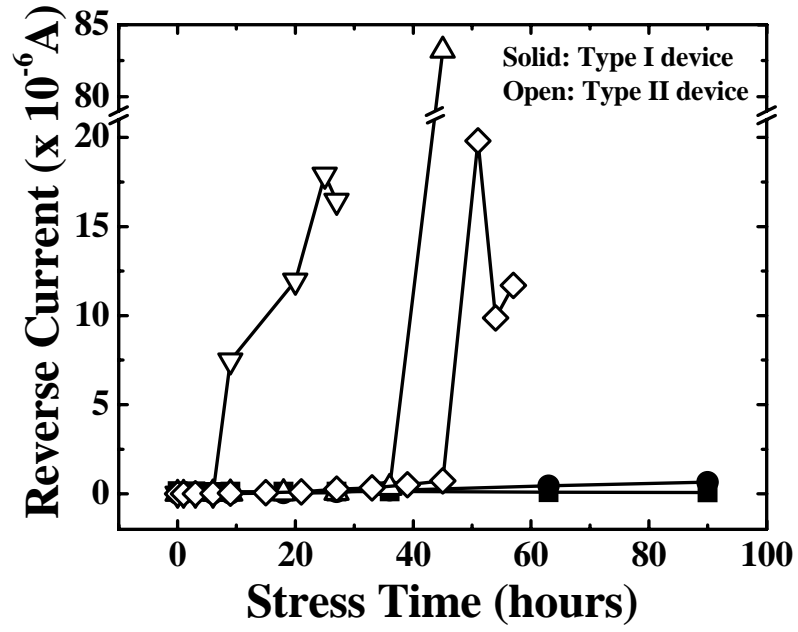
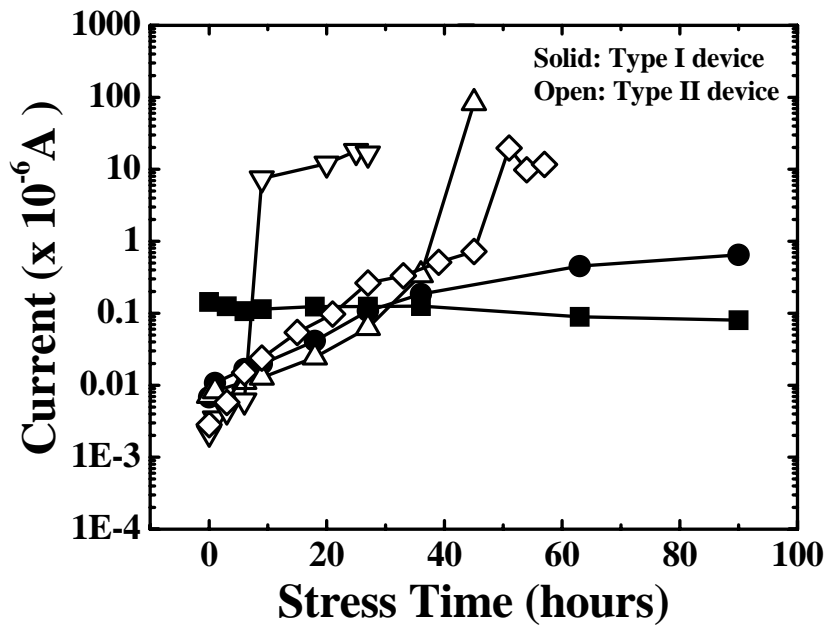


Figure 5.4: Experimental semi-logarithmic  $I$ - $V$  characteristics measured at different  $t_s$  for (a) type I and (b) type II devices.



(a)



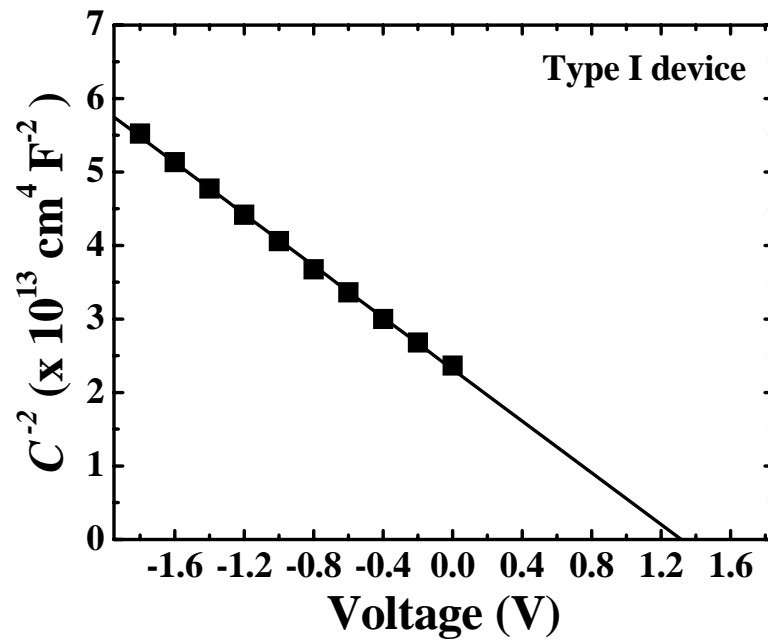
(b)

Figure 5.5: Reverse leakage current at  $-0.2 \text{ V}$  as a function of  $t_s$  for type I (solid symbols) and type II (open symbols) devices. (a) Linear plot; (b) Semi-logarithmic plot.

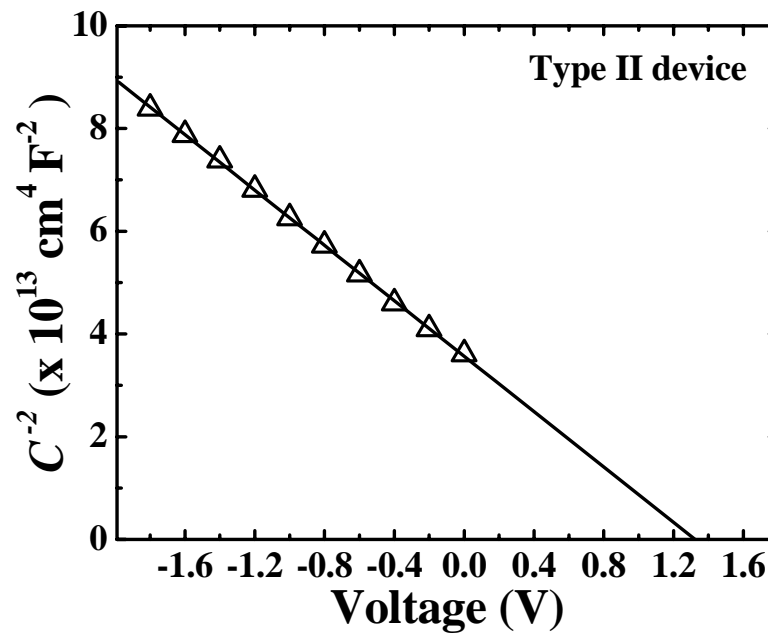
### 5.1.3 Experimental Results on $C$ - $V$ Measurements

Detailed characterizations of the junction capacitance was undertaken to investigate the interface properties of the devices. As discussed in Chapter 4, plots of  $C^{-2}$  against  $V$  yield important information on the barrier height of the Schottky junction. Figure 5.6 below shows the typical  $C^{-2}$ - $V$  plots for both types of diodes. The data exhibit a linear relationship between  $C^{-2}$  and the applied reverse bias voltage across the device. The results indicate the formation of abrupt Schottky junctions with a uniformly distributed carrier concentration at the depletion region. The voltage intercepts obtained from the plots yield the built-in potentials ( $V_{bi}$ ) of 1.34 V and 1.35V for types I and II devices respectively. The Schottky barrier heights can then be determined from the measured  $V_{bi}$  and Eq. 4.10, and are found to be equal to 1.37 eV and 1.39 eV for type I and type II devices, respectively.

Upon exposing the devices to high intensity UV radiation, significant changes occur in the  $C$ - $V$  relationship as shown in Fig. 5.7. The experimental data clearly show the capacitances measured from both type I and II devices decrease monotonically with  $t_S$ . It is important to note that a steady decrease in the capacitance is observed for type I devices as a function of the stress time. However, for the particular type II device shown in Fig. 5.7 below, a catastrophic decrease in the capacitance is observed for stress times of 36 hours or above. In general, such a catastrophic decrease in the junction capacitance is observed among type II devices only.

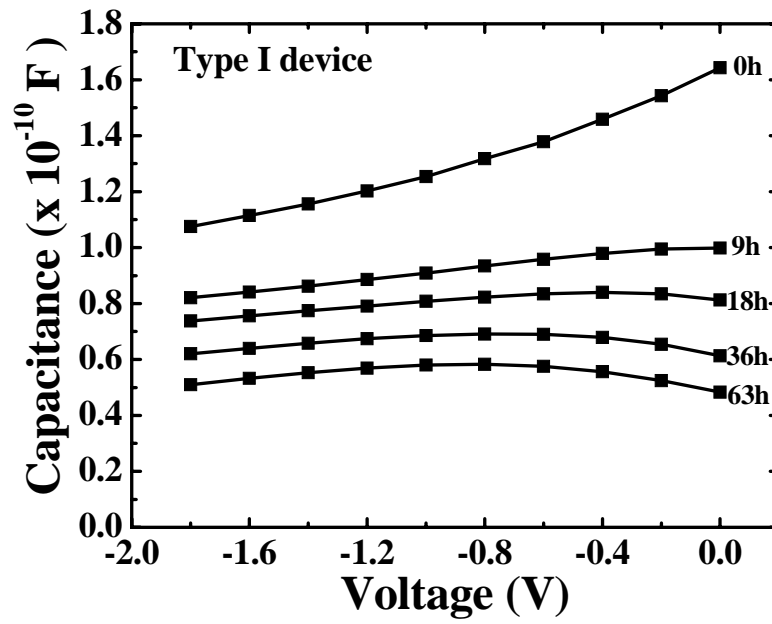


(a)

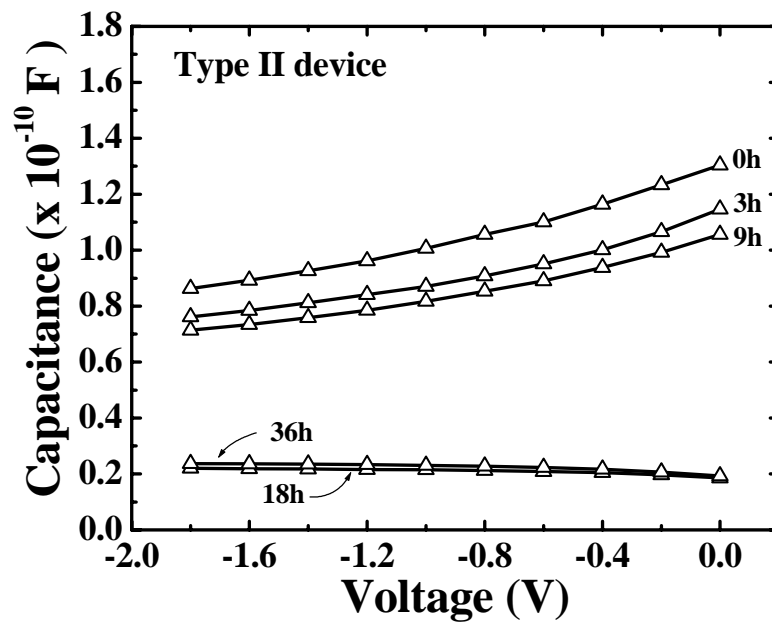


(b)

Figure 5.6:  $C^{-2}$  versus  $V$  characteristics for a typical (a) type I device and (b) type II devices before optical stress.



(a)



(b)

Figure 5.7: Experimental  $C$ - $V$  characteristics measured at different  $t_s$  for (a) type I and (b) type II devices.

Similar decrease in the capacitance due to the irradiation of the Schottky junctions with energetic radiation/particles had been investigated by Jayavel *et al.* [116]. It has been shown that the decrease in the capacitance arises from the generation of localized states at the junction, leading to the increase in trap-assisted tunneling through the Schottky junction. This establishes an alternate parallel conductive path through the junction and, thereby, shorts out of the junction capacitor. The experimental variations in the capacitance, as a function of the stress time, corroborates the observed changes in the reverse leakage current, as reported in the previous section. The observed catastrophic reduction in the capacitance for type II devices. This stipulates the corresponding catastrophic increase in the localized states at the Schottky junctions, which is in agreement with the observations in the degradations of the reverse currents among the type II devices.

#### 5.1.4 Experimental Results on Spectral Response Measurements

Typical spectrally resolved current responsivity of GaN Schottky photodiodes fabricated with an Ni-Schottky contact for both types of devices before optical stress is shown in Fig. 5.8. We found that prior to UV radiation stressing, both type I and II devices have similar responsivities, exhibiting a sharp and narrow cutoff at around 364 nm, the direct bandgap energy of the GaN film. Above the band edge, the sensitivity remains constant within an order of magnitude. Both type I and II photodetectors had nearly equal maximum current responsivities of 0.063 A/W and 0.065 A/W respectively at 350 nm, which corresponds to ~23% quantum efficiency ( $\eta$ ). The responsivities are

found to decrease sharply after the cutoff wavelength and typical responsivities at 400 nm are two orders of magnitude below the maximum value at 350 nm, and are believed to be determined by defect related absorption in the sub-bandgap region.

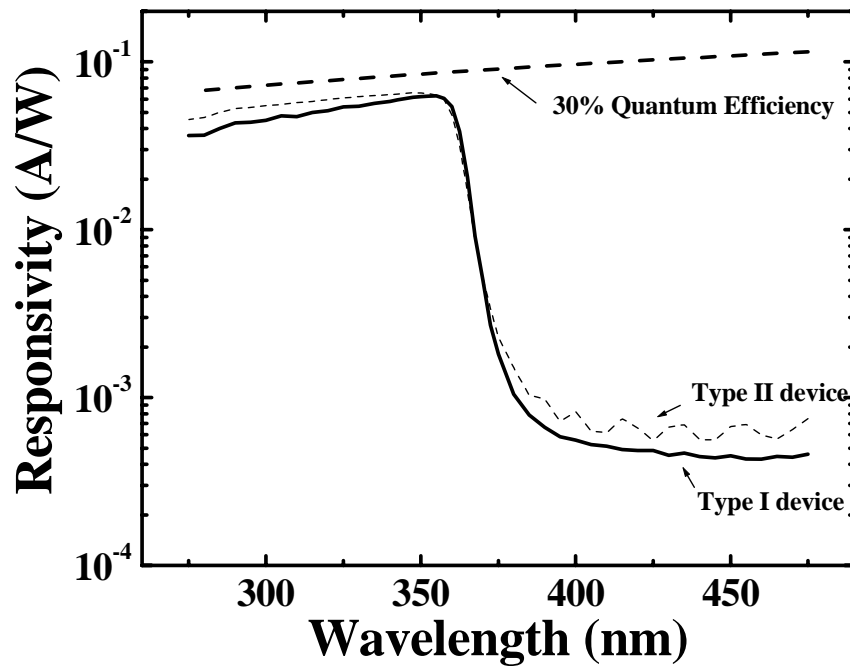
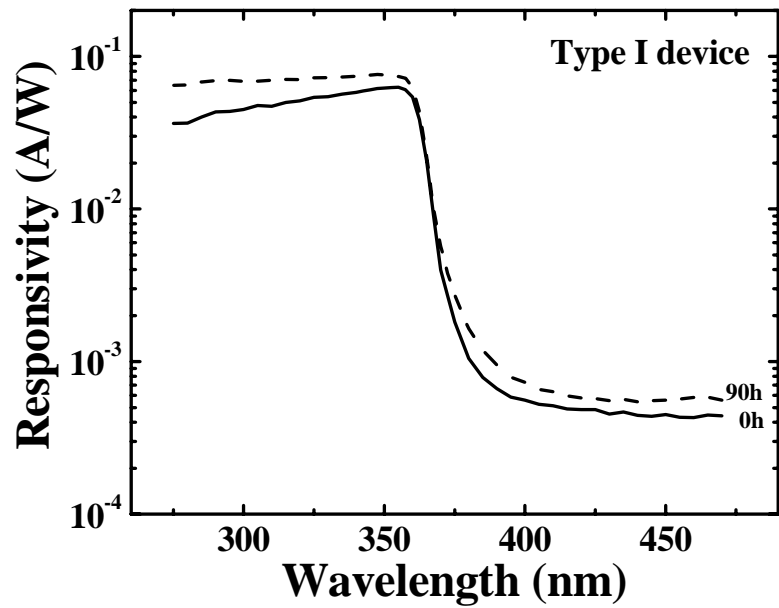
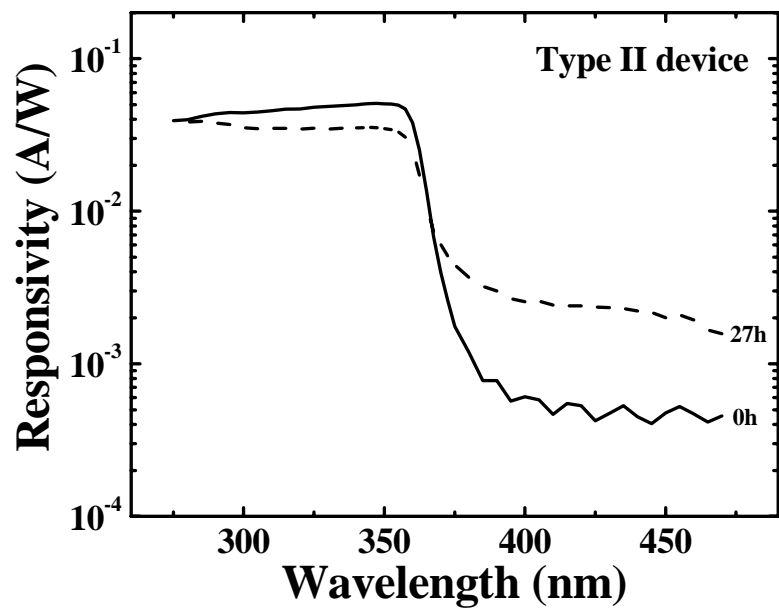


Figure 5.8: Typical spectrally resolved current responsivities for type I (solid line) and type II (dashed line) devices before optical stress. Dashed line shows the theoretical calculated responsivity of 30% quantum efficiency for eye guidance.



(a)



(b)

Figure 5.9: Experimental spectral responsivities for (a) type I and (b) type II device both before optical stress, after 90 hours and 27 hours of optical stress respectively.

The irradiation of the devices by high intensity UV radiation is found to have strong effects on the responsivities of the devices. Significant differences are observed in the behaviour between type I and type II devices upon exposure to high intensity UV radiation. Figure 5.9 clearly indicates that changes in the responsivities of the type I devices are relatively insignificant when subjected to the UV radiation stress compared to type II devices. In fact, little to no degradation is typically observed in type I devices after being exposed to the UV radiation for a duration of 90 hours. For the particular device shown in Fig. 5.9, a slight increase in the responsivity is actually observed after a stress time of 90 hours. It is believed that this is due to the thermal annealing effect from the heating of the device during the UV irradiation process. On the other hand, type II devices typically exhibit some kind of catastrophic breakdown for a stress time  $< 90$  hours. The experimental data shown in Fig. 5.9 indicate about 50% degradation in the responsivity for this particular type II device under test after a stress time of 27 hours. Several devices have been tested and the results are consistent with the experimental data presented above, in which type I devices invariably demonstrate much better radiation hardness compared to type II devices, as shown in Figs. 5.10 to 5.12. Figures 5.10 and 5.11 present the devices' responsivity at photon energy slightly above (at 350 nm) and below (at 400 nm) the bandgap energy of GaN as a function of  $t_S$ . The UV/visible rejection ratio, which defined as the responsivity at 350 nm divide by the value at 400 nm, is also plotted as a function of  $t_S$  and shown in Fig. 5.12.

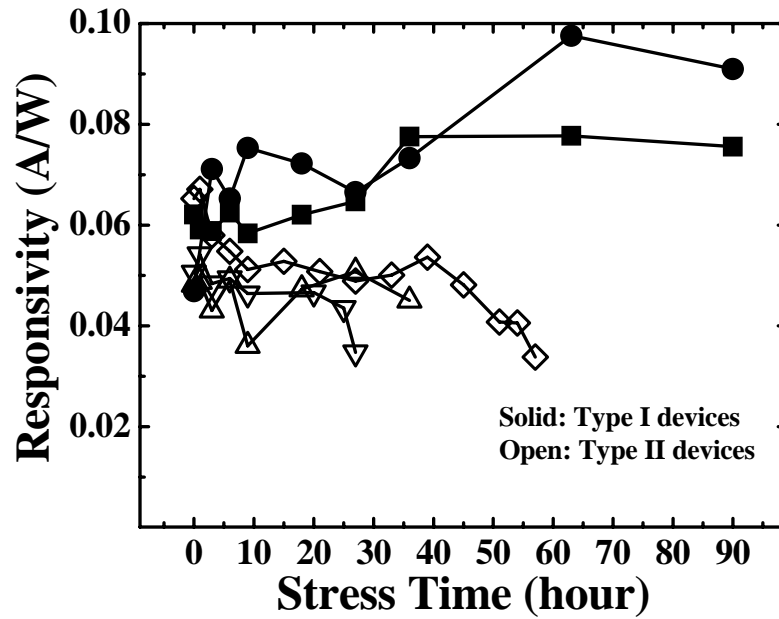


Figure 5.10: Responsivity at 350 nm as a function of stress time for both type I and type II photodiodes.

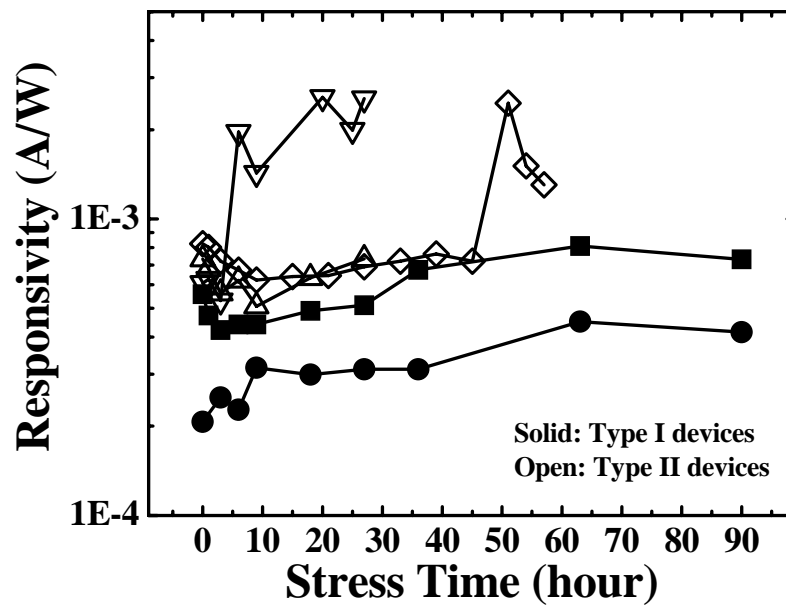


Figure 5.11: Responsivity at 400 nm as a function of stress time for both type I and type II photodiodes.

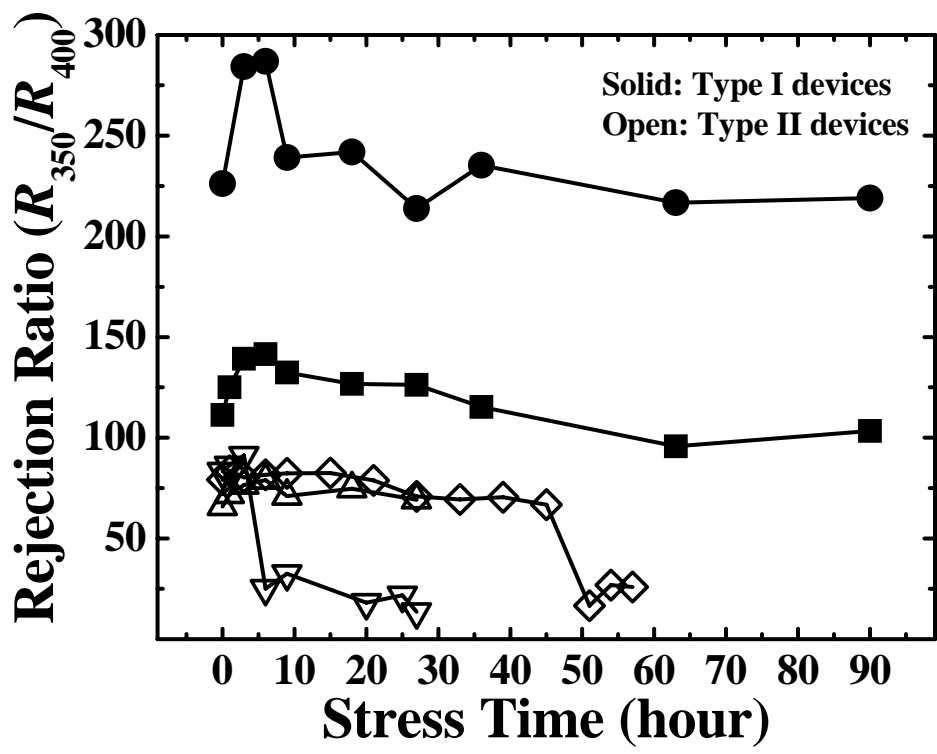


Figure 5.12: Rejection ratio of stressed devices as a function of stress time.

In general, it is observed there is a significant degradation in both the responsivity as well as the rejection ratio ( $\mathfrak{R}_{350nm} / \mathfrak{R}_{400nm}$ ) in the type II devices, due to the decrease in the responsivity at 350nm as well as the increase in the response of photons with energies smaller than the bandgap. Such degradations can be explained by the generation of traps in the bandgap region of the GaN films. This is consistent with the observed changes in both the junction capacitance and the  $I$ - $V$  characteristics among the type II devices, which are also believed to arise from the generation of interface traps.

### 5.1.5 Experimental Results on Low-frequency Noise Measurements

The experimental data on the  $I$ - $V$  and  $C$ - $V$  characteristics and the responsivity measurements indicate that high power UV radiation illumination has led to degradation in the device characteristics. In particular, for type II devices, catastrophic failure in the devices is commonly observed for  $t_S < 90$  hours. This phenomenon has been attributed to the generation of localized states in GaN films. In order to provide further evidence for the trap origin of the observed failure among the type II devices, a systematic investigation in the low-frequency noise characteristics of the devices has been conducted. It has been pointed out in previous chapters that the noise power spectral density,  $S_V(f)$ , of the devices is shown to be directly proportional to the trap density at the interface, as given by [109, 111, 117, 118]

$$S_V(f) = 4\Delta I^2 R^2 \int_x \int_y \int_z \int_E N_T(x, y, z, E) \frac{\tau}{1 + \omega^2 \tau^2} dx dy dz dE \quad (5.1)$$

where  $\Delta I$  is the current fluctuation arising from the capture of a single electron by an interface trap and  $\omega$  is the frequency. Careful examination of Eq. 5.1 shows that the Lorentzians peak sharply at energy  $E_p = -k_B T \ln(\omega\tau_0)$ , stipulating that the noise power spectral density is directly proportional to the trap density at  $E=E_p$ . Based on Eq. 5.1 and following the Thermal Activation model, measurement of  $S_V(f)$  would be useful for monitoring the change in  $N_T(E)$  of the device as a function of externally applied stress. Here the normalized trap density is defined as:

$$N_{TR}(E_p) = \frac{4C_i f}{k_B T} S_V(f, T) \quad (5.2)$$

in which  $C_i$  is the proportionality constant.

As shown in Fig. 5.13, both type I and type II devices show similar input-referred spectral noise densities  $S_V(f)$  prior to the optical stress. However, upon irradiation of the devices with high power UV radiation, the two types of devices are found to behave quite differently. Figure 5.14 shows the normalized noise factor of studied devices, defined as  $F_n = S_V(f, t_S) / S_V(f, t_S = 0)$ , where  $f = 36$  Hz, as a function of  $t_S$ . In general, it is observed that type II devices degrade at a much faster rate compared to type I devices. The experimental data show that for type I devices, the normalized noise factor, exhibits little change with  $t_S$ . However, catastrophic increase in  $F_n$  is observed in all type II devices tested. The experimental results clearly indicate substantial increase in the trap density in type II devices as they are being subjected to high intensity UV radiation.

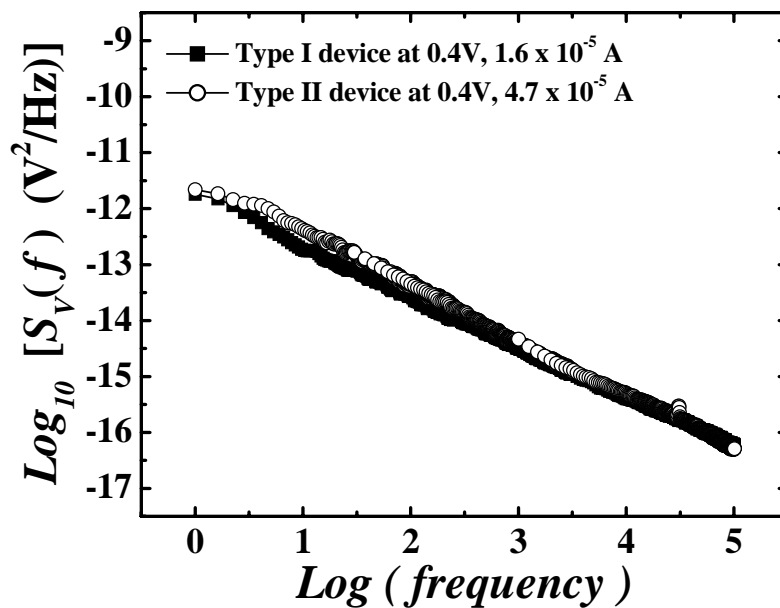


Figure 5.13: Experimental  $S_V(f)$  for typical type I and type II devices before optical stress.

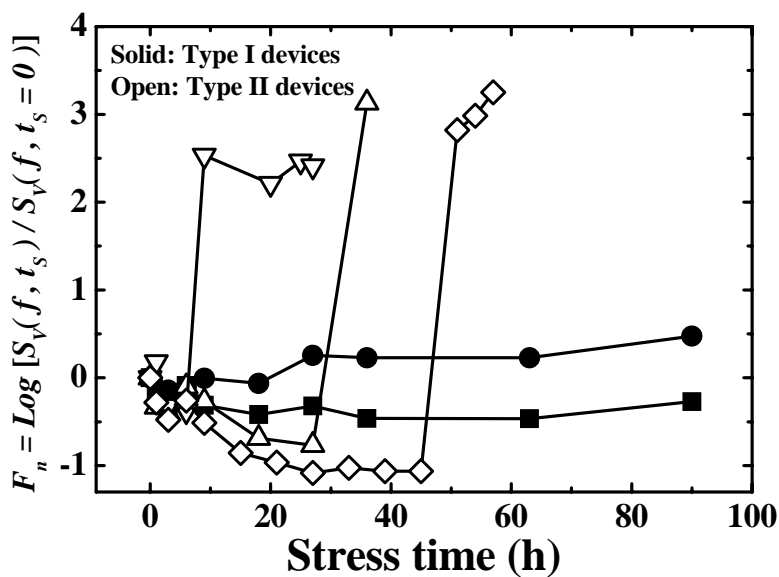


Figure 5.14: Experimental values of  $F_n$  plotted as a function of  $t_s$  for type I and type II devices.

The experimental data presented above clearly indicate that while both types of devices have comparable properties prior to the application of optical stress, and catastrophic degradation can be observed in type II devices upon irradiating the devices with high intensity UV radiation. Also, there are large variations in the onset of the catastrophic degradation among the type II devices. The data so far indicate that the degradations in the device characteristics arise from generation in the defect states in the device. This is consistent with the observed drop in the responsivity in type II devices subsequent to optical stress, as shown in Fig. 5.9. This investigation clearly shows that UV detectors fabricated on GaN films grown with the use of an ITBL, result in significant improvement in device reliability when exposed to high intensity UV radiation.

### 5.1.6 Discussion

In the investigations of the optoelectronic properties of GaN-based UV detectors, a common trend in the device characteristics was observed. Prior to the exposure of the devices to high level UV radiation, both types of devices exhibit highly comparable characteristics. This can clearly be seen from Figs. 5.2, 5.6, 5.8 and 5.13, which demonstrates that both type I and type II devices have similar  $I$ - $V$ ,  $C$ - $V$ , responsivity and low-frequency noise properties. However, once the devices were subjected to optical stress, one observes significant differences in the behaviour between the two types of devices. In general, the changes in device characteristics among the type I devices are found to be relatively gradual. Of all the type I devices tested, not one exhibited any form of catastrophic breakdown in the device characteristics, up to the stress time of 90 hours under UV radiation with an intensity of  $4 \text{ Wcm}^{-2}$ . On the other hand, for type II devices, it is observed that the devices exhibit gradual changes in the device characteristics during early stages of stressing, however, it is generally found that the devices demonstrate catastrophic breakdown beyond a certain stress time,  $t_S$ . This phenomenon is clearly observed in Figs. 5.4, 5.5, 5.7, 5.9, 5.14. It is noteworthy that of all the type II devices tested, all of them experienced catastrophic failure at some point in which  $t_S < 90$  hours.

Detailed investigations of the dependence of the low-frequency excess noise as a function of  $t_S$  indicated that significant increase in the trap density is associated with the catastrophic breakdown of the type II devices. Such increase in the trap density is

attributed as the underlying cause for the breakdown in the  $I$ - $V$ ,  $C$ - $V$  and responsivity of the devices. An increase in the interface trap density at the Schottky junction leads to a corresponding increase in the trap assisted tunneling through the junction, as shown in Fig. 5.15, thereby establishing an alternative conduction path through the Schottky junction. When there is a high density of localized states at the junction, the device eventually loses its Schottky rectifying characteristics and becomes ohmic, as observed in the experiment.

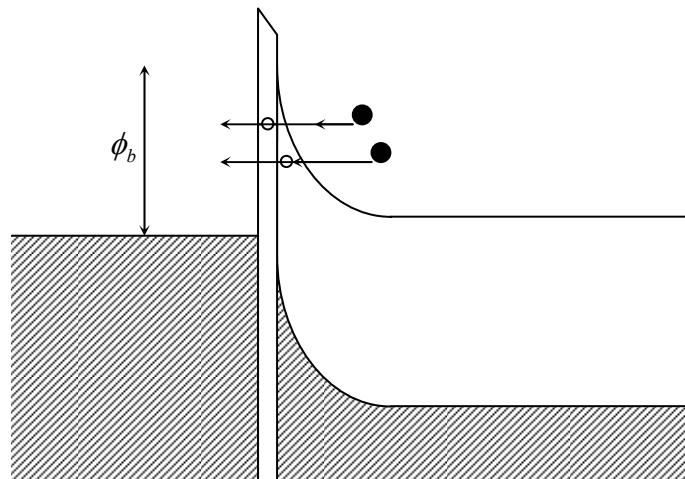


Figure 5.15: Schematic diagram of the carrier tunneling process through localized states in a Schottky barrier contact.

This alternative conduction path also “shorts out” the capacitor leading to a substantial drop in the junction capacitance, as observed in Fig. 5.7. Another effect arising from the generation of localized states in the bandgap is the corresponding increase in the sub-bandgap responsivity. For an ideal GaN-based UV photodiode one would expect a very low sensitivity to photons at wavelengths above 364 nm since this corresponds to the bandgap of the GaN film. However, due to the presence of the defect states within the bandgap, photons with energies smaller than the bandgap will be able to excite electrons residing in the bandgap states, as shown in Fig. 5.16 below.

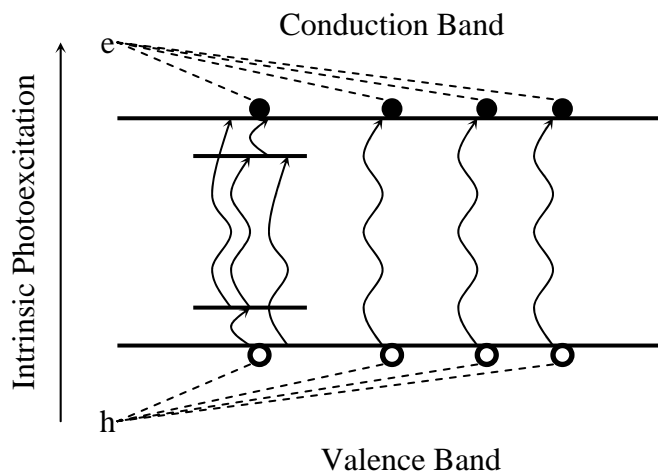


Figure 5.16: Schematic diagram of photo-electrons excitation process by defect state within the bandgap.

The experimental results show that as the devices are subjected to optical stress, an increase in the sub-bandgap responsivity is invariably observed. The work of Emtsev *et al.* [119] has shown that such increase in the yellow luminescence band in GaN films is related to the radiation induced defects. Hence, the experimental data clearly show that the degradation of the device characteristics arises from the generation of defect states within the GaN material.

Based on the discussions above, one can also conclude that GaN thin films grown using a double buffer layer structure - a conventional high temperature AlN buffer layer and an intermediate temperature buffer layer, demonstrate an improved radiation hardness in comparison to films grown with the use of just a conventional buffer layer. To account for this phenomenon, it is noted that previous studies on the optoelectronic properties of GaN epitaxial layers grown with the use of an ITBL, exhibit a systematic improvement in the PL intensity, the FWHM and the electron mobility, which is shown in Figs. 3.7a and b and is reproduced below in Figs. 5.17 and 5.18. The improvement in the PL and mobility indicates a corresponding improvement in the material quality of the films. In addition, it was also observed that there were systematic shifts in the peak wavelengths of the PL spectra, as shown in Fig. 5.18. The shift in the PL peak signifies a systematic change in the lattice constant and this stipulates a relaxation in the residue strain of the material. A blue shift in the PL peak suggests an increase in compressive stress during the growth process and hence an improvement in the two-dimensional mobility of the adsorbed species on the growth surface. This corroborates the improvement in the FWHM of the PL spectra, which indicates a corresponding

improvement in the crystallinity of the film. It is believed that such improvement in the crystallinity of the GaN film is ultimately responsible for the observed improvement in radiation hardness of the Ni/n-GaN UV photodiodes.

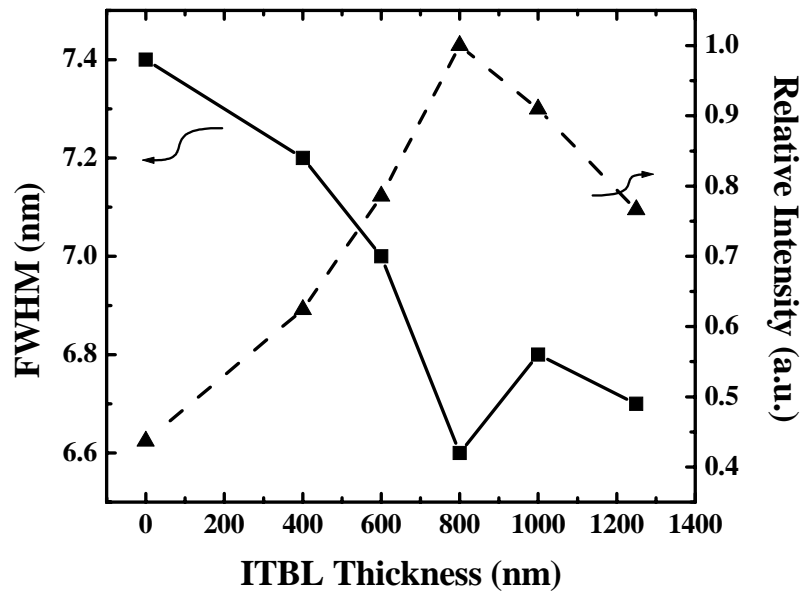


Figure 5.17: The FWHM and the relative intensity of the bandedge emission of GaN films plotted against the thickness of ITBL [79].

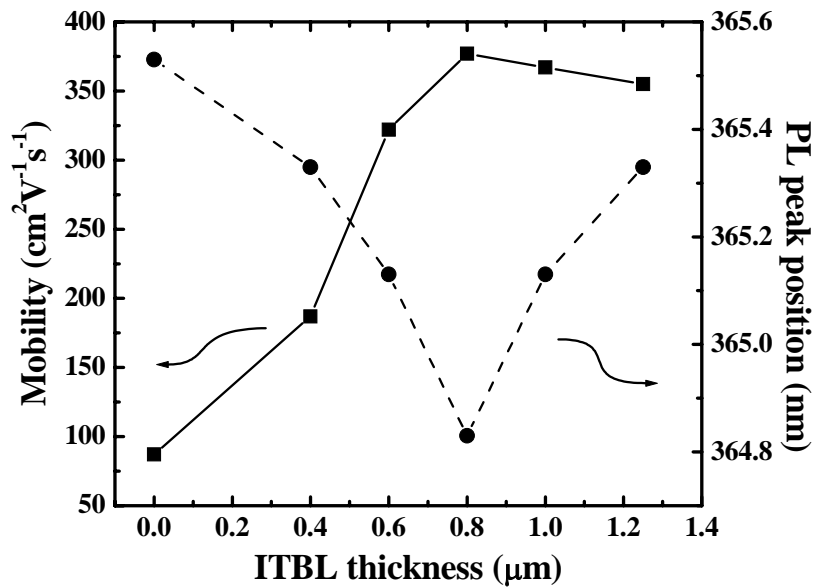


Figure 5.18: Hall mobility and PL peak position at different ITBL thicknesses [79].

## 5.2 Experiment II: Development of ITO/n-GaN UV Photodiodes

### 5.2.1 Indium Tin Oxide (ITO)

There are many advantages in the use of a metal/semiconductor Schottky barrier structure for the fabrication of photodetectors, such as simplicity in the fabrication process and high speed operation [22, 23]. However, there are some inherent disadvantages in the Schottky photodiode as well. To enable the light to be absorbed by the active region of the device, a semi-transparent metal layer, with high work function, such as Ni, Au or Pt, is commonly e-beam deposited on slightly n-doped epitaxial grown GaN films. The thickness of the metal layer is usually kept thin, of the order of a few tens of angstroms, to allow for efficient optical absorption. This semi-transparent metallic layer forming the Schottky junction, however, is highly absorptive and reflective, and these devices usually suffer from high series resistances and low efficiencies. In order to address these problems, a practically transparent and highly conductive contact layer is required. It has been reported that a number of wide-bandgap oxide films of tin, indium, cadmium, zinc and their alloys exhibit high transmittance and nearly metallic conductivity [120, 121]. To date, most research effort has been concentrated on  $\text{In}_2\text{O}_3:\text{Sn}$  commonly known as indium tin oxide (ITO). The material possesses excellent electrical and optical properties, and as a result, a wide range of electronic, optoelectronic and mechanical applications that take advantage of the superior properties of ITO have been reported. Traditional applications utilizing ITO

thin films include transparent heating elements of aircraft and car windows, antistatic coatings over instrument display panels, heat reflecting mirrors and antireflection coatings. ITO has also found important applications in optoelectronic devices such as charge-coupled device (CCD) arrays and liquid crystal displays (LCD) as a transparent electrode [120-122]. More recently, ITO has been used as a transparent contact in advanced optoelectronic devices such as solar cells, light emitting diodes, photodiodes and lasers [120, 123-125]. It is clearly demonstrated that ITO is becoming an integral part of modern electronic devices and has the potential to significantly improve the optical sensitivity of light detecting devices or the quantum efficiency of light emitting devices.

A Schottky junction can be formed by depositing ITO films directly to n-GaN, therefore, it is very attractive to use ITO to replace the semi-transparent metals in the conventional structure to produce high performance GaN-based Schottky photodetectors [126-130]. In this study, the properties of GaN-based UV photodiodes by e-beam deposition of ITO films onto the GaN as transparent electrodes are explored. The fabrication and characterization of ITO/n-GaN Schottky junction visible-blind UV photodiodes are presented in the following sections. The optical and electronic properties of the devices are characterized by  $I$ - $V$  characteristics, photo-responsivity and low-frequency noise measurements. The work also includes investigations into a unique device structure in which a thin Ni layer is deposited between the ITO and n-GaN film for the passivation of the GaN surface. The optoelectronic properties of this novel device are discussed in the following sections.

### *Properties of ITO*

Indium Tin Oxide is formed by doping indium oxide with tin (Sn), in which Sn replaces the  $\text{In}^{3+}$  atoms from the bixbyte lattice structure of  $\text{In}_2\text{O}_3$ . The Sn atoms thus form an interstitial bond with oxygen, either as SnO or  $\text{SnO}_2$  with valency of +2 and +4 respectively. The lower valence states act as traps and capture free electrons, which as a result, reduces the bulk conductivity. However,  $\text{SnO}_2$  acts as an n-type donor and creates free electrons in the conduction band. In addition, beside the substitutional tin creating free electrons, non-stoichiometric alloys produce oxygen vacancies which also contribute to the high conductivity of the material [120, 131, 132].

Being a wide bandgap semiconductor, ITO has high optical transmittance in the solar spectrum. The optical bandgap of ITO films is generally greater than 3.75 eV, although a range from 3.5 to 4.1 eV have also been reported in the literature [133, 134]. The fundamental absorption edge generally lies in the ultraviolet end of the spectrum and shifts to shorter wavelengths with increasing carrier concentration. This is because the bandgap exhibits an  $N^{2/3}$  dependence due to the Burstein-Moss shift [132, 135, 136]. Crystalline  $\text{In}_2\text{O}_3$  exhibits a bixbyte structure with a unit cell containing 40 atoms and two non-equivalent cation sites. A more fundamental understanding of ITO's electrical conductivity has been given by Odaka *et al.* [137]. They suggested that a Sn atom replacing an In atom leads to the formation of three impurity bands with s-like symmetry and one of these bands overlaps the conduction band of  $\text{In}_2\text{O}_3$ . As a result,

the Fermi level of ITO is located in this band, which accounts for the high electron concentration of the material.

### *ITO Deposition Techniques*

Various deposition techniques have been explored to produce high-quality ITO films in the literature. Both sputtering and electron-beam evaporation are the most extensively used techniques for the deposition of ITO. Other techniques are also used, including pulsed laser evaporation, spray pyrolysis and screen printing [138-145]. The choice of the particular deposition technique is determined by a number of factors, such as film quality, uniformity over a wide section, reproducibility, cost and the limitations and drawbacks of each technique. In addition, since the physical properties of ITO are sensitive to its microstructure, stoichiometry, and the nature of the impurities present, it is obvious that the optoelectronic properties of the films critically depend on the parameters of the deposition process.

The sputtering deposition technique is a popular choice for the deposition of a wide range of materials. In this process, the source atoms are knocked out of the target material by accelerated ions from glow discharge plasma and transported to the substrate wafers in a vacuum. Various techniques can be used to accelerate the plasma ions giving rise to the d.c. sputtering and rf sputtering techniques. In the magnetron sputtering process, a magnetic field is used to trap secondary electrons close to the target. The electrons follow helical paths around the magnetic field lines, undergoing

more ionizing collisions with neutral gaseous ions near the target and sputtering occur. This allows the process to take place at a much lower pressure. It is known that the sample surface can be substantially damaged due to the energy flux directed to it during the deposition process. This may affect the resulting device properties, especially the optical and electronic characteristics of the diode [146].

In this study, the electron beam (e-beam) deposition process was chosen for the fabrication of ITO/GaN UV photodiodes. Electron beam evaporation is one of the most widely used and successful techniques for producing high quality ITO films [130, 138, 139, 142]. In general, ITO evaporation sources consisting of  $\text{In}_2\text{O}_3$  and  $\text{SnO}_2$  in a ratio of 9:1 by weight, are heated and vaporized by an electron beam and subsequently deposited on the substrate. Usually oxygen is introduced in the chamber during deposition to restore the stoichiometric as dissociation and oxygen loss are induced by evaporation. There is no damage associated with e-beam deposition since there are no energetic ion bombardments during deposition. The deposition parameters, including oxygen partial pressure and substrate temperature, play a critical role in the film's properties. Detailed optimization of the deposition parameter of ITO/GaN Schottky photodiode is presented in the following section.

### *Transmittance Measurement*

In order to characterize the optical properties of the ITO films, the transmittance of the ITO films was measured over 250 – 800 nm wavelength range. Transmittance is defined as

$$\text{Transmittance}(\lambda) = \frac{OP_{film}(\lambda)}{OP_{blank}(\lambda)} \times 100\%. \quad (5.3)$$

where the  $OP_{blank}(\lambda)$  is the light power transmitted through the blank sample at the particular wavelength  $\lambda$  and  $OP_{film}(\lambda)$  is the light power transmitted through the films and the substrate. The blank sample is normally the identical bare substrate used for the film deposition and this is used to eliminate the transmittance of the substrate from the overall results.

The experimental setup for transmittance measurements shown in Fig. 5.19 is similar to responsivity measurement. A Xenon lamp was used as the light source, and a monochromator for wavelength selection. The monochromatic beam from the monochromator was converged by a UV enhanced silica lens and allowed to pass through a pinhole and reach the sample under test. The transmitted power was measured as a function of wavelength using a Newport Model 840 handheld optical power. This step was then repeated using a quartz blank sample and another quartz sample coated with an ITO film. Following Eq. 5.3 the transmittance was calculated as a function of the wavelength.

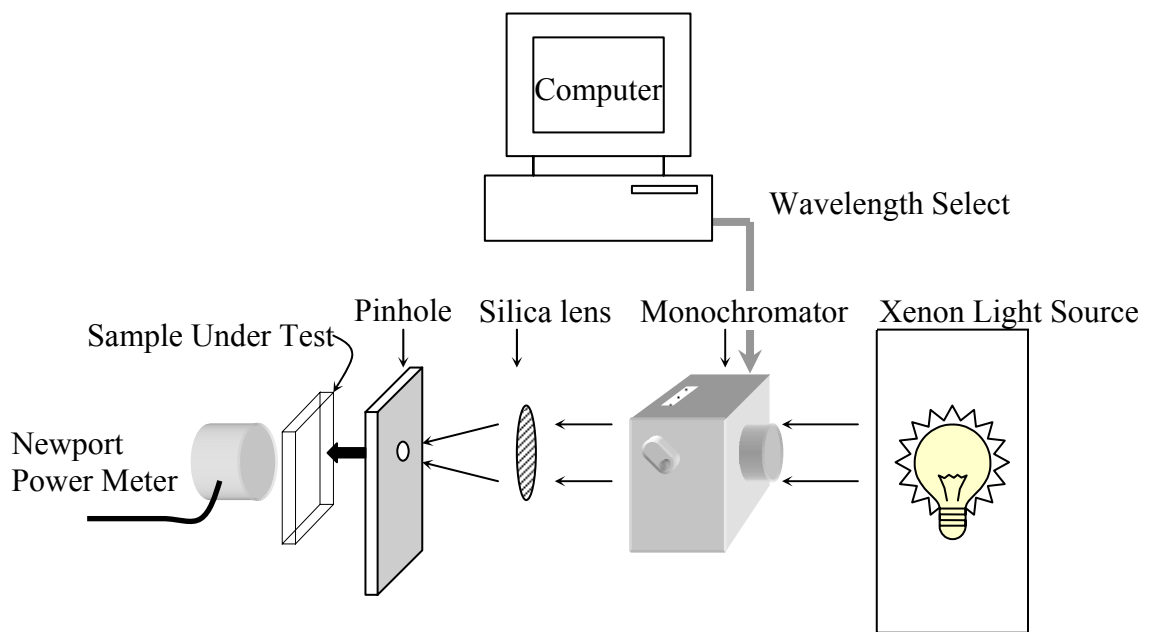


Figure 5.19: Schematic of the transmittance measurement setup.

### 5.2.2 ITO Deposition and Fabrication of ITO/n-GaN UV Photodiodes

The ITO/n-GaN UV photodiodes were fabricated on slightly n-doped GaN epilayers which were grown on (0001) sapphire substrates by rf plasma-assisted MBE. Similar to the type I devices as described in the previous section, the ITO/n-GaN UV photodiodes were fabricated on a novel double buffer layer structure consisting of a 20 nm AlN high temperature buffer layer and an 800 nm GaN ITBL. A lightly Si doped GaN epitaxial layer of thickness about 1  $\mu\text{m}$  was deposited at about 740°C on top of the ITBL layer. Hall measurement shown that typical carrier concentration was around  $5 \times 10^{17} \text{ cm}^{-3}$ . The same MBE deposition processes, as described in Chapter 5, were adopted for the GaN epitaxial growth in this work.

The device structure and the dimensions were largely the same as the Ni/n-GaN devices, with the exception that the Schottky contacts were formed by an ITO layer. Figure 5.20 shows the schematic cross-sectional view of the ITO/n-GaN Schottky photodiode. The ohmic contacts consisted of an e-beam deposited Ti/Al (20 nm/20 nm) bi-layer and were rapid thermal annealed at 800°C in nitrogen ambient for 60 s. After the formation of ohmic contacts, ITO films were deposited onto the n-GaN layers, using an AST Peva 400ES electron beam evaporator.

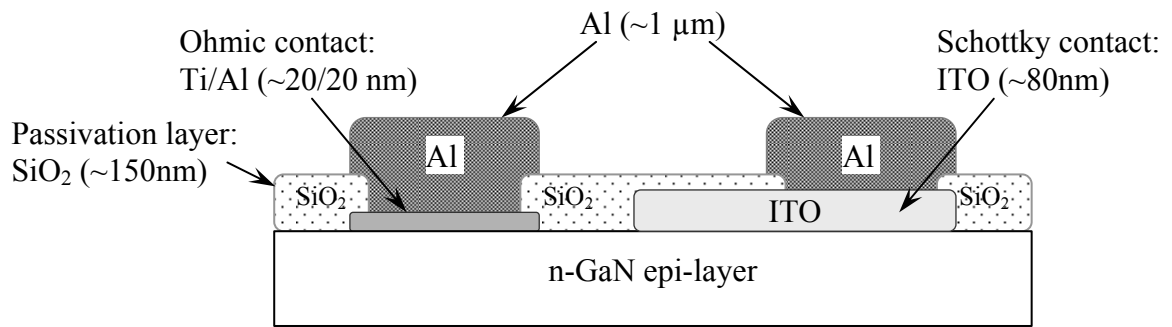


Figure 5.20: Device cross sectional view of the ITO/n-GaN Schottky photodiode.

The deposition parameters of the ITO strongly affect the optoelectronic characteristics of the resulted film. The principal deposition parameters are substrate temperature, oxygen partial pressure, the deposition rate and material composition. In this study, the deposition conditions were optimised by systematically varying the substrate temperature and partial pressure of oxygen, while the deposition rate and the source material composition was being fixed. The ITO evaporation source consisted of a mixture of  $\text{In}_2\text{O}_3$  and  $\text{SnO}_2$  in a ratio 9:1 by weight, in pellet form. The background pressure was maintained at about  $5 \times 10^{-6}$  Torr. The deposition rate and the thickness of the ITO layer were monitored using an oscillating crystal sensor, and the rate was kept at 0.1 nm/s and a total thickness of 80 nm was used throughout this study. The deposition parameters for the ITO layer were optimized by systematically varying the substrate temperature from 167 to 224°C and the oxygen flow rate from 1 to 5 sccm, which correspond to an equivalent working pressure between  $1 \times 10^{-3}$  to  $8 \times 10^{-3}$  Torr. The oxygen partial pressures were calibrated against the flow rates, as shown in Fig. 5.21. Parallel to the ITO deposition on GaN, the ITO was also deposited on quartz substrates placed next the GaN substrate. This was used to characterize the optical transmission of the ITO films. Prior to the evaporation, the substrate was heated to the predetermined temperature at a rate of 10°C per minute and stabilized for at least 30 minutes. This was followed by introducing oxygen into the evaporation chamber at a set rate to maintain a specific oxygen partial pressure. The oxygen flow rate was controlled by a mass flow control (MFC) unit.

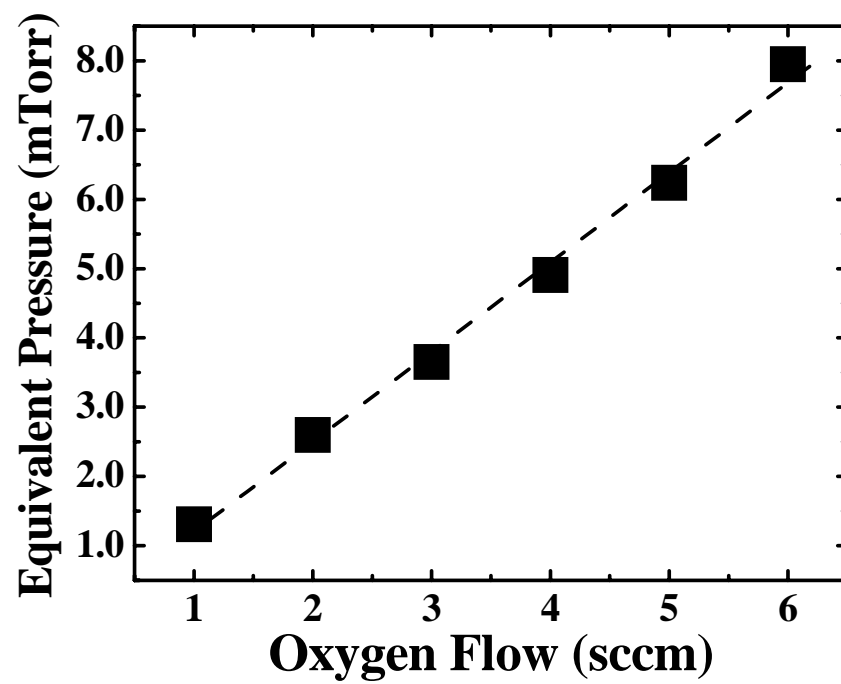


Figure 5.21: Oxygen partial pressure against flow rate of the e-beam system.

The evaporation procedure starts by sweeping a low power electron beam on the ITO pellet to slowly and uniformly fuse the surfaces of the material, without boring a tunnel with the beam. During this time, the substrate was shielded by a shutter placed over the source to prevent the outgassing material from contaminating the substrate surface. While monitoring and minimizing the pressure and spitting level, the e-beam emission power was slowly increased to evaporation power. Once the pre-conditioning was completed, the shutter was opened and the deposition process begin.

After the deposition of the ITO film, the wet chemical etching technique was used to define the active area of the diode. The active region of the ITO/GaN Schottky photodiode was first defined by standard photolithography. Then, an aqueous solution of H<sub>2</sub>O : 35%-HCl in a 9 : 1 ratio was used for the wet etching process. During the etching process, the solution was heated to 50°C to increase the etch rate. Figure 5.22 shows the etching depth as a function of the etch time. A calibrated etching rate of 14 Å/s was determined from the experimental data. This enabled a fine definition of the ITO contact without severe over-etch. This was followed by the deposition of a 150 nm thick layer of SiO<sub>2</sub> by e-beam evaporation, which served as the passivation layer. Finally, the bonding pads consisting of 1µm thick layer of Al were deposited by e-beam evaporation.

After the completion of the fabrication process, the samples were scribed into small pieces using a diamond scriber. The devices were then attached to a 24-pin dual-in-line ceramic package by silver paint and connected electrically to the package by wire bonding.

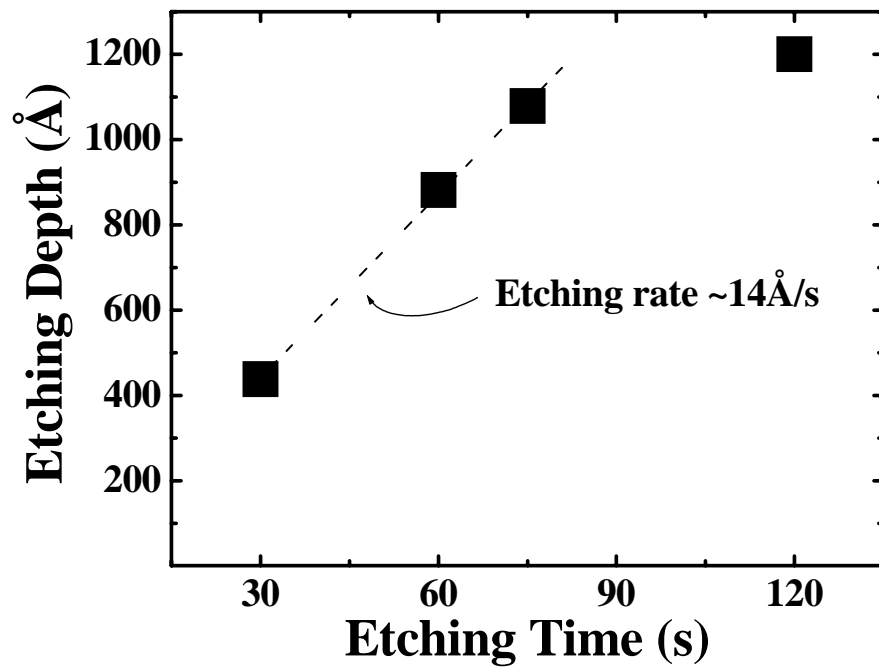


Figure 5.22: Measured ITO etching depth as a function of the etching time.

The devices were characterized by  $I$ - $V$ , low-frequency noise and photo-responsivity measurements. The photo-responsivities of the devices were characterized using a 150 W Xenon (Xe) lamp light source and a monochromator. Details of the responsivity measurements are described in Chapter 4. For the measurement of low-frequency noise, the devices were forward biased using a battery-powered constant voltage source and the current fluctuations of devices were measured. The fluctuating current was converted to a voltage signal with a Stanford Research SR560 low-noise current-to-voltage converter and the input-referred current noise power spectral density,  $S_I(f)$ , was then measured with an HP 3561A dynamic signal analyzer. The detailed experimental setup for noise measurements is described in Chapter 4.

### 5.2.3 Experimental Results and Discussion

First, the growth parameters for the ITO films were optimized. Since the substrate have significant effects on the properties of the films, the deposition parameters were optimized by detailed characterization of the optoelectronic properties of complete ITO/n-GaN UV photodiodes, fabricated under different deposition conditions. The performances of the photodiodes were assessed by measuring their responsivities as a function of the fabrication parameters and the results are summarized in Table 5.2. Experimental results shown that the device characteristics were strongly dependent on the ITO deposition conditions. It was determined that the optimal substrate temperature and oxygen flow rates for the system were 186°C and 3 sccm (device ID: T186O3), respectively. Under the optimized conditions, device T186O3 exhibited the highest

responsivity of 0.0413 A/W at 350 nm, which was indicative of the high transmission coefficient for the ITO films deposited under such conditions. A similar trend of improvements was also observed for the UV/visible rejection ratio (at  $\mathfrak{R}_{350nm} / \mathfrak{R}_{500nm}$ ) which indicated a value close to 2.5 orders of magnitude for the optimized device. Compared to device T167O3, with a deposition temperature of 167°C and the same oxygen flow rate, the optimized device exhibited a 2.7 fold improvement in the UV/visible rejection ratio.

Samples ID	Substrate Temperature (°C)	Oxygen flow (sccm)	Responsivity @ 350 nm (A/W)	Rejection Ratio ( $\mathfrak{R}_{350nm} / \mathfrak{R}_{500nm}$ )
T167O3	167	3	0.0387	102.0
T186O3	186	3	0.0413	288.7
T205O3	205	3	0.0372	149.0
T224O3	224	3	0.0333	186.3
T186O1	186	1	0.0383	86.0
T186O2	186	2	0.0231	66.1
T186O3	186	3	0.0413	288.7
T186O4	186	4	0.0179	176.8
T186O5	186	5	0.0234	210.0

Table 5.2: Summary of the ITO layer growth conditions, ITO/n-GaN photodiodes responsivities and rejection ratios.

Typical experimental data on the transmission of the ITO films from 250 to 800 nm are shown in Fig. 5.23. As shown in the figure, a transmittance of around 90% was achieved for wavelengths between 340 nm to 800 nm. However, the transmittance drops sharply below 340 nm and this corresponding to the fundamental absorption edge of ITO. The transmittance at 300 nm is around 63%. This is compared to the transmittance of 15nm Ni nm, as shown in the same graph, which is relatively constant at around 65% - 70% over the range from 250 nm to 800 nm. The results clearly evident that ITO has a higher transmission, compared to the 15 nm Ni from the range above ~300 nm, and hence is a potential candidate for fabrication of high performance UV photodiodes. The full spectral responsivity curves for the ITO/n-GaN UV photodiodes fabricated under different ITO deposition conditions are shown in Fig. 5.24.

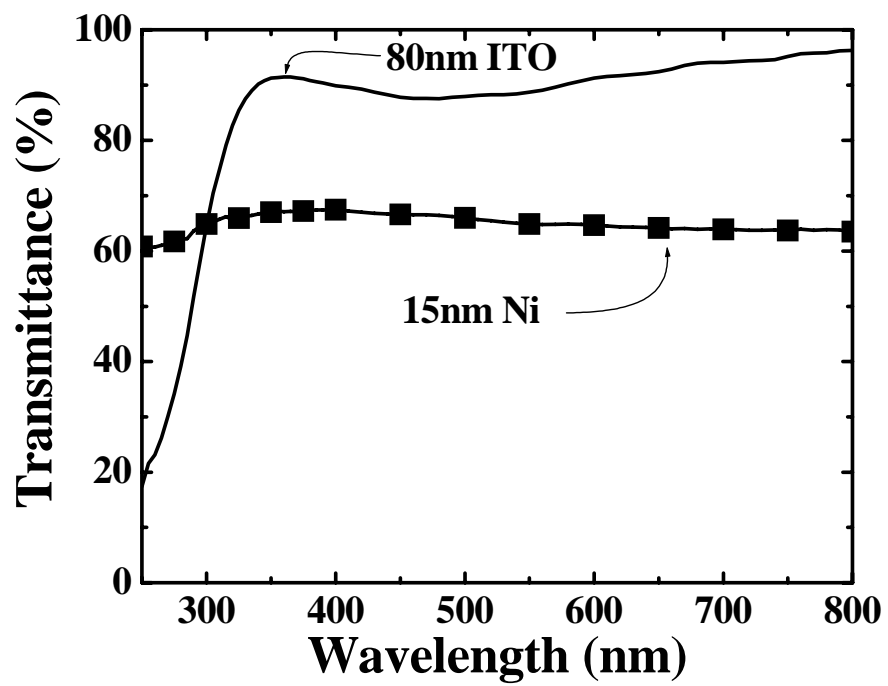


Figure 5.23: Typical transmittance spectrum of 80 nm ITO and 15 nm Ni e-beam evaporated on quartz substrates.

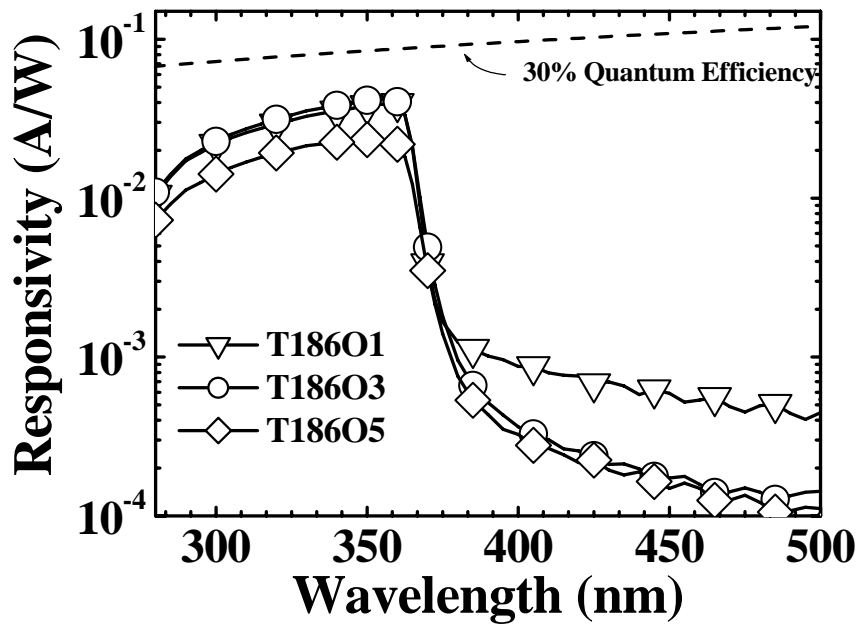
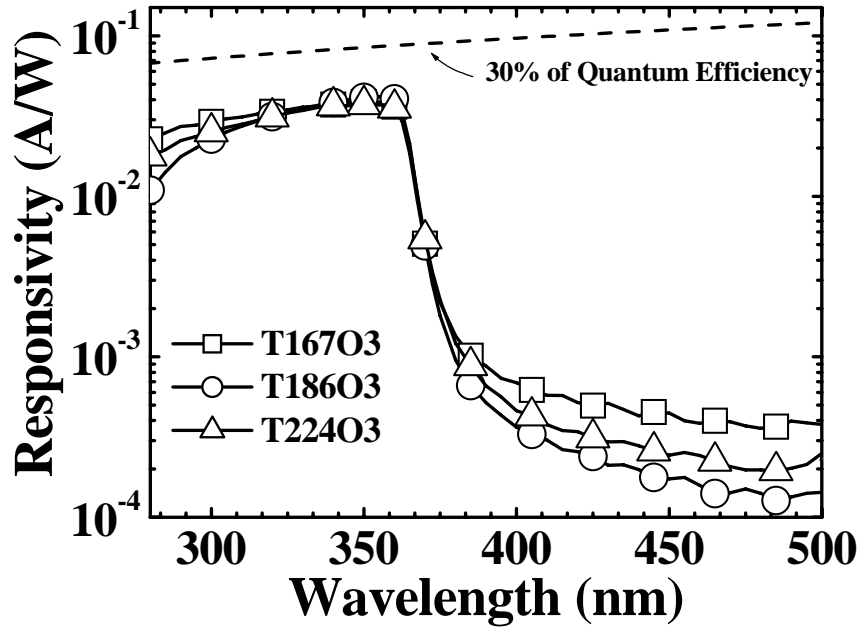


Figure 5.24: Spectral current responsivity curves for devices fabricated at different ITO deposition conditions. Dashed line shows the theoretical calculated responsivity of 30% quantum efficiency for eye guidance.

Typical room temperature  $I$ - $V$  characteristics of the device fabricated under the optimised ITO deposition conditions are shown in Fig. 5.25. For this particular device, a  $3.37 \times 10^{-7}$  A reverse leakage current was measured at -1 V bias. Typical  $C$ - $V$  measurement results of the device, plotted as  $C^{-2}$  versus  $V$ , are shown in Fig. 5.26. The calculated carrier concentration for this device is  $8.1 \times 10^{17} \text{ cm}^{-3}$  and which is in good agreement with the applied doping concentration of the GaN film ( $5 \times 10^{17} \text{ cm}^{-3}$ ). The Schottky barrier height,  $\phi_b$ , extracted from the  $C$ - $V$  characteristic shown in Fig. 5.26 is equal to 1.48 eV.

It is interesting to note that the reverse biased currents of these photodiodes also exhibit a strong dependence on the ITO deposition conditions, as shown in Figs. 5.27 and 5.28. The results show that the reverse biasing current at -1 V increases as the flow rate of oxygen and substrate temperature decreases. The increase in the reverse biased current can be explained by the variation in the stoichiometry of the ITO/GaN interface under different ITO deposition conditions. It is suggested that varying the deposition temperature and the oxygen partial pressure may affect the stoichiometric of the deposited ITO thin film. Work by Chiou *et al.* [130] shows that oxygen deficiency in ITO film results in the In-rich condition which leads to the formation of InGaN at the ITO/GaN interface. The existence of InGaN may lower the contact barrier height and results in the increase of the reverse leakage current by quantum-mechanical tunnelling.

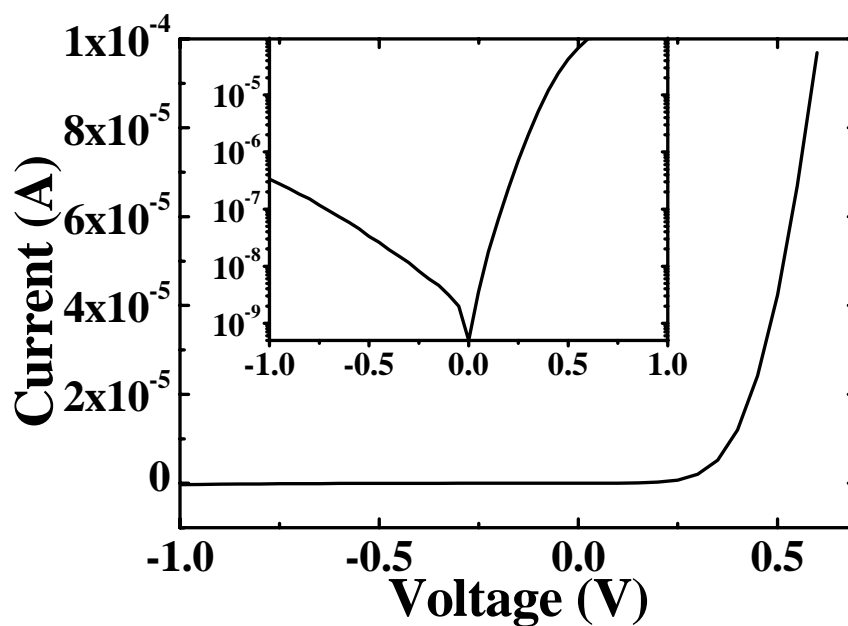


Figure 5.25: Typical  $I$ - $V$  characteristic of the ITO/n-GaN Schottky photodiode device.

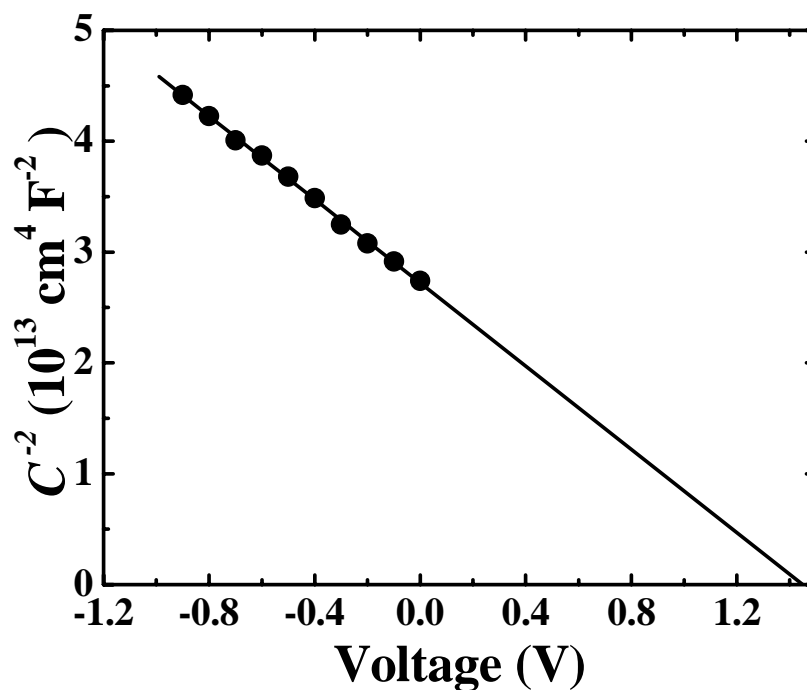


Figure 5.26: Typical  $C^{-2}$ - $V$  characteristic of the ITO/n-GaN Schottky photodiode device.

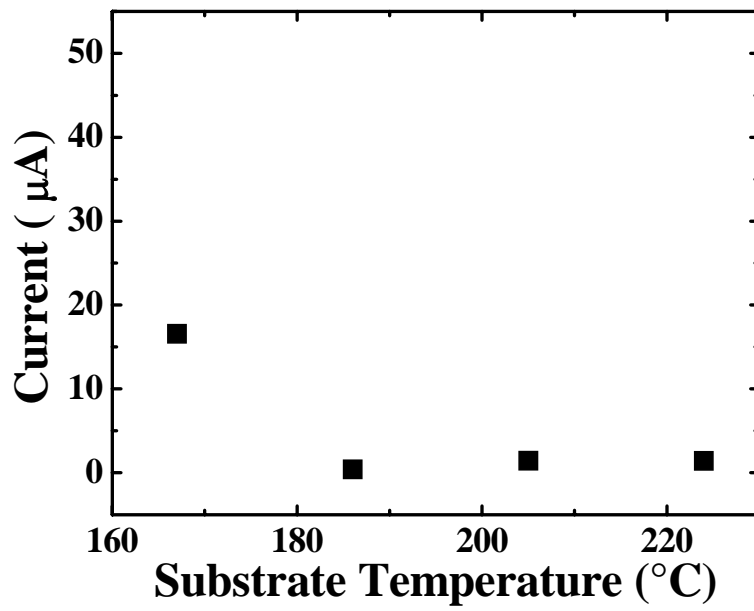


Figure 5.27: ITO/n-GaN Schottky photodiode reverse bias current at -1 V as a function of the substrate temperature.

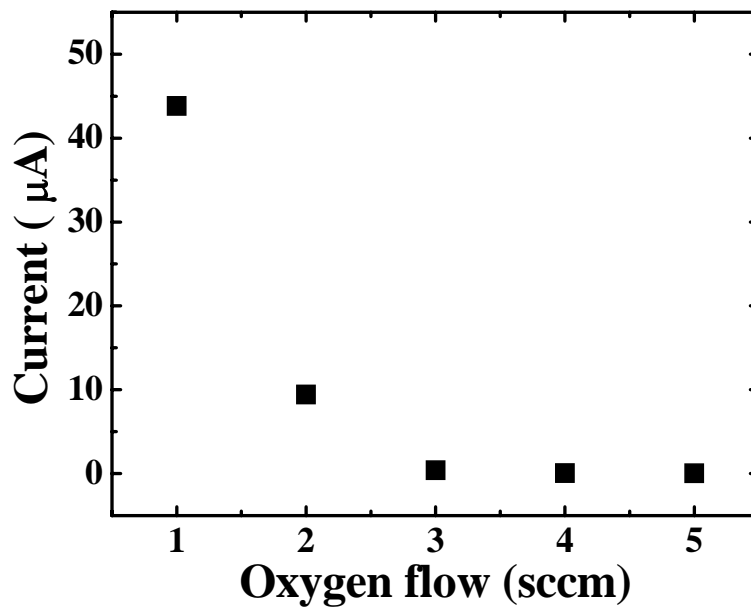


Figure 5.28: ITO/n-GaN Schottky photodiode reverse bias current at -1 V as a function of the oxygen flow.

The data indicate that the passivation of the ITO/GaN interface states may be important for the reduction in the dark current. To accomplish this, the use of a double layer Schottky contact device structure was investigated, in which a thin Ni layer is sandwiched between the ITO and n-GaN film to serve as a passivation layer of the GaN. A approximately 3 nm thick Ni layer was first e-beam deposited on the GaN surface prior to the ITO deposition. Following the thin Ni layer, the ITO films were deposited using the optimised conditions, with a 3 sccm oxygen flow and a substrate temperature of 186°C. Figure 5.29 shows the transmission spectrum of such a 3 nm Ni layer evaporated on quartz substrate. The schematic diagram of this unique device structure is shown in Fig. 5.30.

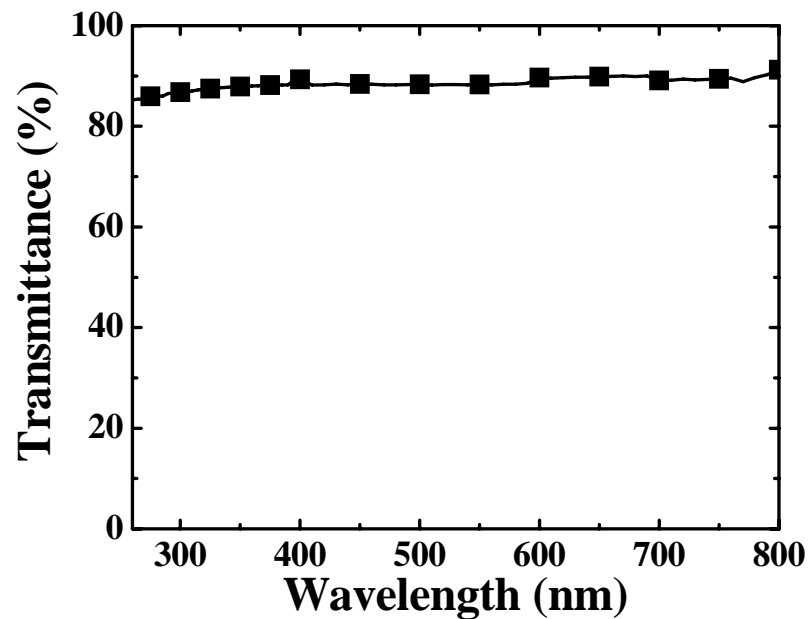


Figure 5.29: Transmission spectrum of 3 nm Ni on quartz substrate.

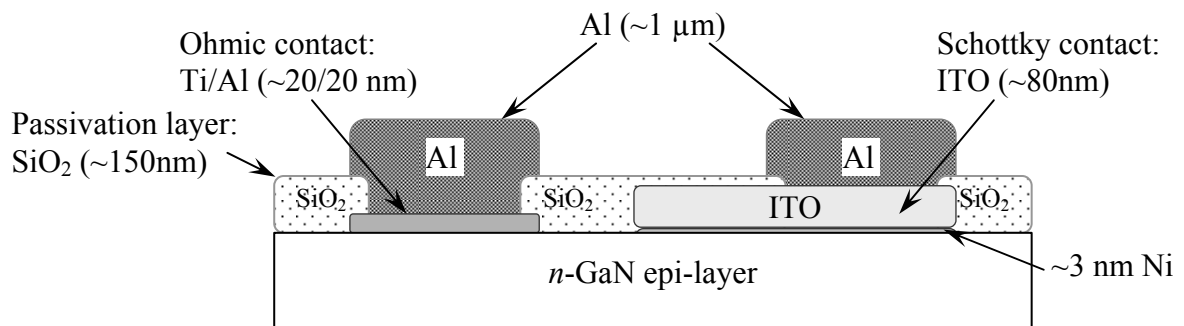


Figure 5.30: Device cross sectional view of the ITO/Ni/n-GaN Schottky photodiode.

Under the ITO deposition conditions, the thin Ni layers will be readily oxidized forming NiO<sub>x</sub>, which is found to have a passivation effect on the interface. Examination of the *I-V* characteristics indicates close to 80% reduction in the leakage current, using the double layer Schottky contact, compared to the results from the standard Ni 15nm/n-GaN device and the ITO/n-GaN device, as shown in Fig. 5.31. The experimental results on responsivity measurements also indicate substantial reduction in the signal in the visible spectrum, with a rejection ratio of about 450 for the device with a double layer Schottky contact, as shown in Fig. 5.32. Since absorption in the long wavelength range arises from trap-assisted processes, the reduction in the responsivity in the visible range indicates an improvement in the interfacial trap density [147].

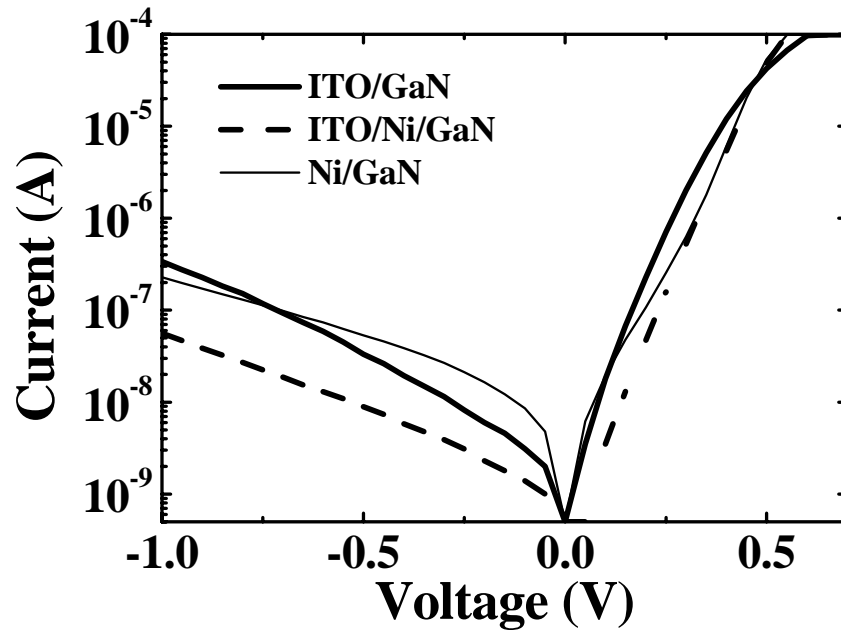


Figure 5.31: Measured  $I$ - $V$  characteristic for ITO/n-GaN, ITO/Ni/n-GaN and Ni/n-GaN Schottky photodiodes.

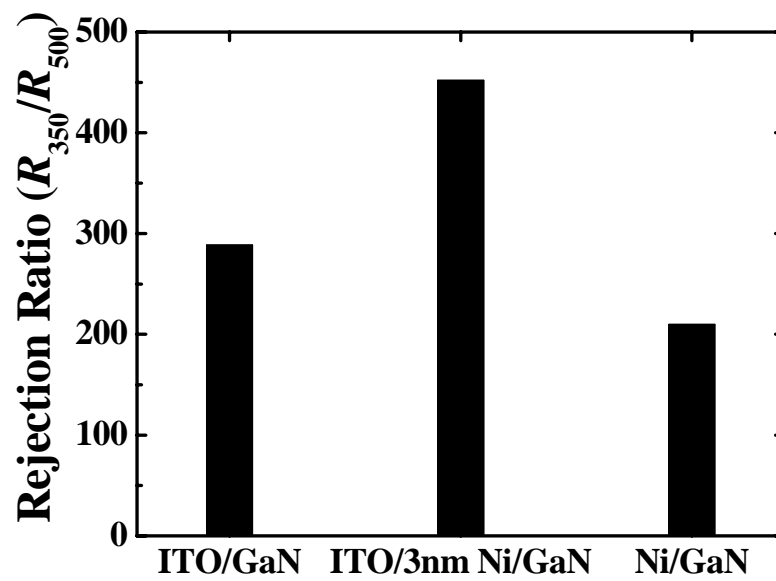


Figure 5.32: Rejection ratio of fabricated ITO/n-GaN, ITO/Ni/n-GaN and Ni/n-GaN Schottky photodiodes.

Low-frequency excess noise was measured in the Ni/n-GaN device, the ITO/n-GaN device and the ITO/Ni/n-GaN device in order to investigate the interface trap density for the three types of devices shown in Fig. 5.33. It has been shown that low-frequency excess noise in GaN-based Schottky junctions arises from the thermally activated trapping and detrapping of carriers by surface states at the metal-semiconductor interface resulting in low-frequency fluctuations of the tunneling current through the modulation of the tunneling barrier. Thus, measurement of  $S_I(f)$  can be used to monitor the surfaces states density. The current noise power spectral density,  $S_I(f)$ , is given by [109, 111, 117, 118]

$$S_I(f) = 4 \frac{I^2 (\Delta R)^2}{R_{ac}^2} \int_x \int_y \int_z \int_E N_T(x, y, z, E) \frac{\tau}{1 + 4\pi^2 f^2 \tau^2} dx dy dz dE \quad (5.4)$$

in which  $R_{ac}$  is the AC resistance of the device,  $\Delta R$  is the fluctuation in the device resistance due to the capture of a single electron by an interface trap. The salient point of Eq. 5.4 is that  $S_I(f)$  is directly proportional to the trap density. Thus,  $S_I(f)$  is an effective indicator for the material quality of the Schottky junction in addition to being an important figure of merit for the detector. Experimental measurement of low-frequency noise, as shown in Fig. 5.33, indicated that normalized current noise power spectral,  $S_I(f)/I^2$ , for three different type of devices are nearly inversely proportional to the frequency. And a close to three orders of magnitude reduction in normalized noise level was observed for the ITO/Ni/n-GaN device, compared to the ITO/n-GaN device at

a voltage bias of 0.5 V. This clearly shows that the electronic properties of the ITO/Ni/n-GaN devices can be improved by effectively passivating the ITO/GaN interface, with the use of a thin Ni layer. And the improvement were arises from the lowering of the interfacial trap density at the Schottky junction as evidenced by the reduction of low-frequency noise. The results show the use of this unique device structure, the fabricated ITO/Ni/n-GaN UV photodiodes result in improvement in the UV/visible rejection ratio, reduction in the leakage current and as well as the noise characteristic.

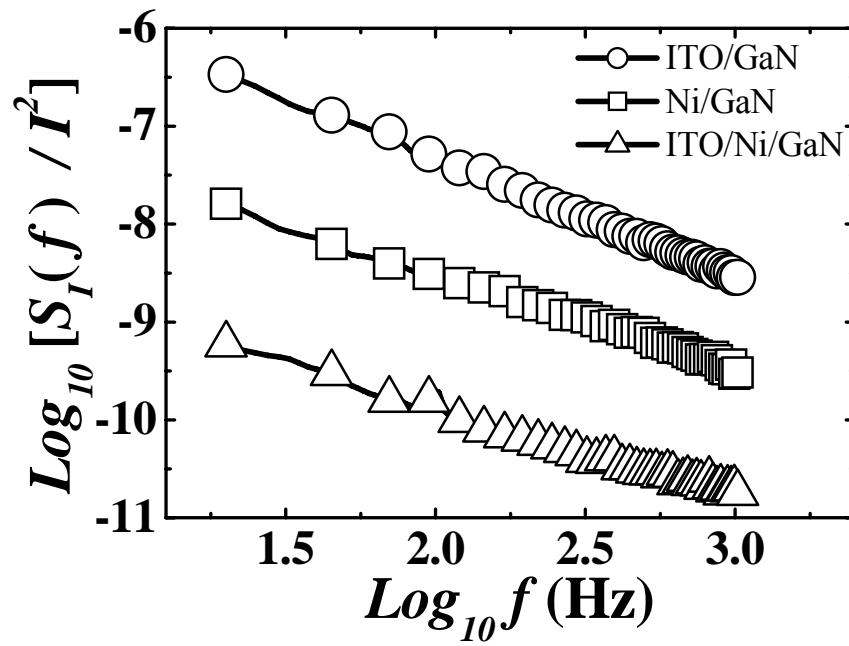


Figure 5.33: Normalized current noise spectrum  $S_I(f)/I^2$  for ITO/n-GaN, Ni/n-GaN and ITO/Ni/n-GaN Schottky photodiodes.

## **Chapter 6**

### **Conclusions and Suggestions for Future work**

Two types of visible-blind GaN-based Schottky contact photodiodes were fabricated on MBE-grown GaN layers in this study. The type I devices were fabricated on GaN films grown with the use of a novel double buffer layer system in which an intermediate-temperature GaN buffer layer (ITBL) is inserted in between the GaN epilayer and the conventional AlN buffer layer. Whereas in type II devices, the GaN layer was grown with a conventional AlN buffer layer only.

A high intensity ultraviolet light generated from a Xenon light source was used to illuminate the devices in order to study the radiation hardness of the detectors. It is found that the UV radiation hardness of the type I devices is much higher than the type II devices. Both electrical properties, including current-voltage, capacitance-voltage and low-frequency noise, and the optical characteristic, the spectral current responsivity, show that all the type II devices under test eventually exhibit catastrophic breakdowns upon exposure to the UV radiation. However, the type I device, in general, exhibit gradual and slow degradation and no devices broke down within the entire exposed

period studied. Experimental *I-V* and *C-V* data suggest that an alternative conduction path has been created prior to the breakdown. Furthermore, the substantial increase in the responsivity for wavelengths above 364 nm for the type II devices, after UV illumination, indicate either significant generation of traps or the activation of a metastable state within the bandgap, enabling electrons occupying these states to be excited by sub-bandgap photons. In addition, the increase in the low-frequency noise, which is caused by the trapping and detrapping of carriers by localized states, provides further evidence for the trap origin of the degradation. The experimental data clearly showed the significant role of crystalline defects in the breakdown of the devices and demonstrated the use of the double buffer layer structure in the improvement of the radiation hardness of the devices, which is showed to arise from the relaxation of the strain in the GaN layer.

The ITO/GaN Schottky detectors have also been explored, in which ITO replaced the highly absorptive and reflective semi-transparent metallic layer used in the conventional Schottky photodiodes structures. Systematic studies on the fabrication and characterization of ITO/n-GaN Schottky junction UV photodetectors were carried out. The effects of ITO deposition temperature and oxygen partial pressure were systematically studied to optimize the detectors' reponsivities. It was found that the reverse bias leakage current is strongly dependent on the ITO deposition conditions. The study shows that the relatively high leakage current and flicker noise of the device, compared to the Ni/n-GaN photodetectors, is due to the fact that ITOs were deposited at high temperature and in an oxidizing ambient. The formation of InGaN at the ITO/GaN

interface due to oxygen deficiency in the ITO, was found to be responsible for the high leakage of the detectors. In order to eliminate that effect, a unique device structure was investigated in which a thin Ni layer was deposited between the ITO and GaN film to passivate the GaN surface. The reduction in leakage currents and the low-frequency noise, showed that the thin Ni layer provides an effective passivation of the interfacial states. The results clearly show that the interface states at the Schottky junction play an important role on the device optoelectronic properties. The deposition of a thin Ni layer between the ITO and GaN is shown to provide an effective passivation of the interface states. Experimental results indicate that the using of such a unique device structure, enable significant improvement of the optoelectronic properties of the devices.

For further work, structural characterizations such as TEM analysis would be helpful. It could help to explain why the devices degraded under optical stress. However, care must be taken as the TEM only shows the detailed crystalline structure in a very small region and the material degradation may not occur evenly over the entire area of the device.

The accelerated optical stressing results obtained in this study clearly demonstrates the low frequency noise measurement can be use as a tool for industrial reliability assessment of photodetectors. It is shown that noise measurement is a fast, nondestructive and more sensitive characterization technique to evaluate the traps or defects densities generated in the devices subject to stress. Similar reliability studies, such as the voltage stressing technique used in MOSFET industry, may be applied. In the case of MOSFET, the time-to-failure measured at various voltages stressing

conditions are used to investigate the expected life times of the devices. One may apply the same approach using the high-intensity radiation stress and the noise measurement techniques as a characterization tool to study the life times of photodetectors. The high sensitivity of noise measurement helps substantially in reducing the stress time of the devices for the estimation of the time-to-failure. Further work and larger sampling size are required to correlate the time-to-failure of the devices to their noise level and form a more complete basis for commercial reliability assessment of optoelectronic devices.

Further work on the fundamental mechanisms of noise generation would be desirable and may contribute to the improvement of the photodetectors. Low temperature noise measurements will be helpful to determine noise mechanisms. Since the thermal activation model should give a more pronounced temperature dependence of noise power spectral density while the McWhorter model does not. Although previous work from our group had shown that the thermal activation model is the dominating process in other device structures, such as metal-semiconductor-metal (MSM) devices. It will be interesting to determine the dependency of the devices current noise spectral density and the device conductance. Because a quadratic relationship between the current noise power spectral density and conductance would indicate that noise originates from the barrier fluctuations induced by the capture and emission of charge carrier.

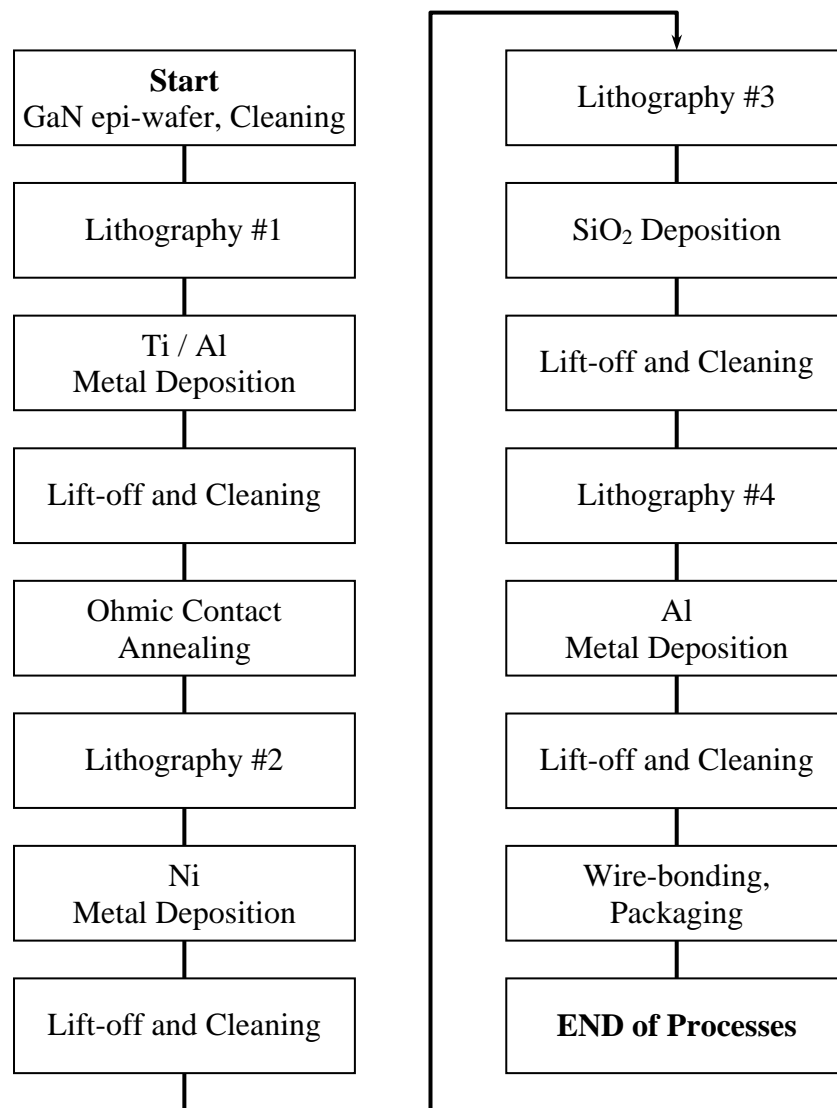
Further improvement on the ITO/Ni/GaN detector's performance can be obtained if the other parameters of the ITO are optimized. There are number of principal parameters, other than substrate temperature and oxygen partial pressure for the ITO deposition process, such as the grown rate, material composition and film thickness.

They play interdependent roles in the optimization of the film properties, as well as the device performance. It would require further work to arrive at optimal conditions for the fabrication of high performance ITO/GaN based UV detectors.

Finally, perhaps some novel device structures could be proposed to fabricate high performance UV photodetectors, one of which would be the development of a photodetector structure based on laser lift-off of GaN films. The removal of the sapphire substrate could further relax the lattice stress of the GaN layer and help in the reduction of the interfacial state at the Schottky contact. In addition, the integration of Si technologies with these photodetectors would be helpful for satisfying the demands of high-power and high-speed UV detection in the future.

## Appendix: Ni/GaN UV Detector Fabrication Processes

*Simplified Block Diagram of the Process Flow:*

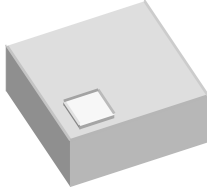
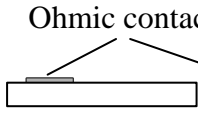
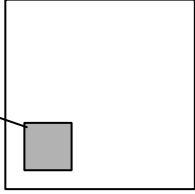
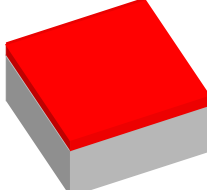
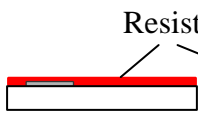
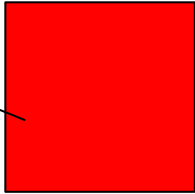
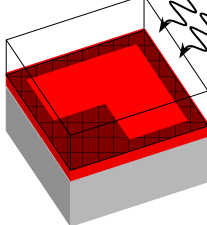
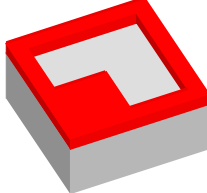
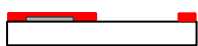
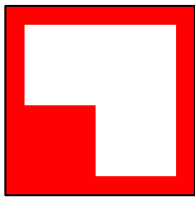
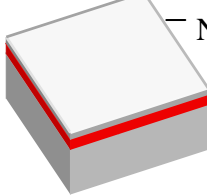
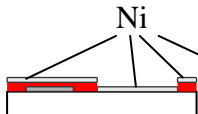
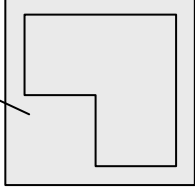
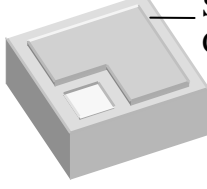
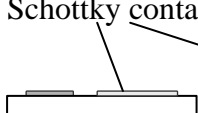
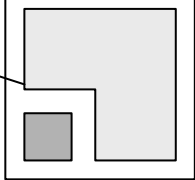


***Schematic of the Fabrication at Select Points in the Process Flow:***

Ohmic contact:

<u>Step</u>	<u>Process</u>	<u>Visualization</u>	<u>Cross-section</u>	<u>Top view</u>
(0)	Start with GaN epi-layer, cleaning			
(1)	Photoresist application			
(2)	Lithography #1		/	/
(3)	Resist Develop			
(4)	Metallization (e-beam Ti/Al)			
(5)	Lift-off, cleaning and annealing			

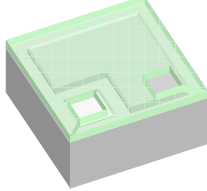
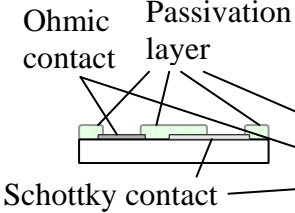
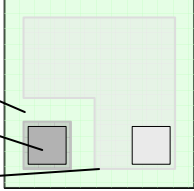
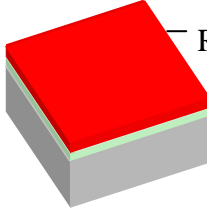
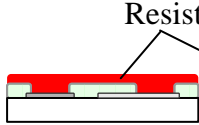
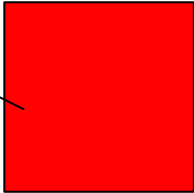
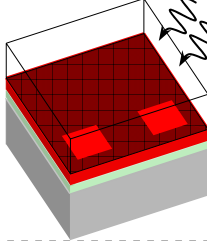
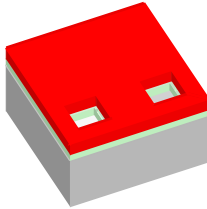
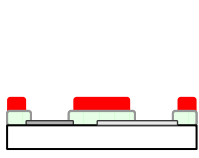
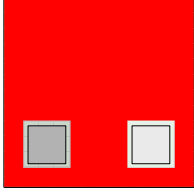
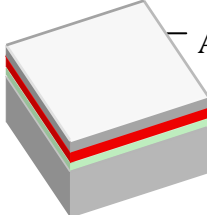
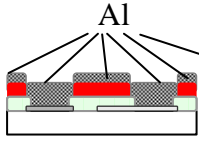
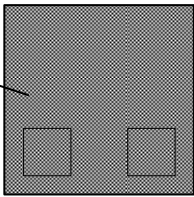
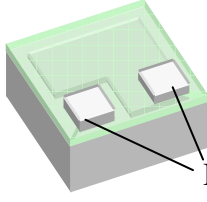
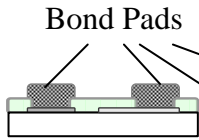
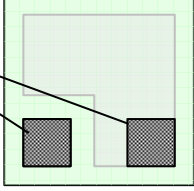
Schottky contact:

<u>Step</u>	<u>Process</u>	<u>Visualization</u>	<u>Cross-section</u>	<u>Top view</u>
(0)	After ohmic contact finish, cleaning			
(1)	Photoresist application			
(2)	Lithography #2		/	/
(3)	Resist Develop			
(4)	Metallization (e-beam Ni)			
(5)	Lift-off, cleaning			

Passivation:

Step	Process	Visualization	Cross-section	Top view
(0)	After Schottky contact finish, cleaning			
(1)	Photoresist application			
(2)	Lithography #3		/	/
(3)	Resist Develop			
(4)	Passivation (e-beam SiO <sub>2</sub> )			
(5)	Lift-off, cleaning			

Bond pad:

Step	Process	Visualization	Cross-section	Top view
(0)	After passivation, cleaning			
(1)	Photoresist application			
(2)	Lithography #4		/	/
(3)	Resist Develop			
(4)	Metallization (e-beam Al)			
(5)	Lift-off, cleaning			
<b>End of Processes</b>				

## References:

1. S. Nakamura, T. Mukai and M. Senoh, "Candela-class high-brightness InGaN/AlGaN double-heterostructure blue-light-emitting diodes", *Applied Physics Letters*, vol. 64, no. 13, pp. 1687 - 1689, 1994.
2. J. M. Van Hove, R. Hickman, J. J. Klaassen, P. P. Chow and P. P. Ruden, "Ultraviolet-sensitive, visible-blind GaN photodiodes fabricated by molecular beam epitaxy", *Applied Physics Letters*, vol. 70, no. 17, pp. 2282 - 2284, 1997.
3. J. C. Carrano, T. Li, D. L. Brown, P. A. Grudowski, C. J. Eiting, R. D. Dupuis and J. C. Campbell, "Very high-speed metal-semiconductor-metal ultraviolet photodetectors fabricated on GaN", *Applied Physics Letters*, vol. 73, no. 17, pp. 2405 - 2407, 1998.
4. D. Walker, E. Monroy, P. Kung, J. Wu, M. Hamilton, F. J. Sanchez, J. Diaz and M. Razeghi, "High-speed, low-noise metal-semiconductor-metal ultraviolet photodetectors based on GaN", *Applied Physics Letters*, vol. 74, no. 5, pp. 762 - 764, 1999.
5. T. D. Moustakas, E. Iliopoulos, A. V. Sampath, H. M. Ng, D. Doppalapudi, M. Misra, D. Korakakis and R. Singh, "Growth and device applications of III-nitrides by MBE", *Journal of Crystal Growth*, vol. 227-228, pp. 13 - 20, 2001.

6. S. E. Hooper, M. Kauer, V. Bousquet, K. Johnson, J. M. Barnes and J. Heffernan, "InGaN multiple quantum well laser diodes grown by molecular beam epitaxy", *Electronics Letters*, vol. 40, no. 1, pp. 33 - 34, 2004.
7. J. Heffernan, M. Kauer, S. E. Hooper, V. Bousquet and K. Johnson, "InGaN violet laser diodes grown by molecular beam epitaxy", *Physica Status Solidi A*, vol. 201, no. 12, pp. 2668 - 2671, 2004.
8. B. Gelmont, K. Kim and M. Shur, "Monte Carlo simulation of electron transport in gallium nitride", *Journal of Applied Physics*, vol. 74, pp. 1818 - 1821, 1993.
9. H. Morkoç, A. Di Carlo and R. Cingolani, "GaN-Based Modulation Doped FETs and UV Detectors", *Solid-State Electronics*, vol. 46, pp. 157 - 202, 2002.
10. M. Manfra, N. Weimann, Y. Baeyens, P. Roux and D. M. Tennant, "Unpassivated AlGaIn/GaN HEMTs with CW power density of 3.2 W/mm at 25 GHz grown by plasma-assisted MBE", *Electronics Letters*, vol. 39, no. 8, pp. 694 - 695, 2003.
11. R. S. Qhalid Fareed, X. Hu, A. Tarakji, J. Deng, R. Gaska, M. Shur and M. A. Khan, "High-power AlGaIn/InGaIn/AlGaIn/GaN recessed gate heterostructure field-effect transistors", *Applied Physics Letters*, vol. 86, no. 14, pp. 143512-1 - 143512-3, 2005.
12. S. N. Mohammad and H. Morkoç, "Progress and prospects of group-III nitride semiconductors", *Progress in Quantum Electronics*, vol. 20, no. 5-6, pp. 361 - 525, 1996.
13. H. Morkoç, "Nitride semiconductors and devices", Publisher: Springer Series in Materials Science, Springer, Berlin, 1999, p. 26.
14. S. C. Jain, M. Willander, J. Narayan and R. Van Overstraeten, "III-nitrides: Growth, characterization, and properties", *Journal of Applied Physics*, vol. 87, pp. 965 - 1006, 2000.

15. U. K. Mishra, Y. F. Wu, B. P. Keller, S. Keller and S. P. Denbaars, "GaN Microwave Electronics", IEEE Transactions on Microwave Theory and Techniques, vol. 46, no. 6, pp. 756 - 761, 1998.
16. J. C. Carrano, T. Li, P. A. Grudowski, R. D. Dupuis and J. C. Campbell, "Improved detection of the invisible", IEEE Circuits and Devices Magazine, vol. 15, no. 5, pp. 15 - 24, 1999.
17. E. Muñoz, E. Monroy, J. L. Pau, F. Calle, F. Omnès and P. Gibart, "III nitrides and UV detection", Journal of Physics: Condensed Matter, vol. 13, no. 32, pp. 7115 - 7137, 2001.
18. S. J. Pearton, B. S. Kang, S. Kim, F. Ren, B. P. Gila, C. R. Abernathy, J. Lin and S. N. G. Chu, "GaN-based diodes and transistors for chemical, gas, biological and pressure sensing", Journal of Physics: Condensed Matter, vol. 16, no. 29, pp. R961 - R994, 2004.
19. M. Misra, D. Korakakis, H. M. Ng and T. D. Moustakas, "Photoconductive detectors based on partially ordered  $\text{Al}_x\text{Ga}_{1-x}\text{N}$  alloys grown by molecular beam epitaxy", Applied Physics Letters, vol. 74, no. 15, pp. 2203 - 2205, 1999.
20. G. Parish, S. Keller, P. Kozodoy, J. P. Ibbetson, H. Marchand, P. T. Fini, S. B. Fleischer, S. P. DenBaars and U. K. Mishra, "High-performance (Al,Ga)N-based solar-blind ultraviolet p-i-n detectors on laterally epitaxially overgrown GaN", Applied Physics Letters, vol. 75, no. 2, pp. 247 - 249, 1999.
21. Y. K. Su, S. J. Chang, C. H. Chen, J. F. Chen, G. C. Chi, J. K. Sheu, W. C. Lai and J. M. Tsai, "GaN metal-semiconductor-metal ultraviolet sensors with various contact electrodes", IEEE Sensors Journal, vol. 2, no. 4, pp. 366 - 371, 2002.
22. B. M. Onat, M. Gökkavas, E. Özbay, E. P. Ata, E. Towe and M. S. Ünlü, "100-GHz resonant cavity enhanced Schottky photodiodes", IEEE Photonics Technology Letters, vol. 10, no. 5, pp. 707 - 709, 1998.

23. N. Biyikli, I. Kimukin, O. Aytur, M. Gokkavas, M. S. Unlu and E. Ozbay, "45GHz bandwidth-efficiency resonant cavity enhanced ITO-Schottky photodiodes", *IEEE Photonics Technology Letters*, vol. 13, no. 7, pp. 705 - 707, 2001.
24. N. Biyikli, T. Kartaloglu, O. Aytur, I. Kimukin and E. Ozbay, "High-performance solar-blind AlGaN Schottky photodiodes", *MRS Internet Journal of Nitride Semiconductor Research*, vol. 8, no. 2, 2003.
25. R. C. Powell, N. E. Lee, Y. W. Kim and J. E. Greene, "Heteroepitaxial wurtzite and zinc-blende structure GaN grown by reactive-ion molecular-beam epitaxy: Growth kinetics, microstructure, and properties", *Journal of Applied Physics*, vol. 73, pp. 189 - 204, 1993.
26. H. M. Ng, D. Doppalapudi and T. D. Moustakas, "The role of dislocation scattering in n-type GaN films", *Applied Physics Letters*, vol. 73, no. 6, pp. 821 - 823, 1998.
27. N. G. Weimann, L. F. Eastman, D. Doppalapudi, H. M. Ng and T. D. Moustakas, "Scattering of electrons at threading dislocations in GaN", *Journal of Applied Physics*, vol. 83, pp. 3656 - 3659, 1998.
28. K. Shiojima, T. Suemitsu and M. Ogura, "Correlation between current-voltage characteristics and dislocations for n-GaN Schottky contacts", *Applied Physics Letters*, vol. 78, no. 23, pp. 3636 - 3638, 2001.
29. D. S. Li, H. Chen, H. B. Yu, H. Q. Jia, Q. Huang and J. M. Zhou, "Dependence of leakage current on dislocations in GaN-based light-emitting diodes", *Journal of Applied Physics*, vol. 96, pp. 1111 - 1114, 2004.
30. W. K. Fong, C. F. Zhu, B. H. Leung and C. Surya, "Growth of high quality GaN thin films by MBE on intermediate-temperature buffer layers", *MRS Internet Journal of Nitride Semiconductor Research*, vol. 5, no. 12, 2000.

31. W. K. Fong, C. F. Zhu, B. H. Leung and C. Surya, "High-mobility GaN epilayer grown by rf plasma-assisted molecular beam epitaxy on intermediate-temperature GaN buffer layer", *Journal of Crystal Growth*, vol. 233, pp. 431 - 438, 2001.
32. C. F. Zhu, J. Q. Xie, W. K. Fong and C. Surya, "Influence of double buffer layers on properties of Ga-polarity GaN films grown by rf-plasma assisted molecular-beam epitaxy", *Materials Letters*, vol. 57, no. 16-17, pp. 2413 - 2416, 2003.
33. B. Gil, "Group III nitride semiconductor compounds: physics and applications", Publishers: Clarendon Press, Oxford, 1998, p. 1.
34. H. Morkoç, "Nitride semiconductors and devices", Publisher: Springer Series in Materials Science, Springer, Berlin, 1999, p. 39, 68.
35. H. Morkoç, "Nitride semiconductors and devices", Publisher: Springer Series in Materials Science, Springer, Berlin, 1999, p. 39.
36. J. Wu, W. Walukiewicz, K. M. Yu, J. W. Ager III, E. E. Haller, H. Lu and William J. Schaff, "Narrow bandgap group III-nitride alloys", *Physica Status Solidi B*, vol. 240, no. 2, pp. 412 - 416, 2003.
37. H. Morkoç, "Nitride semiconductors and devices", Publisher: Springer Series in Materials Science, Springer, Berlin, 1999, p. 68.
38. H. Morkoç, R. Cingolani and B. Gil, "Polarization effects in nitride semiconductor device structures and performance of modulation doped field effect transistors", *Solid-State Electronics*, vol. 43, pp. 1909 - 1927, 1999.
39. T. Suski, P. Perlin, H. Teisseyre, M. Leszczyński, I. Grzegory, J. Jun, M. Boćkowski, S. Porowski and T. D. Moustakas, "Mechanism of yellow luminescence in GaN", *Applied Physics Letters*, vol. 67, no. 15, pp. 2188 - 2190, 1995.
40. J. Neugebauer and C. G. Van de Walle, "Gallium vacancies and the yellow luminescence in GaN", *Applied Physics Letters*, vol. 69, no. 4, pp. 503 - 505, 1996.

41. S. Yoshida, "Photoluminescence measurement of InGaN and GaN grown by a gas-source molecular-beam epitaxy method", *Journal of Applied Physics*, vol. 81, pp. 7966 - 7969, 1997.
42. A. Y. Polyakov, N. B. Smirnov, A. S. Usikov, A. V. Govorkov and B. V. Pushniy, "Studies of the origin of the yellow luminescence band, the nature of nonradiative recombination and the origin of persistent photoconductivity in n-GaN films", *Solid-State Electronics*, vol. 42, pp. 1959 - 1967, 1998.
43. S. Yoshida, S. Misawa and S. Gonda, "Improvements on the electrical and luminescent properties of reactive molecular beam epitaxially grown GaN films by using AlN-coated sapphire substrates", *Applied Physics Letters*, vol. 42, no. 5, pp. 427 - 429, 1983.
44. S. Nakamura, "GaN growth using GaN buffer layer", *Japanese Journal of Applied Physics*, vol. 30, no. 10A, pp. L1705 - 1707, 1991.
45. M. A. Herman and H. Sitter, "Molecular beam epitaxy: fundamentals and current status", Publisher: Springer, New York, 2nd Revision, 1996.
46. A. Y. Polyakov, N. B. Smirnov, A. V. Govorkov, M. G. Mil'vidskii, S. J. Pearton, A. S. Usikov, N. M. Shmidt, A. V. Osinsky, W. V. Lundin, E. E. Zavarin, "Deep levels studies of AlGaIn/GaN superlattices", *Solid-State Electronics*, vol. 47, pp. 593 - 762, 2003.
47. J. Heffernan, M. Kauer, K. Johnson, C. Zellweger, S. E. Hooper and V. Bousquet, "InGaIn multiple quantum well lasers grown by MBE", *Physica Status Solidi A*, vol. 202, no. 5, pp. 868 - 874, 2005.
48. D. Sugihara, A. Kikuchi, K. Kusakabe, S. Nakamura, Y. Toyoura, T. Yamada and K. Kishino, "2.6  $\mu\text{m}/\text{h}$  high-speed growth of GaN by rf-molecular beam epitaxy and improvement of crystal quality by migration enhanced epitaxy", *Physica Status Solidi A*, vol. 176, no. 1, pp. 323 - 328, 1999.

49. D. Sugihara, A. Kikuchi, K. Kusakabe, S. Nakamura, Y. Toyoura, T. Yamada and K. Kishino, "High-quality GaN on AlN multiple intermediate layer with migration enhanced epitaxy by rf-molecular beam epitaxy", *Japanese Journal of Applied Physics, Part 2 (Letters)*, vol. 39, no. 3A/B, pp. L197 - 199, 2000.
50. A. Kikuchi, T. Yamada, S. Nakamura, K. Kusakabe, D. Sugihara and K. Kishino, "Improvement of crystal quality of rf-plasma-assisted molecular beam epitaxy grown Ga-polarity GaN by high-temperature grown AlN multiple intermediate layers", *Japanese Journal of Applied Physics, Part 2 (Letters)*, vol. 39, no. 4B, pp. L330 - 333, 2000.
51. W. K. Fong, B. H. Leung and C. Surya, "In: Advances in condensed matter and materials research, Volume 5, Editor: Francois Gerard", Publisher: Nova Science Publishers Inc., Huntington, New York, pp. 1 - 40, 2004.
52. M. E. Lin, Z. Ma, F. Y. Huang, Z. F. Fan, L. H. Allen and H. Morkoç, "Low resistance ohmic contacts on wide band-gap GaN", *Applied Physics Letters*, vol. 64, no. 8, pp. 1003 - 1005, 1994.
53. A. C. Schmitz, A. T. Ping, M. Asif Khan, Q. Chen, J. W. Yang and I. Adesida, "Schottky barrier properties of various metals on n-type GaN", *Semiconductor Science and Technology*, vol. 11, no. 10, pp. 1464 - 1467, 1996.
54. W. Lei, M. I. Nathan, T. H. Lim, M. A. Khan and Q. Chen, "High barrier height GaN Schottky diodes: Pt/GaN and Pd/GaN", *Applied Physics Letters*, vol. 68, no. 9, pp. 1267 - 1269, 1996.
55. B. P. Luther, S. E. Mohny, T. N. Jackson, M. A. Khan, Q. Chen and J. W. Yang, "Investigation of the mechanism for ohmic contact formation in Al and Ti/Al contacts to n-type GaN", *Applied Physics Letters*, vol. 70, no. 1, pp. 57 - 59, 1997.
56. Y. Kribes, I. Harrison, B. Tuck, T. S. Cheng and C. T. Foxon, "Investigation of Au Schottky contacts on GaN grown by molecular beam epitaxy", *Semiconductor Science and Technology*, vol. 12, no. 7, pp. 913 - 916, 1997.

57. F. Braun, Poggendorffs Annalen, vol. 153, pp. 556, 1874.
58. W. Schottky, "Halbleitertheorie der Sperrschicht", Naturwissenschaften, vol. 26, no. 52, pp. 843, 1938.
59. N. F. Mott, Proceedings of the Cambridge Philosophical Society, vol. 34, pp. 568, 1938.
60. E. H. Rhoderick and R. H. Williams, "Metal-semiconductor contacts", Publisher: Clarendon Press, Oxford, 2nd Edition, 1988.
61. H. Morkoç, "Nitride semiconductors and devices", Springer Series in Materials Science, Springer, Berlin, 1999, p. 191.
62. L. S. Yu and E. T. Yu, "In: III-V nitride semiconductors: applications and devices, Editors: E. T. Yu and M. O. Manasreh", Publisher: Taylor & Francis, New York, 2003, p. 81.
63. D. Donoval, M. Barus and M. Zdimal, "Analysis of I-V measurements on PtSi-Si Schottky structures in a wide temperature range", Solid-State Electronics, vol. 34, pp. 1365 - 1373, 1991.
64. S. N. Mohammad, "Contact mechanisms and design principles for Schottky contacts to group-III nitrides", Journal of Applied Physics, vol. 97, pp. 63703-1 - 19, 2005.
65. F. A. Padovani and R. Stratton, "Field and thermionic-field emission in Schottky barriers", Solid-State Electronics, vol. 9, pp. 695 - 707, 1966.
66. J. Singh, "Semiconductor optoelectronics: physics and technology", Publisher: McGraw-Hill, New York, 1995, p. 336.
67. J. M. Senior, "Optical fiber communications: principles and practice", Publisher: Prentice Hall Inc., New Jersey, USA, 2nd Edition, 1992, p. 419.

68. D. H. Lee, S. S. Li and N. G. Paulter, "A low dark current, high-speed GaAs/Al<sub>0.3</sub>Ga<sub>0.7</sub>As heterostructure Schottky barrier photodiode", *IEEE Journal of Quantum Electronics*, vol. 25, no. 5, pp. 858 - 861, 1989.
69. J. Kuhl, M. Klingenstein, J. Rosenzweig, C. Moglestue and A. Axmann, "Picosecond electron and hole transport in metal-semiconductor-metal photodetectors", *Semiconductor Science and Technology*, vol. 7, no. 3B, pp. B157 - 159, 1992.
70. T. Mori, T. Kozawa, T. Ohwaki, Y. Taga, S. Nagai, S. Yamasaki, S. Asami, N. Shibata and M. Koike, "Schottky barriers and contact resistances on p-type GaN", *Applied Physics Letters*, vol. 69, no. 23, pp. 3537 - 3539, 1996.
71. H. M. Ng, D. Doppalapudi, D. Korakakis, R. Singh and T. D. Moustakas, "MBE growth and doping of III-V nitrides", *Journal of Crystal Growth*, vol. 189-190, pp. 349 - 353, 1998.
72. J. K. Sheu, Y. K. Su, G. C. Chi, P. L. Koh, M. J. Jou, C. M. Chang, C. C. Liu and W. C. Hung, "High-transparency Ni/Au ohmic contact to p-type GaN", *Applied Physics Letters*, vol. 74, no. 16, pp. 2340 - 2342, 1999.
73. A. Bhattacharyya, W. Li, J. Cabalu, T. D. Moustakas, David J. Smith and R. L. Hervig, "Efficient p-type doping of GaN films by plasma-assisted molecular beam epitaxy", *Applied Physics Letters*, vol. 85, no. 21, pp. 4956 - 4958, 2004.
74. M. W. Cole and P. C. Joshi, "In: III-V nitride semiconductors : applications and devices, Editors: E. T. Yu and M. O. Manasreh", Publisher: Taylor & Francis, New York , 2003, p. 31.
75. J. C. Carrano, T. Li, P. A. Grudowski, C. J. Eiting, D. Lambert, J. D. Schaub, R. D. Dupuis and J. C. Campbell, "Low dark current pin ultraviolet photodetectors fabricated on GaN grown by metal organic chemical vapour deposition", *Electronics Letters*, vol. 34, no. 7, pp. 692 - 694, 1998.

76. A. Osinsky, S. Gangopadhyay, B. W. Lim, M. Z. Anwar, M. A. Khan, D. V. Kuksenkov and H. Temkin, "Schottky barrier photodetectors based on AlGaN", *Applied Physics Letters*, vol. 72, no. 6, pp. 742 - 744, 1998.
77. C. Y. Chang and S. M. Sze, "VLSI Technology", Publisher: McGraw-Hill, New York, 2nd edition, 1988, p. 329.
78. B. J. Pong, C. J. Pan, Y. C. Teng, G. C. Chi, W. H. Li, K. C. Lee and C. H. Lee, "Structural defects and microstrain in GaN induced by Mg ion implantation", *Applied Physics Letters*, vol. 83, no. 11, pp. 5992 - 5996, 1998.
79. W. K. Fong, "Growth of high quality gallium nitride thin films by rf-plasma assisted molecular beam epitaxy", Ph.D. thesis in The Hong Kong Polytechnic University, 2001.
80. W. K. Fong, B. H. Leung, J. Q. Xie and C. Surya, "Study of low-frequency excess noise transport in Ga-face and N-face GaN thin films grown on intermediate-temperature buffer layer by RF-MBE", *Physica Status Solidi A*, vol. 192, no. 2, pp. 466 - 471, 2002.
81. W. K. Fong, S. W. Ng, B. H. Leung and C. Surya, "Characterization of low-frequency noise in molecular beam epitaxy-grown GaN epilayers deposited on double buffer layers", *Journal of Applied Physics*, vol. 94, pp. 387 - 391, 2003.
82. M. Leszczyński, T. Suski, H. Teisseyre, P. Perlin, I. Grzegory, J. Jun, S. Porowski and T. D. Moustakas, "Thermal expansion of gallium nitride", *Journal of Applied Physics*, vol. 76, pp. 4909 - 4911, 1994.
83. W. Shan, R. J. Hauenstein, A. J. Fischer, J. J. Song, W. G. Perry, M. D. Bremser, R. F. Davis and B. Goldenberg, "Strain effects on excitonic transitions in GaN: Deformation potentials", *Physical Review B (Condensed Matter)*, vol. 54, no. 19, pp. 13460 - 13463, 1996.
84. M. Schroeder and D. E. Wolf, "Diffusion on strained surfaces", *Surface Science*, vol. 375, no. 1, pp. 129 - 140, 1997.

85. N. V. Edwards, M. D. Bremser, A. D. Batchelor, I. A. Buyanova, L. D. Madsen, S. D. Yoo, T. Wethkamp, K. Wilmers, C. Cobet, N. Esser, R. F. Davis, D. E. Aspnes and B. Monemar, "Optical characterization of wide bandgap semiconductors", *Thin Solid Films*, vol. 364, pp. 98 - 106, 2000.
86. E. H. Rhoderick and R. H. Williams, "Metal-semiconductor contacts", Publisher: Clarendon Press, Oxford, 2nd Edition, 1988, p. 99, 107.
87. Thorsten U. Kampen and Winfried Monch, "Barrier heights of GaN Schottky contacts", *Applied Surface Science*, vol. 117/118, pp. 388 - 393, 1997.
88. X. A. Cao, S. J. Pearton, G. Dang, A. P. Zhang, F. Ren and J. M. Van Hove, "Effects of interfacial oxides on Schottky barrier contacts to n- and p-type GaN", *Applied Physics Letters*, vol. 75, no. 26, pp. 4130 - 4132, 1999.
89. T. Sawada, Y. Ito, K. Imai, K. Suzuki, H. Tomozawa and S. Sakai, "Electrical properties of metal/GaN and SiO<sub>2</sub>/GaN interfaces and effects of thermal annealing", *Applied Surface Science*, vol. 159-160, pp. 449 - 455, 2000.
90. K. M. Tracy, P. J. Hartlieb, S. Einfeldt, R. F. Davis, E. H. Hurt and R. J. Nemanich, "Electrical and chemical characterization of the Schottky barrier formed between clean n-GaN(0001) surfaces and Pt, Au, and Ag", *Journal of Applied Physics*, vol. 94, pp. 3939 - 3948, 2003.
91. T. Sawada, N. Kimura, K. Imai, K. Suzuki and K. Tanahashi, "Interpretation of current transport properties at Ni/n-GaN Schottky interfaces", *Journal of Vacuum Science & Technology B*, vol. B22, no. 4, pp. 2051 - 2058, 2004.
92. A. M. Goodman, "Metal-semiconductors barrier height measurement by the differential capacitance method - one carrier system", *Journal of Applied Physics*, vol. 34, pp. 329 - 338, 1963.
93. G. Hu, J. Shi, Y. Shi, X. Yang and J. Li, "An improved method and experimental results of noise used as reliability estimation for semiconductor lasers", *Optics and Laser Technology*, vol. 35, pp. 481 - 483, 2003.

94. L. K. J. Vandamme, "Noise as a diagnostic tool for quality and reliability of electronic devices", IEEE Transactions on Electron Devices, vol. 41, no. 11, pp. 2176 - 2187, 1994.
95. A. D. van Rheenen, G. Bosman and C. M. Van Vliet, "Decomposition of generation-recombination noise spectra in separate Lorentzians", Solid-State Electronics, vol. 28, pp. 457 - 463, 1985.
96. G. Bosman and R. J. J. Zijlstra, "Generation-recombination noise in p-type silicon", Solid-State Electronics, vol. 25, pp. 273 - 280, 1982.
97. A. D. van Rheenan, G. Bosman and R. J. J. Zijlstra, "Low frequency noise measurements as a tool to analyze deep-level impurities in semiconductor devices", Solid-State Electronics, vol. 30, pp. 259 - 265, 1987.
98. F. Hofman, R. J. J. Zijlstra and J. C. M. Henning, "Current noise in n-type  $\text{Al}_x\text{Ga}_{1-x}\text{As}$ ", Solid-State Electronics, vol. 31, pp. 279 - 282, 1988.
99. F. Hofman, R. J. J. Zijlstra and J. M. Bettencourt de Freitas, "Voltage noise in an  $\text{Al}_x\text{Ga}_{1-x}\text{As}$  heterostructure", Journal of Applied Physics, vol. 67, pp. 2482 - 2487, 1990.
100. F. N. Hooge and A. M. F. Hoppenbrouwers, " $1/f$  noise in continuous thin gold films", Physica, vol. 45, no. 3, pp. 386 - 392, 1969.
101. F. N. Hooge, " $1/f$  noise", Physica B, vol. 83, no. 1, pp. 14 - 23, 1976.
102. C. M. Van Vliet, "A survey of results and future prospects on quantum  $1/f$  noise and  $1/f$  noise in general", Solid-State Electron, vol. 34, pp. 1 - 21, 1991.
103. P. H. Handel, "In: Noise in Physical Systems and  $1/f$  Noise. Proceedings of the 8th International Conference on Noise in Physical Systems and the 4th International Conference on  $1/f$  Noise", editors: M. Savelli, G. Lecoy and J. P. Nougier, Montpellier, 1983, p. 97.

104. C. Surya and T. Y. Hsiang, "Theory and experiment on the  $1/f$  noise in p-channel MOSFET at low drain bias", *Physical Review B*, vol. 33, no. 7, pp. 4898 - 4905, 1986.
105. C. Surya and T. Y. Hsiang, "Surface mobility fluctuations in MOSFETs", *Physical Review B*, vol. 35, no. 12, pp. 6343 - 6347, 1987.
106. C. Surya and T. Y. Hsiang, "A thermal activation model for  $1/f$  noise in Si-MOSFETs", *Solid-State Electronics*, vol. 31, pp. 959 - 964, 1988.
107. M. M. Surdin, *Journal de Physique et le Radium*, vol. 10, p.188, 1939.
108. A. L. McWhorter, Ph.D. thesis in semiconductor surface physics, editor: R. H. Kinston, University of Pennsylvania Press, Philadelphia, 1956.
109. A. Van der Ziel, "Noise in solid-state devices and lasers", *Proceedings of the IEEE*, vol. 58, no. 8, pp. 1178 - 1206, 1970.
110. P. Dutta, P. Dimon and P. M. Horn, "Energy scales for noise processes in metals", *Physical Review Letters*, vol. 43, no. 9, pp. 646 - 649, 1979.
111. P. Dutta and P. M. Horn, "Low-frequency fluctuations in solids:  $1/f$  noise", *Reviews of Modern Physics*, vol. 53, no. 3, pp. 497 - 516, 1981.
112. J. Singh, "Semiconductor optoelectronics: physics and technology", Publisher: McGraw-Hill, New York, 1995, p. 342.
113. International Commission on Illumination, "CIE 85-1989. Solar spectral irradiance", 1989.
114. G. A. Umana-Membreno, J. M. Dell, G. Parish, B. D. Nener, L. Faraone and U. K. Mishra, " $^{60}\text{Co}$  Gamma Irradiation Effects on n-GaN Schottky Diodes", *IEEE Transactions on Electron Devices*, vol. 50, no. 12, pp. 2326 - 2334, 2003.

115. T. Makimoto, M. Kashiwa, T. Kido, N. Matsumoto, K. Kumakura and N. Kobayashi, "Schottky barrier heights of Au, Pd and Ni on n-GaN evaluated using mesa-structure diodes", *Physica Status Solidi C*, vol. 0, no. 7, pp. 2393 - 2395, 2003.
116. P. Jayavel, M. Udhayasankar, J. Kumar, K. Asokan and D. Kanjilal, "Electrical characterisation of high energy  $^{12}\text{C}$  irradiated Au/n-GaAs Schottky Barrier Diodes", *Nuclear Instruments and Methods in Physics Research B*, vol. 156, pp. 110 - 115, 1999.
117. B. H. Leung, W. K. Fong, C. F. Zhu and C. Surya, "Study of low-frequency excess noise in gallium nitride thin films deposited by rf-MBE on intermediate-temperature buffer layers", *IEEE Transactions on Electron Devices*, vol. 48, no. 10, pp. 2400 - 2404, 2001.
118. B. H. Leung, N. H. Chan, W. K. Fong, C. F. Zhu, S. W. Ng, H. F. Lui, K. Y. Tong, C. Surya, L. W. Lu and W. K. Ge, "Characterization of deep levels in Pt-GaN Schottky diodes deposited on intermediate-temperature buffer layers", *IEEE Transactions on Electron Devices*, vol. 49, no. 2, pp. 314 - 318, 2002.
119. V. V. Emtsev, V. Yu. Davydov, I. N. Goncharuk, E. V. Kalinina, V. V. Kozlovskii, D. S. Poloskin, A. V. Sakharov, N. M. Shmidt, A. N. Smirnov and A. S. Usikov, "Impact of radiation-induced defects on the yellow luminescence band in MOCVD GaN", *Materials Science Forum*, vol. 258-263, pp. 1143 - 1148, 1997.
120. C. G. Granqvist and A. Hultåker, "Transparent and conducting ITO films: new developments and applications", *Thin Solid Films*, vol. 411, pp. 1 - 5, 2002.
121. K. L. Chopar, S. Major and D. K. Pandya, "Transparent conductors - a status review", *Thin Solid Films*, vol. 102, pp. 1 - 46, 1983.
122. F. P. Fehlner, "Thin films on glass for liquid crystal displays", *Journal of Non-Crystalline Solids*, vol. 218, pp. 360 - 367, 1997.

123. C. Y. Kwong, A. B. Djurišić, P. C. Chui, L. S. M. Lam and w. K. Chan, "Improvement of the efficiency of phthalocyanine organic Schottky solar cells with ITO electrode treatment", *Applied Physics A: Materials Science & Processing*, vol. 77, no. 3-4, pp. 555 - 560, 2003.
124. N. Biyikli, I. Kimukin, B. Butun, O. Aytur and E. Ozbay, "ITO-Schottky photodiodes for high-performance detection in the UV-IR spectrum", *IEEE Journal of Selected Topics in Quantum Electronics*, vol. 10, no. 4, pp. 759 - 765, 2004.
125. H. Wrzesińska, L. Ilka, D. Wawer, K. Hejduk, A. Kudła, M. Bugajski and E. Łusakowska, "Investigation of Indium Tin Oxide (ITO) films for the VCSEL laser with dielectric Bragg reflectors", *Physica Status Solidi C*, vol. 1, no. 2, pp. 396 - 400, 2004.
126. C. H. Chen, S. J. Chang, Y. K. Su, G. C. Chi, J. Y. Chi, C. A. Chang, J. K. Sheu and J. F. Chen, "GaN metal-semiconductor-metal ultraviolet photodetectors with transparent indium-tin-oxide Schottky contacts", *IEEE Photonics Technology Letters*, vol. 13, no. 8, pp. 848 - 850, 2001.
127. Y. K. Su, F. S. Juang and M. H. Chen, "GaN metal-semiconductor-metal visible-blind photodetectors with transparent indium-tin-oxide contact electrodes", *Japanese Journal of Applied Physics*, vol. 42, no. 4B, pp. 2257 - 2259, 2003.
128. J. K. Sheu, Y. K. Su, G. C. Chi, M. J. Jou and C. M. Chang, "Effects of thermal annealing on the indium tin oxide Schottky contacts of n-GaN", *Applied Physics Letters*, vol. 72, no. 25, pp. 3317 - 3319, 1998.
129. N. Biyikli, T. Kartaloglu, O. Aytur, I. Kimukin and E. Ozbay, "High-speed visible-blind GaN-based indium-tin-oxide Schottky photodiodes", *Applied Physics Letters*, vol. 79, no. 17, pp. 2838 - 2840, 2001.
130. Y. Z. Chiou and J. J. Tang, "GaN photodetectors with transparent Indium Tin Oxide Electrodes", *Japanese Journal of Applied Physics*, vol. 43, no. 7A, pp. 4146 - 4149, 2004.

131. P. Nath and R. F. Bunshah, "Preparation of  $\text{In}_2\text{O}_3$  and tin-doped  $\text{In}_2\text{O}_3$  films by a novel activated reactive evaporation technique", *Thin Solid Films*, vol. 69, pp. 63 - 68, 1980.
132. O. N. Mryasov and A. J. Freeman, "Electronic band structure of indium tin oxide and criteria for transparent conducting behavior", *Physical Review B*, vol. 64, pp. 233111-1 - 3, 2001.
133. J. C. C. Fan and J. B. Goodenough, "X-Ray photoemission spectroscopy studies of Sn-doped indium oxide films", *Journal of Applied Physics*, vol. 48, pp. 3524 - 3531, 1977.
134. N. Balasubramanian and A. Subrahmanyam, "Electrical and optical properties of reactively evaporated indium tin oxide (ITO) films - Dependence on substrate temperature and tin concentration", *Journal of Physics D: Applied Physics*, vol. 22, no. 1, pp. 206 - 209, 1989.
135. I. Hamberg, C. G. Granqvist, K. F. Berggren, B. E. Sernelius and L. Engström, "Band-gap widening in heavily Sn-doped  $\text{In}_2\text{O}_3$ ", *Physical Review B*, vol. 30, pp. 3240 - 3249, 1984.
136. L. Gupta, A. Mansingh and P. K. Srivastava, "Band gap narrowing and the band structure of tin-doped indium oxide films", *Thin Solid Films*, vol. 176, pp. 33 - 34, 1989.
137. H. Odaka, Y. Shigesato, T. Murakami and S. Iwata, "Electronic structure analyses of Sn-doped  $\text{In}_2\text{O}_3$ ", *Japanese Journal of Applied Physics, Part 1*, vol. 40, no. 5A, pp. 3231 - 3235, 2001.
138. H. Kobayashi, T. Ishida, K. Nakamura, Y. Nakato and H. Tsubomura, "Properties of indium tin oxide films prepared by the electron beam evaporation method in relation to characteristics of indium tin oxide/silicon oxide/silicon junction solar cells", *Journal of Applied Physics*, vol. 72, pp. 5288 - 5293, 1992.

139. T. Ishida, H. Kobayashi and Y. Nakato, "Structures and properties of electron-beam-evaporated indium tin oxide films as studied by x-ray photoelectron spectroscopy and work-function measurements", *Journal of Applied Physics*, vol. 73, pp. 4344 - 4350, 1993.
140. P. Thilakan and J. Kumar, "Studies on the preferred orientation changes and its influenced properties on ITO thin films", *Vacuum*, vol. 48, no. 5, pp. 463 - 466, 1997.
141. A. Salehi, "The effects of deposition rate and substrate temperature of ITO thin films on electrical and optical properties", *Thin Solid Films*, vol. 324, pp. 214 - 218, 1998.
142. H. J. Kim, J. W. Bae, J. S. Kim, K. S. Kim, Y. C. Jang, G. Y. Yeom and N. E. Lee, "Electrical, optical, and structural characteristics of ITO thin films by krypton and oxygen dual ion-beam assisted evaporation at room temperature", *Thin Solid Films*, vol. 377-378, pp. 115 - 121, 2000.
143. K. H. Shim, M. C. Paek, B. T. Lee, C. Kim and J. Y. Kang, "Preferential regrowth of indium-tin oxide (ITO) films deposited on GaN(0001) by rf-magnetron sputter", *Applied Physics A*, vol. 72, pp. 471 - 474, 2001.
144. D. Yu, W. Yu, D. Wang and Y. Qian, "Structural, optical, and electrical properties of indium tin oxide films with corundum structure fabricated by a sol-gel route based on solvothermal reactions", *Thin Solid Films*, vol. 419, pp. 166 - 172, 2002.
145. C. Nunes de Carvalho, G. Lavaredaa, E. Fortunatoa and A. Amaral, "Properties of ITO films deposited by r.f.-PERTE on unheated polymer substrates - dependence on oxygen partial pressure", *Thin Solid Films*, vol. 427, pp. 215 - 218, 2003.
146. F. D. Auret, S. A. Goodman, F. K. Koschnick, J. M. Spaeth, B. Beaumont and P. Gibart, "Sputter deposition-induced electron traps in epitaxially grown n-GaN", *Applied Physics Letters*, vol. 74, no. 15, pp. 2173 - 2175, 1999.

147. Y. Z. Chiou, Y. K. Su, S. J. Chang, J. F. Chen, C. S. Chang, S. H. Liu, Y. C. Lin and C. H. Chen, "Transparent TiN electrodes in GaN metal-semiconductor-metal ultraviolet photodetectors", Japanese Journal of Applied Physics, vol. 41, no. 6A, pp. 3643 - 3645, 2002.